Surface Wave Propagation in 3-D Anelastic Media

Youyi Ruan

Dissertation submitted to the Faculty of the

Virginia Polytechnic Institute and State University

in partial fulfillment of the requirements for the degree of

Doctor of Philosophy

in

Geosciences

Ying Zhou, Chair

John A. Hole

Scott D. King

Chester J. Weiss

August 28, 2012

Blacksburg, Virginia

Keywords: Surface waves, Seismic attenuation, Anelasticity, Wave scattering and diffraction.

Surface Wave Propagation in 3-D Anelastic Media

Youyi Ruan

(ABSTRACT)

Lateral perturbations in anelasticity (Q) and wave speed together provide important constraints on thermal and chemical structures in the mantle. In present-day tomography studies of global wave speed and anelasticity, the significance of 3-D wave speed and 3-D Q structures on surface wave travel times and amplitudes has not been well understood. In this dissertation, the effects of lateral perturbations in anelasticity (Q) and wave speed on surface wave observables are quantified based upon wave propagation simulations in 3-D earth models using a Spectral Element Method.

Comparison between phase delays caused by 3-D wave speed structures and those caused by 3-D Q variations show that anelastic dispersion due to lateral perturbation in Q is important in long-period surface wave and can account for 15-20$\%$ observed phase delays. For amplitude perturbations, elastic focusing/defocusing effects associated with 3-D wave speed structures are dominant while energy dissipation is important in short-period ($\sim$ 50 s) surface waves but decreases quickly with increasing wave period. Anelastic focusing/defocusing associated with 3-D anelastic dispersion becomes more important than wave attenuation in longer period surface waves.

In tomography studies, ray theory breaks down and finite frequency effects become important when the length scale of heterogenities are smaller than seismic wavelength. Finite frequency effects in 3-D earth models are investigated by comparing theoretical predictions of travel times and amplitudes with "ground truth" measurements made on synthetic seismograms generated in SEM simulations. The comparisons show that finite frequency effects are stronger in amplitudes than in phases, especially at long periods.

Acknowledgments

It has been an enjoyable and rewarding experience to study at Virginia Tech. I feel myself lucky to join Geophysics group in 2007, and I am grateful to many professors and fellow students in this group for their kind help. Among them, I feel indebted to Prof. Ying Zhou, who is a great advisor guiding me to theoretical and computational seismology and inspiring me to explore anelasticity of Earth interior. She encouraged me to pursue my research interests and always gave me patient guidance when I have difficulties. She is also a considerate friend and has been a tremendous help to me and my family in so many ways.

I am grateful to my committee members, Prof. Scott D. King, Prof. John A. Hole, and Prof. Chester J. Weiss. Prof. King has been a great help on Geodynamics, and it is definitely necessary to take his Geodynamics class twice. He is knowledgable and humor, discussions with him during group meetings is always beneficial and joyful. Prof. Hole also has been a constant source of help; he has provided constructive suggestions to my research and helped me networking at conferences for my career future. I would like to thank Prof. Weiss for his feedbacks and contributes regarding my research. My gratitude also extend to other Geosciences faculty members, especially Prof. Arthur Snoke, Prof. Bob Lowell, Prof. Ross Angel and Prof. Martin Chapman, for their informative graduate courses and valuable discussions which I found useful in my research.

My special thanks to Changyeol Lee and Kui Liu for their friendship over the years. My fel-

low students, Ellen Gilliland, Pavithra Sekhar, Kate Craft, Sharmin Shamsalsadati, Eric Kazlaukas, Samuel Fortson, Karina Cheung, Oluyinka Oyewumi, Tannistha Maiti, Aida Farough, Shreya Singh, and Cable Warren, are always fun to talk with. I would like to thank Bin shen, Juan Liu and Guo zheying for their kind host and thoughtful help when I first arrived in Blacksburg, and year-long free rides. I will miss the good time with my chinese friends, Di Wang, Liang Han (panda), Kai Wang, and Meijing Zhang, for dinning around.

I wish to thank administrative staff, Connie Lowe, Ellen Mathena, Mary McMurray, and Linda Bland for their kind assistance, and Richard Godbee and Mark Lemon for their technical support in the past five years.

I would like to thank my parents and my brother for their continuous support, and my parents-in-law for taking care of my daughter Arwen. At last, I have to express my deepest thanks to my wife, Wei Sun, who has been a great support of my PhD studies with her love and care.

Contents

List of Figures

List of Tables

Chapter 1

Introduction

1.1 Anelasticity of the Earth

It's well known that earth materials are not purely elastic, when an earthquake occurs, seismic waves propagating in the earth's mantle will quickly attenuate due to the internal friction of the earth. Energy dissipation of seismic waves is often measured by the quality factor Q. The inverse of Q is defined as

$$Q^{-1} = \frac{\Delta E}{2\pi E}, \tag{1.1}$$

where ΔE is the energy loss per unit cycle and E is the total strain energy stored in unit volume associated with seismic waves. In addition to amplitude attenuation, anelasticity also causes velocity dispersion of seismic waves — the speed of seismic wave depends on the frequency of the wave.

Modern measurements of anelasticity using seismological observations date back to 1950s. The early efforts were primarily based upon amplitude measurements of earth's free oscillations (e.g., Anderson & Archambeau, 1964; Deschamps, 1977; Anderson & Hart, 1978; Sailor & Dziewonski, 1978) and attenuation of long-period surface wave amplitudes (e.g., Sato, 1958; Canas & Mitchell,

1978, 1981; Dziewonski & Steim, 1982). With the development of seismic observation techniques and accumulation of modern seismic data, several early works on radial Q model of the earth were published: SL8 (Anderson & Hart, 1978), PREM (Dziewonski & Anderson, 1981), QM1(Widmer *et al.*, 1991), and QL6 (Durek & Ekström, 1996). These pioneering studies identified several important features of radial Q structures: (1) shear quality factor (Q_μ) are orders of magnitude stronger than bulk quality factor (Q_κ) in the mantle; (2) beneath a high-Q lithosphere, a low-Q zone exists in the upper most mantle between 80 and 200 km. Q values in lower mantle were less well resolved than in the upper mantle.

In addition to the depth dependence of Q, frequency dependence of Q has also been observed base upon observations of free oscillations across a wide range of frequencies including Chandler wobble (e.g., Smith & Dahlen, 1981), decay of normal mode peaks and amplitude attenuation of surface waves and body waves. The frequency dependence coefficient α is constrained to the range of 0.1 – 0.4, indicating Q only weakly depends on frequency in the frequency band of seismic observations (e.g., Karato & Spetzler, 1990). An absorption band in the seismic frequency range can be modeled using standard linear solids, which represent solid-state mechanisms of relaxation with a spectrum of relaxation times (Liu *et al.*, 1976; Anderson & Minster, 1979; Anderson & Given, 1982). The associated microscopic mechanism of anelastic behavior in mantle rocks and minerals have been investigated in laboratory under high temperature and pressure. Experiments of mantle minerals showed dislocation motion and grain boundary process, which have a wide range of characteristic relaxation times, are dominant mechanisms for frequency-dependent anelasticity.

In the past decades, progresses in experiment techniques have allowed mineralogists to investigate the elastic and anelastic properties of materials at mantle temperature and pressure. Laboratory studies showed that seismic wave speed and anelasticity have very different sensitivities to variations in temperature, composition, and water content. Therefore, wave speed and Q model together can provide good constraints on distinguishing between chemical and thermal origins of heterogneities in

deep earth. However, seismic tomography of 3-D Q structure remains a challenging task due to difficulties in separating elastic focusing effects on seismic amplitudes from intrinsic attenuation. With recent development in advanced numerical method for 3-D wave propagation and high-performance parallel computing, now it is possible to investigate the effects of 3-D Q on surface wave propagation through numerical experiments. In following sections, we will briefly review laboratory studies in anelasticity of mantle materials, current 3-D global tomography of Q models, as well as numerical method used in this study to simulated wave propagation.

1.2 Laboratory studies of anelasticity

In mineral physics, anelasticity is due to irreversible processes including point defects, diffusion, dislocations and grain boundary sliding in response to stresses associated with seismic waves. These microscopic processes are dependents on temperature, pressure, grain size and composition of earth materials. Understanding the dependence of anelasticity on these controlling factors therefore can shed a light upon physical/chemical heterogeneities in deep earth interior.

Laboratory studies on high-temperature plasticity of olivine and olivine-rich rocks have been carried out since the late 1960s. Experiments on olivine poly-crystals showed that their response to an applied stress is characterized by three distinct regimes: instantaneously elastic response, recoverably anelastic response and permanent viscous deformation. The time dependent strain is accompanied with relaxation of modulus. The characteristic relaxation time, τ, depends upon temperature and grain size, and can be expressed as

$$\tau(T, P, d) = A\ d^m\ e^{\frac{E^* + P\ V^*}{RT}}, \tag{1.2}$$

where A is a constant, E^* is the activation energy, V^* is activation volume, P is pressure, R is gas

constant, T is absolute temperature, d is the grain size and m is the exponent. The dimensionless quality factor associated with energy dissipation is a function of frequency and relaxation time, and can be written as

$$Q(\omega, T, P, d) = A\ d^m\ \omega^\alpha\ e^{\frac{\alpha(E^* + P\ V^*)}{RT}}. \tag{1.3}$$

Early experimental studies of anelasticity of mantle rocks were normally done at high temperatures and ambient pressure due to limited laboratory techniques. Berckhemer *et al.* (1982) investigated temperature dependence of Q in polycrystalline rocks composed by forsterite and dunite, and estimated the activation energy in their experiment to be $E^* = 700$ kJ mol^{-1}. The pressure dependence was ignored due to difficulty in obtain high temperature and high pressure simultaneously in laboratory. One interesting result of their study is that when temperature crosses the solidus, the anelasticity does not show a drastic change although modulus does, which implies that partially molten rock in earth may result in very different behavior in seismic velocity and anelasticity. Gueguen *et al.* (1989) also made pioneering experiments on anelasticity at seismic frequency and high temperature, ambient pressure. They measured shear modulus and Q of a single-crystal forsterite from room temperature to 1400°C. The activation energy E^* estimated in their experiment is approximately 440 kJ mol^{-1}, and pressure dependence was not considered . In addition, the frequency dependence coefficient of Q was estimated to be $\alpha = 0.2$.

Jackson *et al.* (1992) developed an apparatus which for the first time simultaneous high temperature (1000°C) and high pressure (0.3 GPa) experiment was made possible in laboratory, therefore allowed experimental study of minerals at upper mantle condition. Exponential temperature dependence of Q, which is comparable to the result in Gueguen *et al.* (1989), was observed in their dunite samples. Frequency dependent coefficient α is measured to be 0.17. Jackson *et al.* (2002) have again measured the shear modulus and Q^{-1} at periods from 1 to 100 seconds for polycrystalline olivine. In their experiments, the behavior of specimens is essentially elastic when the temperature is less than

$900°$C. At higher temperature, the anelasticity increases, showing an absorption band behavior with frequency exponent α of $0.23 \sim 0.28$. Activation energy E^* is estimated to be in a range from 397 to 495 kJ mol^{-1}, depending on the temperature of measurements.

In addition to temperature, experimental studies show that grain size, composition and wave content may also play important roles in anelasticity. Measuring Q_μ^{-1} as a function of grain size was first done by Jackson *et al.* (2002). In their experiments, average grain size varies from 2.9 μm to 23.4 μm, the finer the grain size, the greater is Q_μ^{-1} at a given temperature and period. They estimate the exponent of grain size dependence m is about 0.28. Compared with shear wave speed, anelasticity is less sensitive to composition. In the experiments of Faul & Jackson (2005), grain boundary in sample minerals may contain different trace elements such as Ca, $\mathrm{Al}$and Tiin San Carlos olivine or trace element free in Sol-Gel olivine, but no resolvable difference of anelasticity is found. This makes anelasticity a good measure of lateral temperature variations in the absence of melt. The effects of water on the anelasticity of olivine has not been investigated comprehensively in laboratory experiments, but Q measurements from hydrous and dehydrated samples suggest that the influence is possibly significant (Jackson *et al.*, 1992).

1.3 Seismic tomography of 3-D anelasticity

In order to understand physical and chemical states of earth interior, it is essential to combine both wave speed model and Q model because they have very different sensitivity to temperature, compositional, wave content variations. Over the past decades, 3-D wave speed structures of the earth have been well constrained (e.g., Grand, 1987; Su *et al.*, 1994; Master *et al.*, 1996; Ritsema & Van Heijst, 2000; Zhou *et al.*, 2006), therefore well resolved 3-D Q structure is becoming particularly important for better understanding of earth interior. Although the depth profile of mantle anelasticity is relatively well constrained and 1-D Q models agree reasonably well on gross features, mapping out

3-D anelastic structures of the earth has been very challenging and large discrepancies exist among different 3-D global models (e.g., Dalton *et al.*, 2008).

The first attempts of mapping lateral variations of anelasticity at global scale were based upon a small dataset of fundamental mode Rayleigh waves at periods of 100 to 300 seconds (Romanowicz, 1995). The resulting model, QR19, imaged upper mantle Q_μ structure down to the depth of 650 km with a relatively low resolution at spherical harmonic degree 6. One prominent feature of this model is that it shows good agreement with surface tectonics (high-Q regions beneath continent and low-Q region beneath oceanic basins). However, focusing effects caused by wave speed structures were not explicitly considered which have been suggested to be significant on amplitudes (e.g., Woodhouse & Wong, 1986; Selby & Woodhouse, 2000). Differential amplitudes of body wave phases have also been used to constrain global Q models. Bhattacharyya *et al.* (1996) measured differential attenuation between SS and S phases to map global upper mantle Q_μ model. In Reid *et al.* (2001), more data set including SS-S and SSS-SS differential attenuation were used to obtain a higher resolution Q_μ model at harmonics degree 8. However, the amplitude ratio of two different phases may subject to strong focusing effects and bias the resulting models (e.g., Ritsema *et al.*, 2002). Warren & Shearer (2002) studied upper mantle Q_κ using the spectra of P and PP waves. With a large fundamental Rayleigh wave data set, Selby & Woodhouse (2002) improved the resolution of upper mantle 3-D Q_μ model to degree 8. They inverted Rayleigh-wave amplitude data measured at periods between 70 and 170 seconds for a set of 3-D Q models with and without correction of focusing effects. The focusing corrections were based upon available phase velocity maps and a linear approximation (Woodhouse & Wong, 1986),

$$\ln A = \frac{1}{2}\text{cosec}\Delta \int_0^\Delta \sin(\Delta - \phi) c_0^{-1} [\sin\theta \partial_\theta^2 - \cos\theta \partial_\theta] \delta c \, d\phi \tag{1.4}$$

where Δ is angular epicenter distance, ϕ is longitude, θ is colatitude and c is the phase velocity. Gung & Romanowicz (2004) used three-component surface-wave waveform data constructed a degree-8

upper mantle Q_μ model, QRLW8. The waveform data are at a broad period range from 60 to 400 second including fundamental-mode and overtone surface waves. Although Q structures in QRLW8 agree with surface tectonics, lateral variations were not well constrained due to a strong damping applied in inversion. The focusing effects on amplitudes were not corrected for as they argued that the effects were probably small. A recently upper mantle Q_μ model QRFSI12 developed by Dalton *et al.* (2008), expanded the resolution of 3-D Q model to spherical harmonics degree 12 using amplitudes of fundamental-mode Rayleigh waves measured at period of 50 to 250 seconds. Focusing effects on amplitudes were shown to be strong and were corrected based upon rat theory (Dalton & Ekström, 2006).

Although elastic focusing effects have received growing attention recently and have been accounted for in some studies using a ray theory, the effects of anelasticity on surface wave travel times and amplitudes have not been well understood. In addition, ray theory used in current 3-D tomography may no longer be valid when imaging heterogeneities at length scales smaller than seismic wave lengths (Zhou *et al.*, 2004). The effects of measurement techniques which may have important impacts on amplitude measurements can not be accounted for in ray theory tomography. It's not surprising that current available 3-D Q models differ greatly from each other (Dalton *et al.*, 2008).

1.4 Wave propagation in 3-D Earth models

In this thesis, I investigate surface wave propagation in 3-D wave speed models and 3-D anelastic models based upon numerical simulations using a Spectral Element Method (SEM). This is a well-developed numerical method which was first introduced in modeling fluid dynamics (Patera *et al.*, 1984). It's characterized by the flexibility of finite-element method and accuracy of spectral method, and has becoming widely used in seismology, especially in 3-D global and regional seismic wave propagation. The Spectral Element Method used in this thesis was first introduced in seismology

by Komatitsch & Tromp (1999) in which the free surface and main internal discontinuities of the Earth have been honored. In order to investigate anelastic effects on seismic waves, Savage *et al.* (2010) incorporated 3-D anelasticity into SEM using a series of Standard Linear Solids. The standard linear solid is a physical model consists of a spring and a parallel Maxwell solid (spring and dashpot connected in series) to represent relaxation behavior of stress and strain in anelastic material. Each standard solid has a characteristic relaxation time therefore a series of them can approximate the absorption band of Q in seismic frequency range. Using this numerical method, we simulate wave propagations in earth models with and without 3-D wave speed structures to investigate their effects on travel times and amplitudes of surface waves. Similar simulations will run for earth models with and without 3-D Q structures to quantify anelastic effects on surface waves.

1.5 Summary of thesis chapters

Lateral variations in anelasticity (Q) provide important constraints complementary to 3-D wavespeed variations in mapping 3-D thermal and compositional structures in the mantle. In this thesis, effects of lateral variations on wave speed and anelasticity (Q) on seismic surface waves are investigated quantitatively through wave propagation simulations. In present-day joint tomographic inversions of global velocity and anelasticity (Q) structure, 3-D anelastic dispersion effects on surface waves have been ignored. In Chapter 2, we quantifed the effects of 3-D Q structure on surface-wave phase delays by simulating wave propagation in 3-D wavespeed and 3-D Q models using a spectral element method (SEM). We compared phase delays caused by 3-D Q structure and those caused by 3-D wave speed structure. Our results showed that (1) roughly 15-20 percent of the observed phase delays (travel times) in long-period surface waves are due to 3-D Q structure; this implies that neglecting 3-D anelastic dispersion effects can lead to biased wave speed models in seismic tomography; (2) the effects of Q perturbations on surface-wave phase delays are frequency dependent as a result of

local S-wave anelastic dispersion, frequency-dependent depth sensitivity of surface waves as well as the 3-D distribution of Q anomalies. In my numerical experiments, the significance of 3-D anelastic dispersion increases with wave period, and the frequency dependence is most apparent in the period range between 60 – 150 seconds and becomes weaker at 150 – 200 seconds and (3) assuming a thermal origin, anelastic delays caused by "hot" anomalies (or advances caused by "cold" anomalies) are correlated with elastic delays (or advances), but their relation is not linear: the ratio between anelastic and elastic delays (or advances) becomes larger for "hotter" anomalies than for "colder" anomalies.

In Chapter 3, I investigate the effects of lateral perturbations in velocity and anelasticity (Q) on surface-wave amplitudes based upon wave propagation simulations in 3-D Earth models using a Spectral Element Method (SEM). We constructed 3-D Q models based upon a wave speed model S20RTS using a set of reasonable mineralogical parameters assuming lateral variations in both wave speed and anelasticity are due to temperature perturbations. We measured and compared amplitude perturbations of surface waves caused by 3-D wave speed (elastic) structures and those caused by 3-D anelastic (Q) structures at a period range of 50-200 s. The measurements showed that the influence of 3-D wave speed structures on amplitudes is comparable to that of 3-D Q structures at short period, but becomes dominant at long period. In ray-theoretical framework, surface wave amplitudes can be decomposed into three terms, elastic focusing, anelastic attenuation, and anelastic focusing which depends respectively upon the roughness of phase velocity perturbations ($\partial_y^2 \delta \ln c$), perturbations in anelasticity ($\delta \ln Q^{-1}$), and the roughness of perturbations in anelasticity ($\partial_y^2 \delta \ln Q^{-1}$). Theoretical calculations confirmed the relative importance of 3-D Q and 3-D wave speed in perturbing surface-wave amplitudes: (1) in short-period (~ 50 s) surface waves, anelastic attenuation effects are comparable to elastic focusing effects caused by 3-D wave speed structures; and (2) in long-period ($>$ 100 s) surface waves, elastic focusing effects are dominant, stronger than anelastic attenuation as it decreases rapidly with increasing wave period; and (3) anelastic focusing effects, which have been ig-

nored in present-day tomographic studies, have a more significant effect than attenuation. Therefore, the effects of 3-D Q structures can be "counter-intuitive" at long period for surface waves traveling through a low-Q region may experience amplitude increase.

Surface wave tomography inversions based upon ray theory have resolution limits, when the length scale of heterogeneities is less than seismic wavelength finite frequency effects become important and need to be considered. In Chapter 4, we investigate finite frequency effects of surface waves in 3-D wave speed and 3-D anelasticity (Q) earth models. We simulate wave propagation in the models using a Spectral Element Method (SEM) and measure travel time and amplitude perturbations caused by lateral variations in wave speed and anelasticity for Rayleigh waves at period range of 50 s – 200 s. Comparisons between the "ground truth" SEM measurements with those predicted using ray theory and finite frequency theory show that finite frequency effects are stronger in surface-wave amplitudes than in travel times, especially at long periods.

Bibliography

Anderson, D. L., & Archambeau, C. B., 1964. The anelasticity of the Earth, *J. geophys. Res.*, , **69**, 2071-2084.

Anderson, D. L., 1976. The anelasticity of the mantle, *Geophys. J. R. astr. Soc.*, , **14**, 135-164.

Anderson, D. L. & Hart, R. S., 1978. Q of the Earth, *J. geophys. Res.*, **83**, 5869- 5882.

Anderson, D. L. & Minster, J. B., 1979. The frequency dependence of Q in the Earth and implications for mantle rheology and Chandler Wobble. *Geophys. J. R. astr. Soc.*, **58**, 431-440.

Anderson, D. L. & Given, J. W., 1982. Absorption band Q model for the earth, *J. geophys. Res.*, **87**, 3893-3904.

Bhattacharyya, J., Masters G., and Shearer P., 1996. Global lateral variations of shear wave attenuation in the upper mantle, *J. geophys. Res.,* **101**, 22,273-22,289.

Berckhemer, H., W. Kampfman, E. Aulbach, and H. Schmeling, 1982. Shear modulus and Q of forsterite and dunite near partial melting from forced oscillation experiments, *Phys. Earth planet. Inter.,* **29**, 30-41.

Canas, J. A. & Mitchell, B. J., 1978. Lateral variation of surface wave anelastic attenuation across the Pacific, *Bull. seism. Soc. Am.,* **68**, 1637-1650.

Canas, J. A. & Mitchell, B. J., 1981. Rayleigh-wave attenuation and its variation across the Atlantic Ocean, *Geophys. J. R. astr. Soc.,* **67**, 259-276

Dalton, C. & Ekström, G., 2006. Global models of surface wave attenuation, *J. geophys. Res.,* **111**, B05317, doi:10.1029/2005JB003997.

Dalton, C., Ekström, G. & Dziewoński, A. M., 2008. The global attenuation structure of the upper mantle, *J. geophys. Res.,* **113**, B09303, doi:10.1029/2007JB005429.

Deschamps, A., 1977. Inversion of the attenuation data of free oscillations of the earth (fundamental and first higher modes), *Geophys. J. R. astr. Soc.,* **50**, 699-722.

Durek, J. J., and Ekström, G., 1996. A radial model of anelasticity constraint with long-period surface wave attenuation, *Bull. seism. Soc. Am.,* **86**, 144-158.

Dziewonski, A. M. & Anderson, D. L., 1981. Preliminary reference Earth Model, *Phys. Earth planet. Inter.,* **25**, 297-356.

Dziewonski, A. M. & Anderson, D. L., 1982. Dispersion and attenuation of mantle waves from wave-form inversion, *Geophys. J. R. astr. Soc.,* **70**, 503-527.

Faul, U. H. & Jackson, I., 2005. The seismological signature of temperature and grain size variations in the upper mantle, *Earth planet. Sci. Lett.,* **234**, 119-134.

Grand, S. P., 1987. Tomographic inversion for shear velocity beneath the North American plate. *J. geophys. Res.,* **92**, 14,065-14,090.

Gueguen, Y., M. Darot, P. Mazot, and J. Woirgard, Q^{-1} of forsterite single crystals, *Phys. Earth planet. Inter.,* **55**, 254-258.

Gung, Y. & Romanowicz, B., 2004. Q tomography of the upper mantle using three-component long-period waveforms, *Geophys. J. Int.,* **157**, 813-830.

Jackson, I., 2000. Laboratory Measurements of Seismic Wave dispersion and Attenuation: Recent Progress., in *Earth's Deep Interior: Mineral Physics and Tomography from the Atomic to the Global Scale, AGU Geophysicsl Monograph Service*, vol.**117**, S. Karato *et al.* (eds), 265-289.

Jackson, I., M. S. Paterson, and J. D. Fitz Gerald, 1992. Seismic wave attenuation in Aheim dunite: An experiment study, *Geophys. J. Int.,* **108**, 517-534.

Jackson, I., J. D. Fitz Gerald, U. H. Faul, and B. H. Tan, 2002. Grain-size-sensitive seismic wave attenuation in polycrystalline olivine, *J. geophys. Res.,* **107**B(12), 2360, doi:10.1029/2001JB001225.

Kanamori, H. & Anderson, D.L., 1977. Importance of physical dispersion in surface-wave and free-oscillation problems: Review. *Rev. Geophys. Space Phys.*, **15**, 105–112.

Karato, Shun-ichiro, 1993. Importance of anelastic in the interpretation of seismic tomography, *Geophys. Res. Lett.,* **20**, NO. 15, 1623-1626.

Karato, S. & Spetzler., H. A., 1990. Defect microdynamics in mineral and solid-state mechanisms of seismic wave attenuation and velocity dispersion in the mantle, *Rev. Geophys.,* **28**, 399-421.

Komatitsch, D. & Tromp, J., 1999. Introduction to the spectral-element method for 3-D seismic wave propagation, *Geophys. J. Int.,* **139**, 806-822.

Komatitsch, D. & Tromp, J., 2002. Spectral-element simulations of global seismic wave propagation—I. Validation, *Geophys. J. Int.,* **149**, 390-412.

Liu, H. P., Anderson, D. L. & Kanamori, H., 1976. Velocity dispersion due to anelasticity; implications for seismology and mantle composition, *Geophys. J. R. astr. Soc.*, **47**, 41-58.

Master, G., Johnson, S., Laske, G., & Bolton, H., 1996. A shear-velocity model of the mantle, *Phil. Trans. R. Soc. Lond.* A, **354**, 1385-1411.

Patera, A. T., 1984. A spectral element method for fluid dynamics: Laminar flow in a channel expansion, *J. Comput. Phys.,* **54**, 468-488.

Reid, F. J. L., Woodhouse, J. H., & van Heijst, H. J., 2001. Upper mantle attenuation and velocity structure from measurements of differential S phases, *Geophys. J. Int.,* **145**, 615-630.

Ritsema, J. & Van Heijst, H. J., 2000. Seismic imaging of structural heterogeneity in Earth's mantle: Evidence for large-scale mantle flow, *Science Progress*, **83**, 243-259.

Ritsema, J., Rivera, L. A., Komatitsch, D., Tromp, J. & van Heijst, H. J., 2002. Effects of crust and mantle heterogeneity on PP/P and SS/S amplitude ratios, *Geophys. Res. Lett.,* **29(10)**, 1430, doi:10.1029/2001GL013831

Romanowicz, B., 1995. A global tomographic model of shear attenuation in the upper mantle, *J. geophys. Res.,* **100**, 12,375-12,394

Sailor, R. V. & Dziewonski, A. M., 1978. Measurements and interpretation of normal modes attenuation. *Geophys. J. R. astr. Soc.,* **53**, 559-581.

Sato, Y., 1958. Attenuation, dispersion of and the wave guide of G wave, *Bull. seism. Soc. Am.,* **48**, 231-251.

Savage, B., Komatitsch, D., & Tromp, J., 2010. Effects of 3D attenuation on seismic wave amplitude and phase measurements, *Bull. seism. Soc. Am.,* **100**, No. 3, 1241-1251, 10.1785/0120090263.

Selby, N. D. & Woodhouse, J. H., 2000. Controls on Rayleigh wave amplitudes: Attenuation and focusing, *Geophys. J. Int.,* **142**, 933-940.

Selby, N. D. & Woodhouse, J. H., 2002. The Q structure of the upper mantle: Constraints from Rayleigh wave amplitudes, *J. geophys. Res.,* **107**, NO. B5, 2097, 10.1029/2001JB000257.

Smith, M. L. & Dahlen, F. A., 1981. The period and Q of the Chandler wobble, *Geophys. J. Int.,* **64**, 223-281.

Su, W.-J., Woodward, R. L., and Dziewonski, A. M., 1994. Degree 12 model of shear velocity heterogeneity in the mantle. *J. geophys. Res.,* **99**, 6945-6980.

Tan, B. H., I. Jackson, and J. D. Fitz Gerald, 1997. Shear wave dispersion and attenuation in fine-grained synthetic olivine aggregates: Preliminary result, *Geophys. Res. Lett.*, **24**, 1055-1058.

Tan, B. H., I. Jackson, and J. D. Fitz Gerald, 2001. High-temperature viscoelastocoty of fine-grained polycrystalline olivine, *Phys. Chem. Minerals,* **28**, 641-664.

Warren, L. M., & Shearer, P. M., 2002. Mapping lateral variation in upper mantle attenuation by stacking P and PP spectra, *J. geophys. Res.,* **107(B12)**, 2342, doi:10.1029/2001JB001195.

Widmer, R. G., Masters, G., & Gilbert, F., 1991. Spherically symmetric attenuation within the Earth from normal mode data., *Geophys. J. Int.,* **104**, 541-553.

Woodhouse, J. H. & Wong, Y. K., 1986. Amplitude, phase and path anomalies of mantle waves, *Geophys. J. R. astr. Soc.,* **87**, 753-773.

Zhou, Y., Dahlen, F. A. & Nolet, G., 2004. Three-dimensional sensitivity kernels for surface wave observables, *Geophys. J. Int.*, **158**, 142-168.

Zhou, Y., Nolet, G., Dahlen, F. A. & Laske, G., 2006. Global upper-mantle structure from finite-frequency surface-wave tomography, *J. geophys. Res.*, **111** B04304, doi:10.1029/2005JB003677.

Chapter 2

The effects of 3-D anelasticity (Q) structure on surface wave phase delays

(An edited version of this chapter has published by RAS. Ruan, Y. and Zhou Y., The effects of 3-D anelasticity (Q) structure on surface wave phase delays, 2010, *Geophys. J. Int.*, **181**, 479-492.)

2.1 Introduction

In the past decades, lateral variations in seismic wavespeeds in the mantle have been mapped out at a global scale by seismic tomographic studies (e.g. Grand, 1987; Su *et al.*, 1994; Master *et al.*, 1996; Ritsema & Van Heijst, 2000; Zhou *et al.*, 2006). It is known that using only wavespeed structure in the upper mantle is not possible to distinguish between thermal and chemical origins of mantle heterogeneities. The anelasticity (Q) structure of the Earth's mantle is very sensitive to temperature perturbations, therefore lateral variations in Q can be applied as a valuable constraint complementary to 3-D wavespeed structure to understand the thermal and chemical variations as well as the dynamics

of the Earth's interior.

The effects of anelasticity on the Earth's free oscillations as well as on propagating surface waves and body waves have been documented in the 1970s (e.g., Liu *et al.*, 1976; Kanamori & Anderson, 1977). Several one-dimensional (radial) Q models have been developed (e.g., Dziewonski & Anderson, 1981) and widely used in today's seismological studies. However, compared to 3-D wavespeed tomography, studies of 3-D anelasticity (Q) structure in the mantle have been lagging behind. In the past two decades, efforts have been made to image the 3-D anelasticity structure in the mantle using both surface waves (e.g., Romanowicz, 1995; Selby & Woodhouse, 2002; Gung & Romanowicz, 2004; Dalton *et al.* , 2008) and body waves (e.g., Reid *et al.*, 2001; Warren & Shearer, 2002). In the upper mantle, lateral variations in Q differ considerably among those models (e.g., Dalton *et al.* , 2008). These discrepancies are partly due to the fact that seismic amplitudes can be affected by both 3-D anelastic structure as well as 3-D elastic wavespeed structure through wave focusing and defocusing. It is difficult to separate the two contributing effects and different research groups often take different approaches in handling the focusing and defocusing effects in tomographic practices (e.g., Selby & Woodhouse, 2000; Dalton *et al.* , 2008). The importance of a joint inversion of 3-D velocity and Q using both amplitude and phase delay measurements has been appreciated in several recent surface-wave studies (e.g., Billien *et al.*, 2000; Dalton *et al.* , 2008), however, the effects of 3-D Q structure on surface-wave phase delays have so far received little attention. The focus of this chapter is to quantify the effects of 3-D anelastic structures on surface-wave phase delays, in particular, how do phase delays caused by 3-D Q structure compared with phase delays caused by 3-D wavespeed structure.

It is known that lateral compositional heterogeneities in the mantle have only secondary effects on seismic wavespeed and anelasticity (e.g. Faul & Jackson, 2005). In this study, we construct our 3-D Q models using a 3-D wavespeed model S20RTS of Ritsema & Van Heijst (2000), assuming that both velocity and Q perturbations are due to temperature variations. We simulate wave propagation

in 3-D global models using the Spectral Element Method (Komatitsch & Tromp, 1999, 2002), and we measure phase delays between fundamental-mode surface waves generated in earth models with and without the presence of 3-D Q structures. The same wave propagation experiments are done for earth models with and without 3-D wavespeed structures to measure phase delays caused by 3-D wavespeed structure. Comparisons between phase delays caused by 3-D wavespeed and 3-D Q structure show that roughly 15-20$\%$ of the observed phase delays (travel times) in long-period surface waves are due to 3-D anelasticity (Q) structure. This result agrees with estimates made based upon 3-D sensitivity kernels (Zhou, 2009). We show that 3-D anelastic effects are dependent upon mineralogical parameters applied in generating global Q models. We investigate 3-D anelastic dispersion effects in continental and oceanic paths and the non-linear relation between delay times caused by "elastic" and "anelastic" mechanisms.

2.2 Quality factor Q and Anelastic Dispersion

The effects of the anelasticity of Earth material on seismic waves can be accounted for by considering the relaxation of elastic moduli. The relaxation of elastic moduli is associated with energy dissipation (internal friction) of seismic waves and can be characterized by the quality factor Q – energy loss per cycle. It is known that anelasticity affects seismic waves in two aspects: amplitude attenuation and anelastic dispersion; and the latter describes variations of wave speed with frequency. These effects can be accounted for by using complex and frequency dependent moduli (Dahlen & Tromp, 1998):

$$\mu \rightarrow \mu_0 \, [1 + \frac{2}{\pi} \, {Q_\mu}^{-1} \, \ln(\frac{\omega}{\omega_0}) \, + \, i \, {Q_\mu}^{-1}], \tag{2.1}$$

$$\kappa \rightarrow \kappa_0 \, [1 + \frac{2}{\pi} \, {Q_\kappa}^{-1} \, \ln(\frac{\omega}{\omega_0}) \, + \, i \, {Q_\kappa}^{-1}], \tag{2.2}$$

where μ_0 and κ_0 are the shear and bulk moduli at a reference frequency ω_0, and Q_μ and Q_κ are the corresponding quality factors. The imaginary part of the modulus in equations (2.1) and (2.2) represents amplitude attenuation, and the frequency-dependent real part describes velocity dispersion. In this study, we shall focus on seismic wave propagation speeds in the presence of 3-D Q structure. The effects of anelasticity on surface-wave amplitudes will be discussed in chapter 3. To the first order, the real part of the complex moduli in equations (2.1) and (2.2) leads to dispersion of wave speed $V(\omega)$ and can be written as (Dahlen & Tromp, 1998)

$$V(\omega) = V(\omega_0) \left[1 + \frac{1}{\pi Q} \ln\left(\frac{\omega}{\omega_0}\right)\right], \tag{2.3}$$

where $V(\omega_0)$ is the wave speed at a reference frequency ω_0, and Q is the quality factor.

The relaxation of stresses and strains in wave propagation is a result of irreversible changes of crystal defect structures and grain boundaries of Earth material. Assuming thermally activated processes, the quality factor Q is dependent upon rheology parameters of the material, mantle temperature and pressure as well as the frequency of the wave (e.g., Jackson & Anderson, 1970; Karato & Spetzler, 1990),

$$Q(\omega, T) = A\, \omega^{\alpha} \exp\left[\frac{\alpha\,(E^* + PV^*)}{R\,T}\right], \tag{2.4}$$

where E^* and V^* are the activation energy and activation volume of anelastic relaxation, respectively. These rheology parameters can be measured in experimental studies for upper mantle material (e.g., olivine), and they vary in a relatively wide range (e.g., Béjina *et al.*, 2003). Under upper mantle condition, the activation energy E^* of olivine varies from 300 KJ/mol to 500 KJ/mol, and the activation volume V^* ranges from 5 cm^3/mol to 30 cm^3/mol (Jackson *et al.*, 2002). A is a constant associated with properties of the material such as the grain size (Jackson *et al.*, 2002; Faul & Jackson, 2005) and R is the gas constant. From both mineral physics experiments and seismological observations, Q ex-

hibits only weak dependence upon frequency and the coefficient α is roughly between 0.1–0.4 and it does not vary significantly with temperature (e.g., Anderson & Minster, 1979; Smith & Dahlen, 1981; Karato & Spetzler, 1990; Jackson & Paterson, 1993; Jackson, 2000; Shito *et al.*, 2004). In surface-wave studies, resolving the frequency dependence of Q is still a challenging task and a constant Q absorption-band model (e.g., Liu *et al.*, 1976; Kanamori & Anderson, 1977) has been widely used in wave propagation simulations as well as in inversions of velocity and Q structures (e.g., Dziewonski & Anderson, 1981; Komatitsch & Tromp, 1999; Dalton *et al.* , 2008). In this study, we neglect the weak frequency dependence of Q in wave propagating experiment and the temperature and pressure dependence of Q can be re-written as

$$Q(\omega, T) = A \ \exp\left[\frac{\alpha\,(E^* + PV^*)}{R\,T}\right]. \tag{2.5}$$

2.3 Wave propagation in 3-D Q and 3-D velocity models

The focus of this chapter is to simulate wave propagation in 3-D wavespeed earth models and 3-D Q models and compare the effects of 3-D wavespeed variations and the effects of 3-D Q perturbations on surface-wave phase delays. In this study, we construct our 3-D tomographic-like Q model using a 3-D wavespeed model S20RTS of Ritsema & Van Heijst (2000), assuming that both velocity and Q perturbations are due to temperature variations.

2.3.1 1-D reference Q model

Model S20RTS describes S-wave velocity perturbations in the mantle with respect to the Preliminary Reference Earth Model (PREM) (Dziewonski & Anderson, 1981). A radial Q structure has been incorporated in the model. In this study, we assume a thermally activated Q mechanism and con-

struct self-consistent reference radial (1-D) Q profile and lateral (3-D) variations using eq. (2.5). In constructing the reference radial (1-D) Q model, we use a reference geotherm in the upper mantle assuming a half-space cooling mantle,

$$T(z) = T_s + (T_m - T_s)\,\mathrm{erf}\left(\frac{z}{2\sqrt{\kappa\tau_c}}\right), \tag{2.6}$$

where the surface temperature T_s is assumed to be $0\,^\circ\mathrm{C}$ and the mantle temperature T_m is assumed to be $1300\,^\circ\mathrm{C}$. We use a thermal diffusivity κ of $1\times10^{-6}\mathrm{m}^2/\mathrm{s}$ and a cooling age τ_c of 60 Myr. An adiabatic thermal gradient of $0.5\,^\circ\mathrm{C}/\mathrm{km}$ is added throughout the mantle. The reference mantle temperature profile is plotted in Fig. 2.1. It is noteworthy that these geothermal parameters are not well constrained, and parameters are chosen based on current estimates to produce a reasonable globally-averaged geotherm in the upper mantle (e.g., Shapiro & Ritzwoller, 2004; Faul & Jackson, 2005).

Based upon the 1-D background temperature model, we calculate a reference 1-D Q model using equation (2.5) with the following rheology parameters: activation energy $E^*=470$ KJ/mol, activation volume $V^* = 17$ cm^3/mol and α value of 0.1. We use the radial pressure profile in model PREM in constructing our reference radial Q structure, and choose a constant $A = 1.394$ such that our 1-D reference Q model is close to PREM. In Fig. 2.1, we plot our reference Q model together with the 1-D Q structure in PREM in the top 400 km. In the uppermost 80 km, PREM has a constant Q value of 600, while Q values in our reference model decrease from over 1000 to 150 due to the exponential temperature dependence. Considering that the lithosphere is cold and mostly elastic, and anelasticity is related to $1/Q$ rather than Q, it is safe to use high Q values in the lithosphere. Even though it is reasonable to assume a mostly elastic lithosphere, especially in the top 50 km, we discuss the effects of low Q values in the lithosphere in section 2.4. At the depth range of $80-220$ km, Q values in our model are very close to PREM, except for that there are two sharp discontinuities at depths of 80 km and 220 km in model PREM. Between 220 km and 300 km, our 1-D Q model shows slightly lower

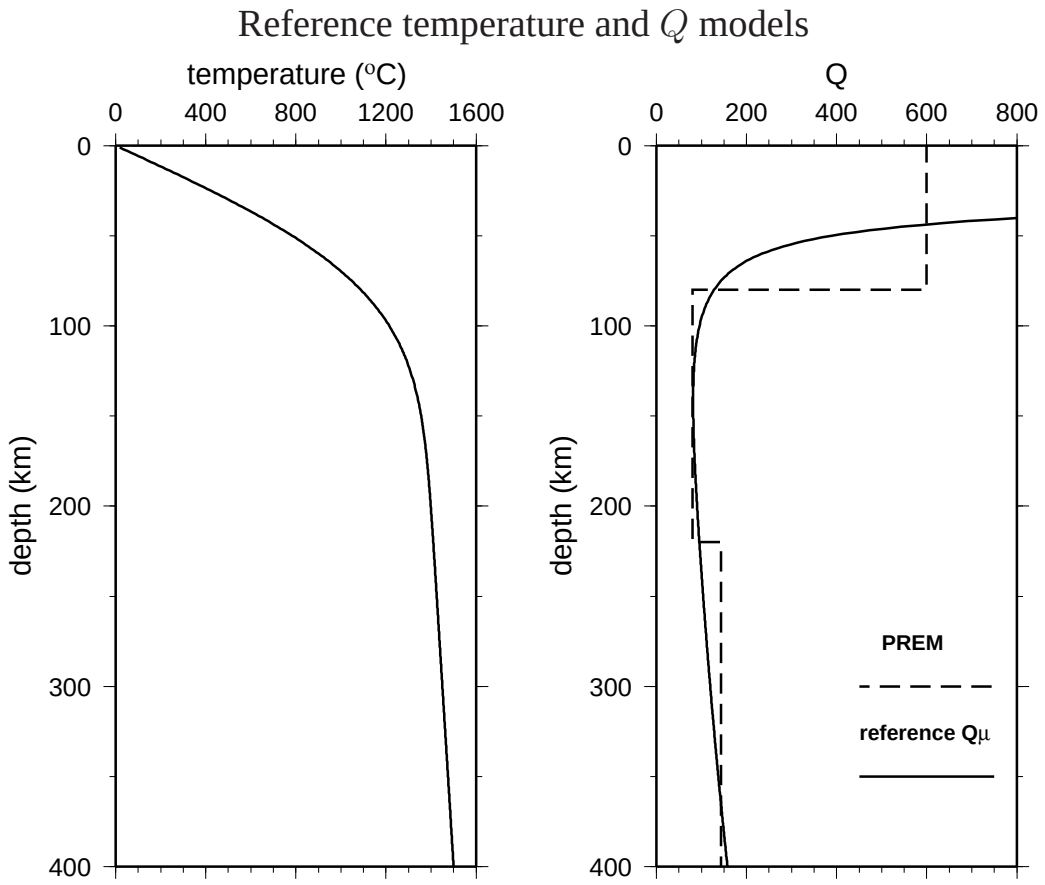

Figure 2.1: (a) Reference geotherm assuming a half-space cooling model with mantle temperature $T_M = 1300\,^{\circ}C$ and cooling age $\tau_c = 60$ Myr. An adiabatic thermal gradient $0.5\,^{\circ}C/$km has been added throughout the mantle. Only the uppermost 400 km of the profile is plotted. (b) Reference Q model (Q_μ) derived using the temperature model and mineralogy parameters $E^* = 470$ KJ/mol and $V^* = 17$ cm^3/mol. PREM Q_μ profile is plotted in dashed line for reference.

Q values than PREM. Overall, our reference 1-D Q model constructed using eq. (2.5) is very close to PREM Q model.

2.3.2 3-D Q models

In this study, we construct a 3-D tomographic-like Q model using a 3-D wavespeed model S20RTS. Assuming thermally activated processes of velocity and Q perturbations, wavespeed is dependent

upon both temperature and wave frequency (Kanamori & Anderson, 1977; Karato, 1993),

$$V(\omega, T) = V_0(T)\left[1 + \frac{1}{Q\pi}\frac{E^* + PV^*}{RT} + \frac{1}{Q\pi}\ln\omega\tau_0\right], \tag{2.7}$$

where τ_0 is a constant in the order of 10^{-12} to 10^{-13} sec, approximately the period of the fundamental thermal vibrations for atomic relaxation (Jackson & Anderson, 1970), and V_0 is the "anharmonic" elastic velocity which corresponds to the seismic velocity at $Q = \infty$. Taking derivative of eq. (2.7), to the first order, temperature perturbations can be calculated from velocity perturbations using the temperature partial derivative $\partial \ln V/\partial T$ (Karato, 1993),

$$\frac{\partial \ln V}{\partial T} = \frac{\partial \ln V_0}{\partial T} - \frac{1}{Q\pi}\frac{E^* + PV^*}{RT^2}. \tag{2.8}$$

Note that to the first order, the frequency-dependent term (anelastic dispersion) in eq. (2.7) does not contribute to the temperature partial derivative. The partial derivative $\partial \ln V_0/\partial T \approx -0.76 \times 10^{-4}$ K^{-1} for S waves (Isaak, 1992), and it is insensitive to crystal structures (Duffy & Anderson, 1989). Taking temperature derivative of equation (2.5), fractional perturbations in Q can be calculated from perturbations in temperature T by

$$\frac{\delta Q}{Q} = -\alpha\,\frac{E^* + PV^*}{RT^2}\,\delta T. \tag{2.9}$$

Like many other global velocity models, model S20RTS describes 3-D wavespeed variations in the mantle but has assumed a radial structure of Q (PREM Q structure). This is not self consistent in the sense that lateral variations in temperature should give rise to lateral variations in both velocity and Q. In this study, we compute its corresponding 3-D Q structure using equations (2.8) and (2.9) using an iterative approach: (1) calculate 3-D temperature perturbations δT from the 3-D velocity perturbations in S20RTS using the temperature partial derivative $\partial \ln V_S/\partial T$ assuming a 1-D initial temperature and Q structure as described in sect. 2.3.1, (2) update the local temperature with perturbations obtained

from step (1) and calculate the corresponding perturbations in Q using equation (2.9), (3) update $\partial \ln V_S / \partial T$ in eq. (2.8) using the new temperature and Q values and go back to step (1), iterate until perturbations in temperature and Q converge.

Maps of the 3-D velocity model (S20RTS) and the corresponding 3-D Q model, $\mathbf{Q3DM_M}$, at 100 km depth are shown in Fig. 2.2. The fractional perturbations in $1/Q$ are with respect to our 1-D reference Q model. The resulting 3-D Q model is highly correlated with the 3-D velocity model: mid-ocean ridges are characterized by slow anomalies and lower-than-average Q values, stable continental interiors show fast anomalies and higher-than-average Q values. Compared with recent tomographic 3-D Q models (e.g., Dalton *et al.* , 2008), the strength (rms) of Q perturbations in our 3-D model is comparable to those tomographic studies. For example, perturbations in $1/Q$ at a depth of 100 km are in the range of -0.01 – 0.011 in our model, comparable to -0.0125 – 0.01 in the model of Dalton *et al.* (2008); the corresponding fractional perturbations are in the range of -99.9%– 107.5% in our model, comparable to -100% – 80% in their model. Two-dimensional (2-D) Love-wave as well as Rayleigh-wave Q maps are plotted in Fig. 2.3, which are also comparable to recent 2-D surface-wave Q models (e.g., Dalton & Ekström, 2006).

It is important to point out that we have considered the Q dependence of temperature partial derivative $\partial \ln V / \partial T$ in constructing 3-D temperature and Q variations from 3-D velocity variations. The resulting 3-D earth model are self-consistent in that both Q and velocity are results of 3-D variations in mantle temperature.

2.3.3 Wave propagation in 3-D earth models and phase delay measurements

The effects of lateral thermal anomalies in seismic observables can be modeled by simulating wave propagation in earth models with 3-D velocity (S20RTS) and 3-D Q structures. In this study, we investigate the effects of 3-D wavespeed structure and the effects of 3-D anelastic dispersion separately,

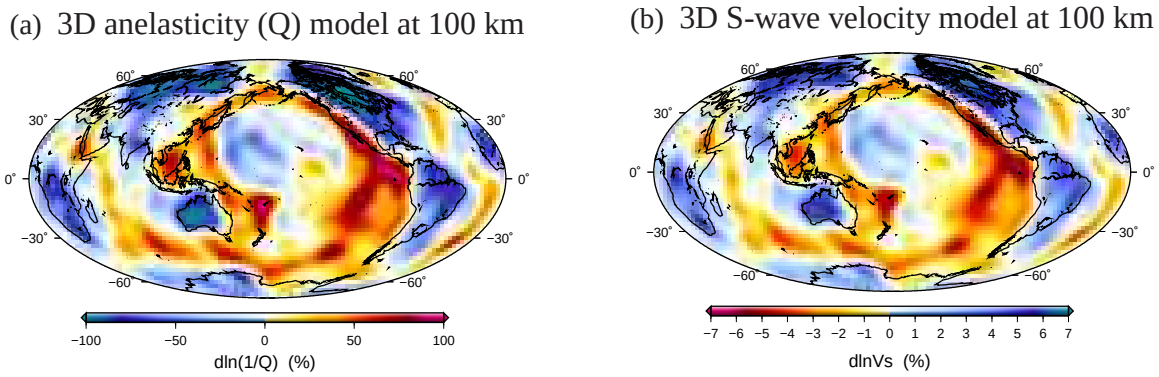

Figure 2.2: (a) 3-D anelasticity model at a depth of 100 km. Fractional perturbations in $1/Q$ are in the range of -99.9% – 107.5%, comparable to recent tomographic models (e.g., Dalton *et al.* , 2008). (b) 3-D shear wave velocity model S20RTS (Ritsema & Van Heijst, 2000) at a depth of 100 km. The 3-D Q model and the 3-D velocity model are correlated as we assume both of them are originated from temperature variations.

and compare long-period surface-wave phase delays caused by 3-D Q structure through 3-D anelastic dispersion with phase delays caused by 3-D elastic wavespeed structure. We simulate wave propagation in 3-D velocity and 3-D Q models using the Spectral Element Method (SEM) (Komatitsch & Tromp, 1999). The SEM incorporated anelasticity in wave propagation using three standard linear solids assuming Q is independent of frequency (absorption-band model). Twelve earthquake events and 801 seismic stations around the world were chosen for our numerical experiments to provide good path coverage.

We simulate wave propagation in four different Earth models (see Table 2.1) for each event. In the case of examining the effects of 3-D wavespeed structure ("3-D elastic effects" hereinafter) on surface-wave phase delays, we measure phase differences between synthetic seismograms generated in model (I) — 1-D velocity and 1-D Q and model (II) — 3-D velocity and 1-D Q. The Q structures in model (I) and (II) are identical, therefore, differences in surface-wave travel times are due to the 3-D velocity structures (elastic delay $= t_{3-\mathrm{D\,V}} - t_{1-\mathrm{D\,V}}$). The 1-D velocity and 1-D Q models used in this case are from PREM (Fig. 2.1) and the 3-D velocity model is S20RTS. In the case of examining the effects of 3-D anelastic dispersion (3-D Q effects), we measure phase differences between seismograms generated in model (III) — 3-D velocity and 1-D Q and model (IV) — 3-D velocity and 3-D

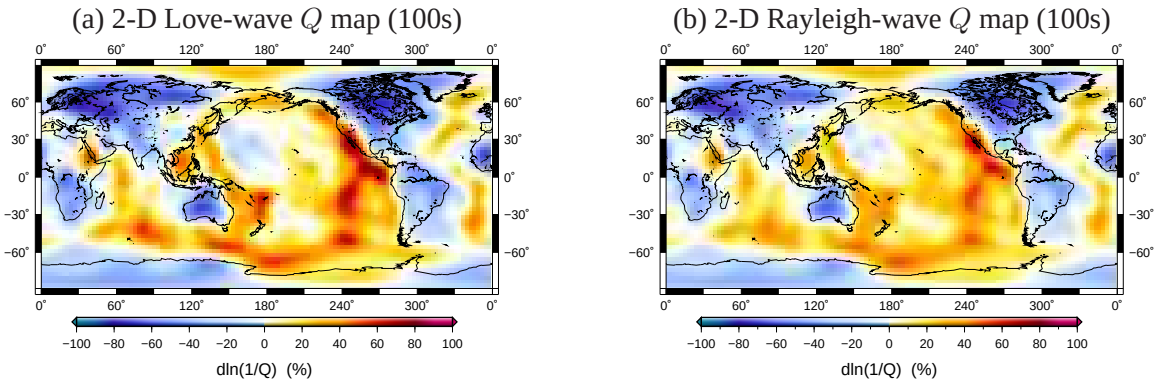

Figure 2.3: Two-dimensional surface-wave Q maps calculated for our 3-D anelastic Earth model. (a) 2-D Love-wave Q map at 100 seconds for our 3-D anelastic Earth model (S20RTS + 3D Q), fractional variations in $1/Q$ are with respect to Love-wave Q in the Earth model with 1-D reference Q structure (S20RTS + 1D Q). Fractional variations in Love-wave $1/Q$ are in the range of $-78.2\% - 85.4\%$. (b) The same as (a) but for 100-second Rayleigh waves, and the fractional variations are between -74.6% and 72.6%.

Table 2.1: Models for 3-D wave propagation

Models	Model No.	Velocity	Anelasticity (Q)
Elastic delay measurement	I	1D (PREM)	1D (PREM)
	II	3D (S20RTS)	1D (PREM)
Anelastic delay measurement	III	3D (S20RTS)	1D ($\mathbf{Q1DM_M}$)
	IV	3D (S20RTS)	3D ($\mathbf{Q3DM_M}$)

Q. In this case velocity structures are the same in the two models, and differences in surface-wave travel times are due to 3-D anelastic perturbations (anelastic delay $= t_{3-\mathrm{D\,Q}} - t_{1-\mathrm{D\,Q}}$). The 1-D Q and 3-D Q models have been described in section 2.3.1 and 2.3.2, and perturbations in the 3-D Q models are comparable to recent tomographic Q models (e.g., Dalton *et al.* , 2008).

Surface-wave phase delays are measured using a multi-taper technique (Laske & Masters, 1996; Zhou *et al.*, 2004). The tapers used in this chapter are five 2.5-π prolate spheroidal eigen-tapers (Slepian, 1978) with narrowly concentrated spectra. Measurements made with this technique show reduced bias in spectral estimates in surface-wave studies (Laske & Masters, 1996). Phase delays and associated errors are estimated by least-square fitting of measurements made with these five orthogonal tapers. We measure fundamental-mode surface-wave phase delays at frequencies (periods) from 5 mHz (200 s) to 20 mHz (50 s). Fundamental-mode surface waves, especially Love waves, can

be contaminated by higher-mode surface waves at short epicentral distances. We carefully choose measurement windows that contain mostly fundamental-mode surface-wave energy to minimize contamination of higher-mode surface waves. Because of the dispersion of surface waves, we filter seismograms at two frequency bands, 50–100s and 100–200s, and choose measurement windows correspondingly. We examine every single measurement and correct/remove measurements with cycle skip problems, this left ~ 7600 minor-arc Love waves and ~ 8500 Rayleigh waves for this study.

For some event-station pairs, seismic waves travel along continent-ocean boundaries where strong velocity contrast can be expected. Surface waves along these paths sometimes show two separate arrivals, one travels in the continental side where seismic velocity is higher than the reference velocity and the other one travels in the oceanic side where seismic velocity is relatively lower. An example of seismogram with apparent multi-pathing signals is plotted in Fig.2.4. In this study, we choose to exclude those paths from our measurements.

(a) Example seismograms of multi-pathing

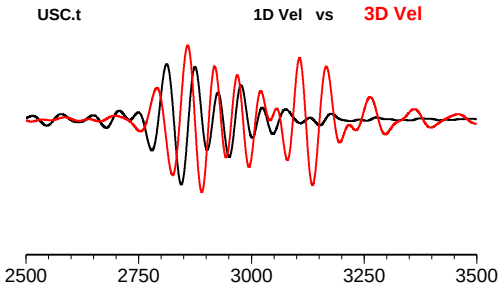

(b) Ray path

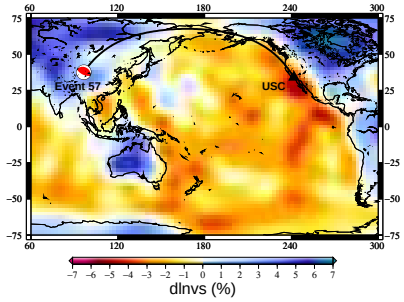

Figure 2.4: (a) Example multi-pathing seismograms. The seismograms are transverse-component synthetic seismograms at station USC for a ray path shown in (b). In this example, surface waves in the 3-D velocity model (red trace) show an additional late arrival compared to the seismogram in 1-D velocity model (black trace). (b) Reference ray path along which multi-pathing arrivals are observed.

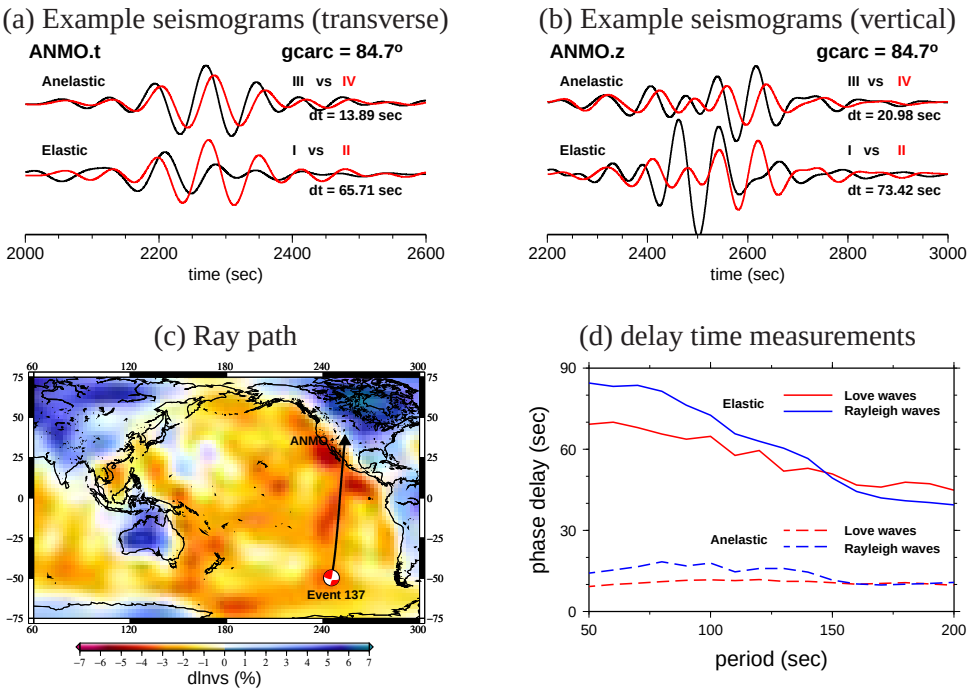

Figure 2.5: Example transverse (a) and vertical (b) synthetic seismograms at station ANMO, band-pass filtered between 6.7 mHz and 20 mHz. Top seismogram pairs show effects due to anelastic perturbations, black seismograms are generated using model (III) – 3-D velocity and 1-D Q, red seismograms are generated using model (IV) – 3-D velocity and 3-D Q. Bottom seismogram pairs show differences due to elastic perturbations: black traces are generated using model (I) – 1-D velocity and 1-D Q; red traces are generated using model (II) – 3-D velocity and 1-D Q. Delay times measured at 100 seconds using multi-taper technique are indicated below the traces. The ray path of the seismograms is shown in (c) and measured elastic and anelastic delay times as a function of period are plotted in (d).

Examples of synthetic seismograms from numerical simulations are shown in Fig. 2.5. The transverse and vertical component seismograms at station ANMO have been band-pass filtered between 6.7 mHz and 20 mHz. The top two traces in (a) and (b) show differences in seismograms caused by 3-D Q structure, and the bottom two traces show differences of surface waves caused by 3-D velocity structure. Frequency-dependent delay-time measurements are plotted in Fig. 2.5(d) for this example path. At a period of 100 seconds, the 3-D velocity variations delay the arrival time of the fundamental-mode Love wave by $\sim$65 seconds and Rayleigh wave by $\sim$73 seconds for this particular path; delay times caused by 3-D anelastic dispersion are $\sim$14 seconds for the Love wave and $\sim$21 seconds for the Rayleigh wave. The 3-D anelastic dispersion effects (difference between 3-D Q and

1-D Q models) on phase delays are about 1/4 of the phase delays caused by 3-D velocity structure (differences between 3-D velocity and 1-D velocity models). More detailed analysis on the anelastic dispersion effects will be be discussed in detail in section 2.4. It is also noteworthy that amplitudes variations in this example show that the effects of 3-D velocity structure on surface-wave amplitudes (focusing/defocusing) are more prominent than the effects of 3-D Q structure, this is consistent with estimates made based upon 3-D sensitivity kernels (Zhou, 2009) and amplitude measurements will be discussed in chapter 3.

2.4 3-D anelastic effects on surface waves and frequency dependence

In Fig. 2.6 we compare Love-wave phase delays caused by 3-D velocity structure with those caused by 3-D Q structure. Each dot in the scatterplot represents two phase delay measurements made for the same source-receiver pair; the horizontal axis is the elastic delay $t_{3-\mathrm{D\,V}} - t_{1-\mathrm{D\,V}}$ and the vertical axis is the anelastic delay $t_{3-\mathrm{D\,Q}} - t_{1-\mathrm{D\,Q}}$. Measurement errors estimated using the multi-taper technique are indicated by black crosses. There are approximately 6,000 measurements in each scatterplot at periods of 60 seconds, 100 seconds and 200 seconds. As expected, the elastic delays and anelastic delays are highly correlated as the velocity and Q structures are correlated.

The anelastic effects on surface-wave phase delays are frequency dependent. This is due to local S-wave anelastic dispersion, frequency-dependent depth sensitivity of surface waves as well as the 3-D distribution of Q anomalies. Generally speaking, anelastic delays become more significant in long-period surface waves than in short-period surface waves. For Love waves at 60 seconds, the ratio between anelastic delays and elastic delays is roughly 0.17. For 100-second and 200-second Love waves, the ratio of anelastic delays to elastic delays increases to 0.22 and 0.27, respectively.

The depth sensitivity kernels of fundamental-mode surface waves calculated for model PREM at corresponding periods are plotted next to each scatterplot for reference. The root-mean-square (rms) values of the 3-D anelasticity model and 3-D velocity model as function of depth are also plotted. The depth sensitivity functions show that short-period Love waves are sensitive to shallow structures where Q values are relatively high and variations of $1/Q$ are relatively weak. Therefore weaker anelastic effects on surface waves are expected. Long-period Love waves are more sensitive to deeper structures in our 3-D Q model, and Q variations are large in the low Q zone at depth of 80-200 km. Therefore the contribution of anelastic dispersion to long-period surface-wave phase delays becomes more prominent.

Comparisons between anelastic delays and elastic delays for Rayleigh waves are shown in Fig. 2.7. The ratios of anelastic delays to elastic delays also show strong frequency dependence. For 60-second Rayleigh waves, this ratio is approximately 0.21, and for 100-second and 200-second Rayleigh waves, the ratio increases to roughly 0.24 and 0.27. This frequency dependence can be explained by the depth sensitivity of Rayleigh waves and the rms of the models. In the uppermost 100 km, the ratio between the rms of the 3-D velocity model and the rms of the 3-D Q model is large. Therefore, for short-period Rayleigh waves, which are more sensitive to shallow structure, anelastic dispersions are relatively weak compared with elastic delays. At depths below 100 km, the ratio between the rms of the 3-D velocity model and the rms of the 3-D Q model becomes smaller. Therefore, Rayleigh waves at 100 and 200 seconds, which are more sensitive to structures in this depth range, show stronger anelastic dispersion than short-period waves. In general, Rayleigh waves are less sensitive to shallow structures than Love waves, and they are more sensitive to structures in depth range of 80 – 300 km (the low Q zone in our model), therefore, 3-D anelastic dispersion effects are more prominent in Rayleigh waves than Love waves.

Based upon the comparisons, we can estimate the fractional contribution of anelastic dispersion to the total surface-wave phase delays. At 100 seconds, the slope of scatterplot is roughly 0.22 for Love

waves and 0.24 for Rayleigh waves, this indicates that assuming a thermal origin of mantle anomalies, phase delays caused by 3-D Q structure accounts for roughly 17-19% of the total observed delay times. At 200 seconds, anelastic dispersion effects account for approximately 21% of the total delay times for both Love waves and Rayleigh waves. At 60 seconds, the percentage decreases to around 15-17%. However, it is important to note that short-period surface waves, especially Love waves, are sensitive to shallow lithosphere structure, and anelastic dispersion of short-period surface waves depends upon Q structures at shallow depths. Because of the exponential temperature dependence, Q values in our reference models are much larger than PREM in the uppermost 50 km. Recent studies (e.g., Durek & Ekström, 1996) suggested a Q value of 300 in the lithosphere. A decrease in background Q will result in an increase in the sensitivity of surface-wave phase delays to fractional perturbations in $1/Q$ (Zhou, 2009). To estimate the effects of a low-Q lithosphere, we generate synthetic seismograms in our reference 1-D Q model with/without the top 80 km layer replaced by a constant Q of 300 and compare surface-wave travel times. At an epicentral distance of 150 degree, 50-second Love waves are delayed by 5 seconds, 100- and 200-second Love waves are delayed by 3 seconds, Rayleigh waves at all periods are delayed by less than 2 seconds. Considering uncertainties in our measurements, the effects of a low Q value in the top 80 km are negligible in long-period Love waves and Rayleigh waves. For short-period Love waves, lower Q values in the top 80 km can lead to slightly stronger 3-D anelastic dispersion than seen in Fig. 2.6.

It is important to point out that while anelastic delays and elastic delays are highly correlated, their relation is not linear. Moreover, due to 3-D wave propagation effects, elastic advances in surface-wave travel times are not necessarily always associated with anelastic advances, sometimes they are accompanied with no advance or even weak anelastic delays. For waves propagating through dominantly fast anomalies, large elastic travel time advances (negative delays) are observed, the anelastic advances do not increase linearly with elastic advances but show a weak flattening pattern in the scatterplot. The weakening of anelastic effects in seismically fast ("cold") regions becomes more apparent for purely

continental paths, and the path dependence will be discussed in more detail in section 2.6.

It is worth noting that (1) the fact 15-20% of observed phase delays can be attributed to 3-D Q structure does not necessarily indicate current velocity tomographic models (e.g. S20RTS) have been overestimated. This is because inaccuracy in tomographic theory will introduce internal inconsistency in the inverse system, which often requires greater damping to be applied in the inversion; (2) the relative contribution of 3-D elastic and 3-D anelastic effects in surface-wave phase delays does not depend on the rms of the "elastic" wavespeed model (S20RTS) used in this chapter; and (3) we have assumed a thermal origin of mantle wavespeed and Q anomalies, other effects such as water content and partial melting can also be important but they have not been well constrained in mineral physics and are beyond the scope of this study.

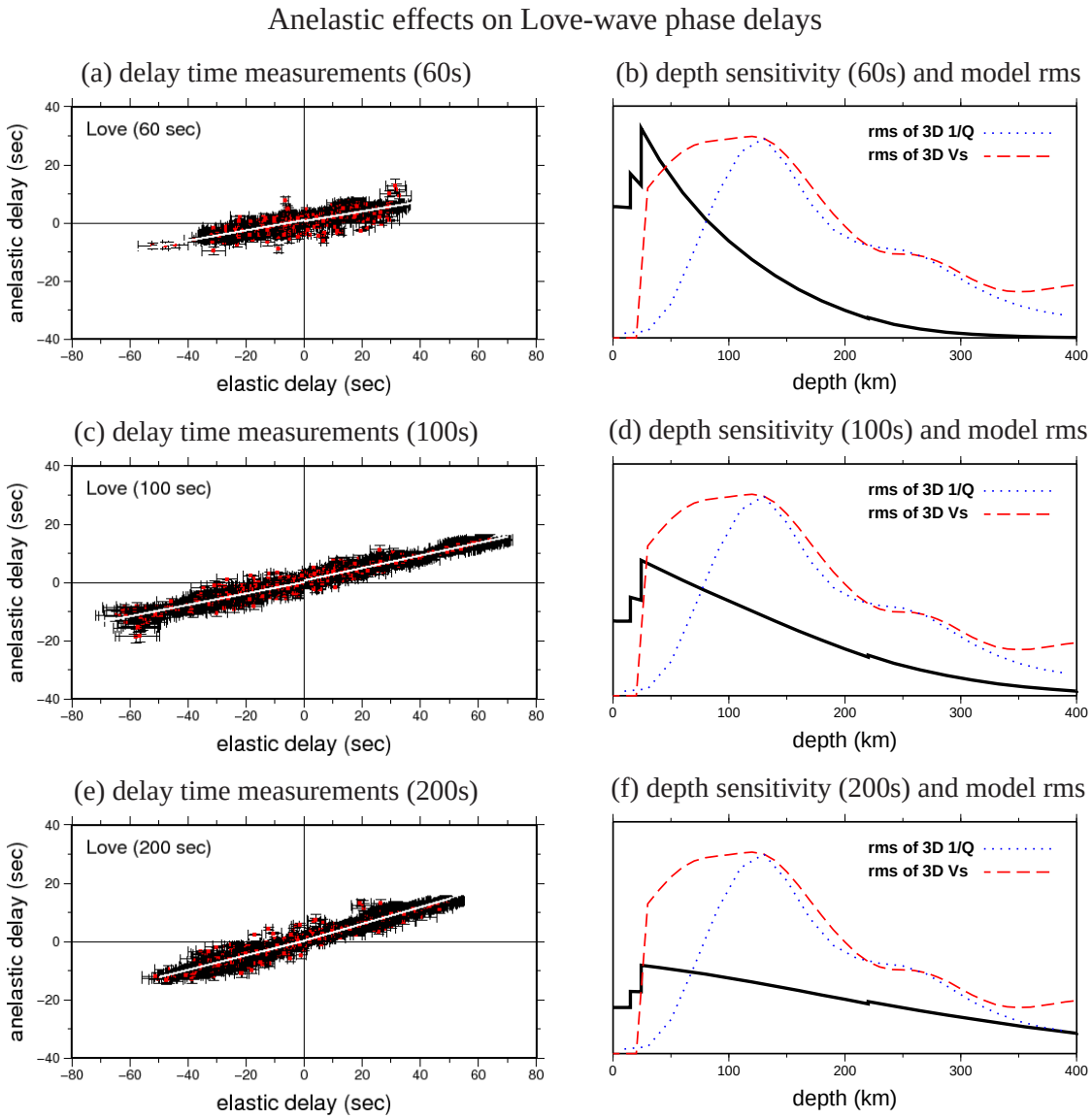

Figure 2.6: Comparison of elastic delays and anelastic delays on Love waves at periods of (a) 60 seconds (c) 100 seconds and (e) 200 seconds. In the scatterplots, the horizontal coordinate of the scatterplots is elastic phase delay ($t_{3-\mathrm{D\,V}} - t_{1-\mathrm{D\,V}}$) and the vertical coordinate is anelastic phase delay ($t_{3-\mathrm{D\,Q}} - t_{1-\mathrm{D\,Q}}$). Errors estimated using the multi-taper technique are indicated by black crosses. Least-square-fitted slope of each scatterplot (white line) shows the ratio between anelastic and elastic effects. These ratios are 0.17 at 60 seconds, 0.22 at 100 seconds and 0.27 at 200 seconds, showing a strong frequency dependence of anelastic effects. Radial sensitivity ($\partial c/\partial\beta$) of fundamental-mode Love waves at corresponding period and root-mean-square (rms) of 3-D Q ($\delta \ln(1/Q)$) and 3-D velocity ($\delta \ln V_S$) models are plotted in (b), (d) and (f) as functions of depth. Sensitivity of long-period Love waves show that they are more sensitive to the low Q zone (80-300 km) than short-period Love waves, therefore stronger anelastic dispersion effects are expected at longer periods.

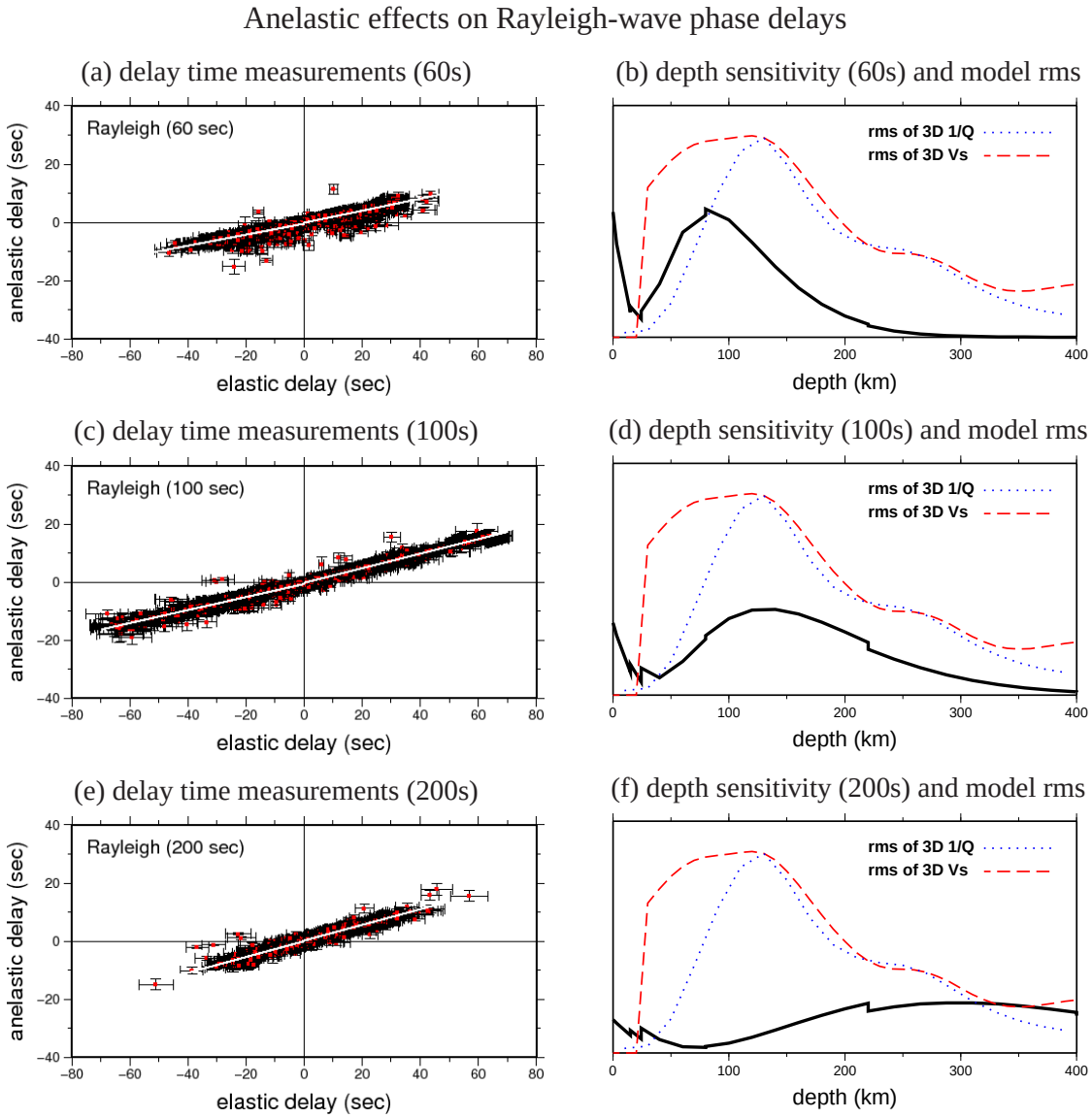

Figure 2.7: The same as Fig. 2.6 but for Rayleigh waves. Strong frequency dependence of anelastic effects is also observed in Rayleigh-wave phase delays. The fitted ratios of anelastic delays to elastic delays are 0.21 at 60 seconds, 0.24 at 100 seconds and 0.27 at 200 seconds. 3-D anelastic effects on Rayleigh waves are systematically more significant than Love waves because Rayleigh waves are more sensitive to structures in the low Q zone (80-300 km) in our model.

2.5 The effects of mineralogical parameters

In this section we examine the dependence of 3-D anelastic effects on mineralogical parameters that control both the 1-D reference Q model and the conversion from 3-D velocity model to 3-D Q model. We experiment with additional two sets of rheology parameters to investigate the effects of rheology parameters on the resulting Q models. The rheology parameters are listed in Table (2.2) and the corresponding 1-D Q models are labeled as $\mathbf{Q1DM_L}$, $\mathbf{Q1DM_M}$ and $\mathbf{Q1DM_H}$, where model $\mathbf{Q1DM_M}$ is the 1-D Q model we used in section 2.3 and 2.4 and it is comparable to PREM (Fig. 2.1 and 2.8). In generating model $\mathbf{Q1DM_L}$ we used a slightly smaller activation energy $E^* = 420$ KJ/mol and a relatively higher activation volume $V^* = 19$ cm^3/mol; and for model $\mathbf{Q1DM_H}$ we used a larger activation energy $E^* = 520$ KJ/mol and a smaller activation volume $V^* = 15$ cm^3/mol. We adjust the mineralogical parameters accordingly such that the overall Q values in the mantle are smaller than PREM in model $\mathbf{Q1DM_L}$ and larger than PREM in model $\mathbf{Q1DM_H}$. (Fig. 2.8). The corresponding 3-D Q models, $\mathbf{Q3DM_L}$ and $\mathbf{Q3DM_H}$, are calculated from 3-D velocity model S20RTS for the additional two sets of mineralogical parameters ($\mathbf{M_L}$ and $\mathbf{M_H}$) using the same algorithm that has been discussed in section 2.3.2. Maps of the 3-D Q models at a depth of 100 km are plotted in Fig. 2.9. We ran wave propagation experiments in the two additional sets of global Q models, and make phase delay measurements following the same procedure as described in section 2.3.3.

Table 2.2: Rheology parameters for different anelasticity (Q) models

Parameter set	E^*(KJ/mol)	V^* (cm^3/mol)	A
$\mathbf{M_L}$	420	19	1.394
$\mathbf{M_M}$	470	17	1.394
$\mathbf{M_H}$	520	15	1.394

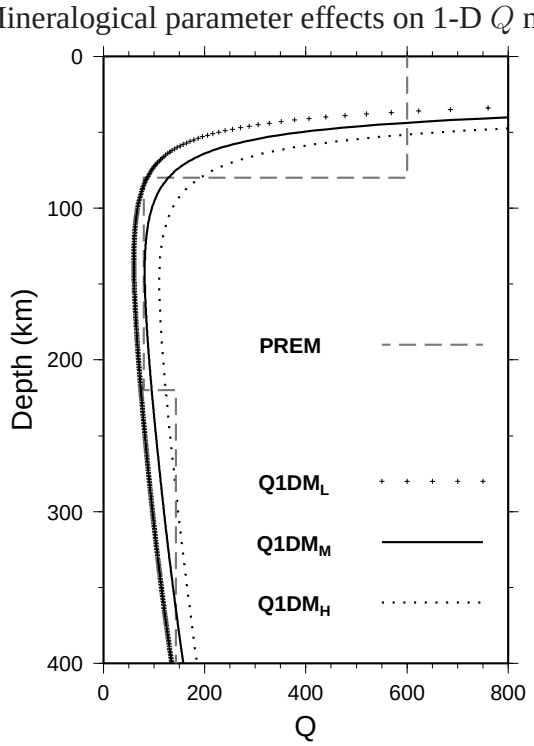

Figure 2.8: Reference Q models constructed using three different mineralogical parameter sets (see Table. 2.2). Q values in $\mathbf{Q1DM_M}$ are moderate and comparable to PREM at depths between 80 – 220 km, Q values are higher than PREM in model $\mathbf{Q1DM_H}$ and lower than PREM in model $\mathbf{Q1DM_L}$. PREM Q model is plotted in gray dashed line for reference.

Our measurements show that the effects of 3-D anelastic dispersion are dependent upon mineralogical parameters used in the experiment. Scatterplots of 100-second Rayleigh-wave phase delays are plotted in Fig. 2.9. The ratio of anelastic phase delays to elastic phase delays depends upon mineralogical parameters: measurements made for 3-D Q model $\mathbf{Q3DM_L}$ show that the slope of the scatterplot is roughly 0.28, and the ratio decreases to $\sim$0.24 in Q model $\mathbf{Q3DM_M}$ and it deceases further to $\sim$0.21 for model $\mathbf{Q3DM_H}$.

Least square fitted ratios of anelastic to elastic delay times for Love waves and Rayleigh waves for the three sets of global Q models are shown in Fig. 2.9. The elastic delays are identical in the three groups, while anelastic delays vary with mineralogical parameters applied in generating the 1-D and 3-D Q models. The gray bars are ratios at periods ranging from 60 seconds to 200 seconds. The fre-

quency dependence of anelastic dispersion shows a similar pattern in the three experiments: anelastic dispersion is more significant at longer periods, and the frequency dependence is most apparent in the period range between 60–150 seconds and becomes weaker at longer periods (150 – 200 seconds), especially for Rayleigh waves.

In the case of using the mineralogical parameter set $\mathbf{M_L}$, the anelastic dispersion effects on surface-wave phase delays are the largest at all periods for both Love waves and Rayleigh waves in spite of the smallest fractional perturbations in $1/Q$ among the three 3-D Q models (Fig. 2.9). It is worth emphasizing that (1) both the reference Q models and perturbations in Q are calculated from mantle temperature using three different sets of mineralogical parameters; (2) anelastic delay times are introduced by perturbations in Q, while temperature partial derivatives are dependent also upon the reference Q values, and overall the 3-D anelastic dispersion effects become stronger when the mineralogical parameters used are associated with lower reference Q values, and (3) we shall keep in mind that uncertainties in mineralogical parameters will lead to uncertainties in 3-D anelastic dispersion effects as illustrated in Fig. 2.9.

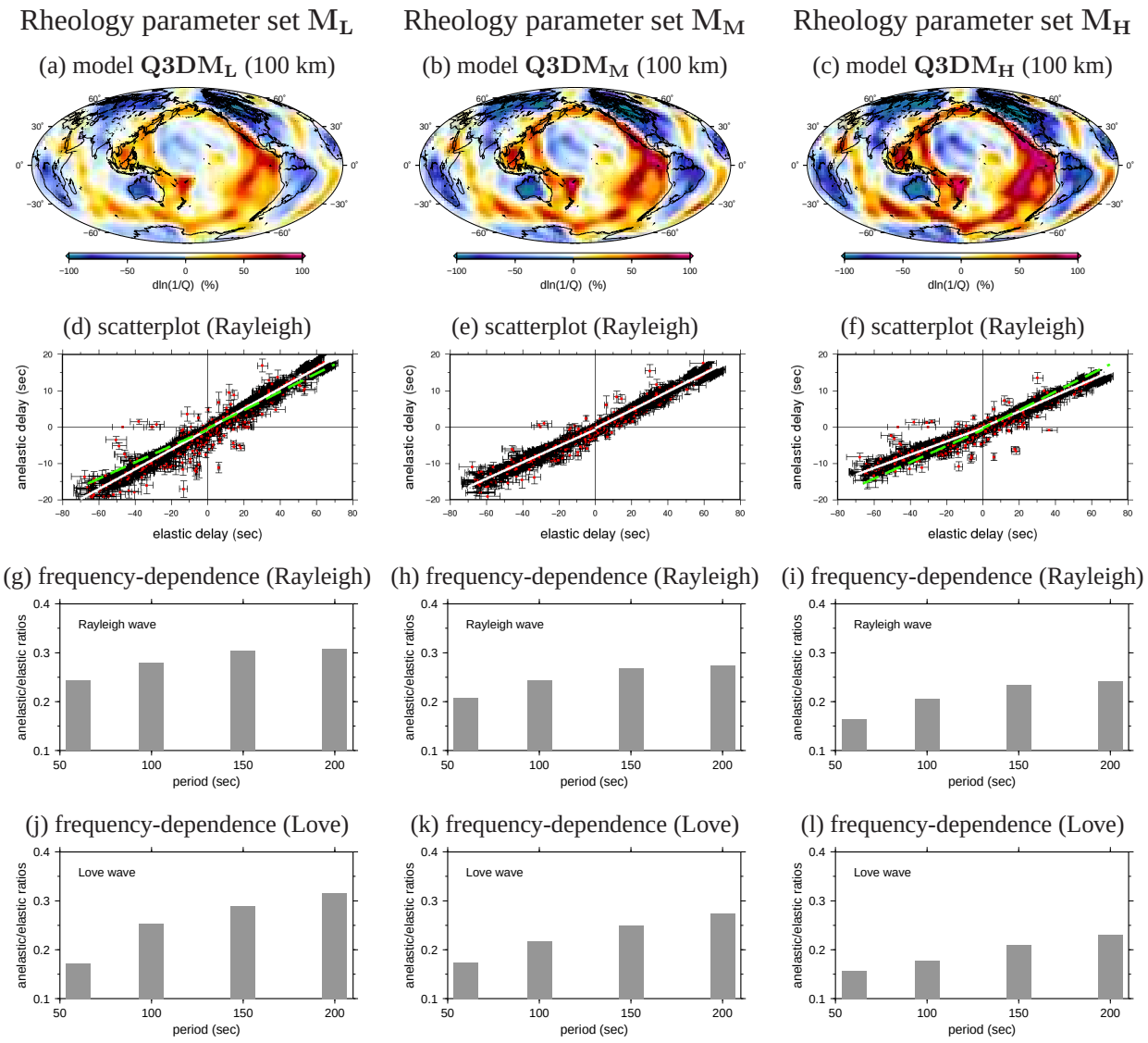

Figure 2.9: Delay-time measurements for three sets of global Q models generated using mineralogical parameters $\mathbf{M_L}$, $\mathbf{M_M}$ and $\mathbf{M_H}$; (a), (b) and (c) are maps of fractional perturbations in $1/Q$ ($\delta \ln Q^{-1}$) at a depth of 100 km. and corresponding reference (1-D) Q models are plotted in Fig. 2.8; (d), (e) and (f) are scatterplots of elastic delays versus anelastic delays for 100-second Rayleigh waves, the ratio of anelastic delay to elastic delay decreases from $\sim$0.28 (parameter set $\mathbf{M_L}$) to $\sim$0.21 (parameter set $\mathbf{M_H}$). The best fitting line in (e) is also plotted as green dashed lines in (d) and (f) for comparison. (g), (h), and (i) are the ratios (gray bars) of anelastic delay to elastic delay of Rayleigh waves at periods of 60s, 100s, 150s and 200s. These ratios come from least-square fitting of measurements. The 3-D anelastic effects are frequency-dependent and the frequency dependence is most apparent in the period range between 60 – 150 seconds. Note fractional perturbations in $1/Q$ are the smallest in model $\mathbf{Q3DM_L}$, while the associated anelastic delay times are largest due to the associated low Q values in the reference model $\mathbf{Q1DM_L}$ (Fig. 2.8).

2.6 Path dependence of 3-D anelastic effects

Our measurements show that 3-D anelastic effects on surface-wave phase delays are path dependent. We select measurements with their great-circle ray paths mainly traveling through oceanic regions as well as those with their great-circle paths mainly in continental regions. Phase-delay measurements for 100-second Love waves and Rayleigh waves and associated ray paths are plotted in Fig. 2.10 and 2.11 for comparison of oceanic paths and continental paths.

In the upper mantle, there is strong correlation between velocity model S20RTS and tectonic features. The oceanic regions are underlain by slower ("hotter") mantle material while stable continents are associated with faster ("colder") lithosphere and mantle. As expected, the scatterplot of elastic-anelastic phase delays for oceanic paths is dominated by positive travel time delays and measurements of continental paths are dominated by negative travel time delays. In Fig. 2.10, the ratio of anelastic delays to elastic phase delays of 100 second Love waves is close to 0.2 for oceanic paths. For continental paths, there is apparent "flattening" on the scatterplot: waves traveling through "colder" regions experience larger phase advances but not as significant increase in 3-D anelastic dispersion. The "flattening" is unlikely due to Love-wave higher-mode contamination because (1) we have excluded records contaminated by higher modes from our measurements; (2) higher modes would affect both the elastic and anelastic measurements and therefore will not result in "flattening" in anelastic measurements and (3) the "flattening" is expected based upon the non-linear relation between "elastic" and "anelastic" delays which will be discussed in section 2.7.

We calculate global phase-velocity maps of 100-second Love waves in the four models listed in Table 2.1. The differences in phase velocities between model (I) and (II) are due to 3-D elastic structure ($c_{3-\mathrm{D\,V}} - c_{1-\mathrm{D\,V}}$), and they are plotted in Fig. 2.10 (e). The fractional perturbations $\delta c/c$ with respect to $c_{1-\mathrm{D\,V}}$ are in the range of -4.1% — 4.7%. The differences in phase velocities between model (III) and (IV) are due to 3-D anelastic structure ($c_{3-\mathrm{D\,Q}} - c_{1-\mathrm{D\,Q}}$) and the perturbations with

respect to $c_{1-\mathrm{D\,Q}}$ are plotted in Fig. 2.10 (f), and the perturbations are in the range of -0.89% — 0.86%. The amplitude of the fractional perturbations in local phase velocities due to 3-D velocity structure is about 3-4 times stronger than that due to 3-D anelastic structure (note the different color scales in Fig. 2.10). The ratio between local $\delta c/c$ caused by 3-D velocity structure and those caused by 3-D Q structure are location dependent, and, they are generally smaller in continental areas than in oceanic areas.

In Fig. 2.11, we compare measurements made for oceanic paths and continental paths for 100-second Rayleigh waves. Rayleigh-wave phase-delay measurements for oceanic paths are dominated by travel time delays (slow anomalies), and the ratio of anelastic delays to elastic phase delays is close to 0.25, and it is larger than the ratio for Love waves at the same period. For continental paths, the flattening of the scatterplot is not as apparent as 100-second Love waves, and the ratio is close to 0.24. Overall, 3-D anelastic dispersion effects on phase delays are slightly stronger in oceanic paths than in continental paths. We calculate maps of 100-second Rayleigh-wave phase velocity perturbations due to 3-D Q structure ($c_{3-\mathrm{D\,Q}} - c_{1-\mathrm{D\,Q}}$), and the fractional perturbations are in the range of -0.79% — 0.85% while the perturbations due to 3-D elastic structure ($c_{3-\mathrm{D\,V}} - c_{1-\mathrm{D\,V}}$) vary from -3.5% to 3.9%, relatively weaker than those for 100-second Love waves. As a result, 3-D Q structures have more significant effects on Rayleigh waves than on Love waves – this is consistent with the slope variations in the measurement scatterplots.

We conclude that (1) the effects of 3-D anelasticity on phase delays are more significant in oceanic paths than in continental paths, i.e., the effects of 3-D anelastic dispersion on phase advances are less significant than that on phase delays. This is mainly due to the non-linear relation between "elastic" and "anelastic" velocity perturbations in the case of a common thermal origin, and (2) the path dependence is more apparent for Love waves than for Rayleigh waves. In section 2.7, we verify the non-linear relation for local S waves using a simple analytical approach.

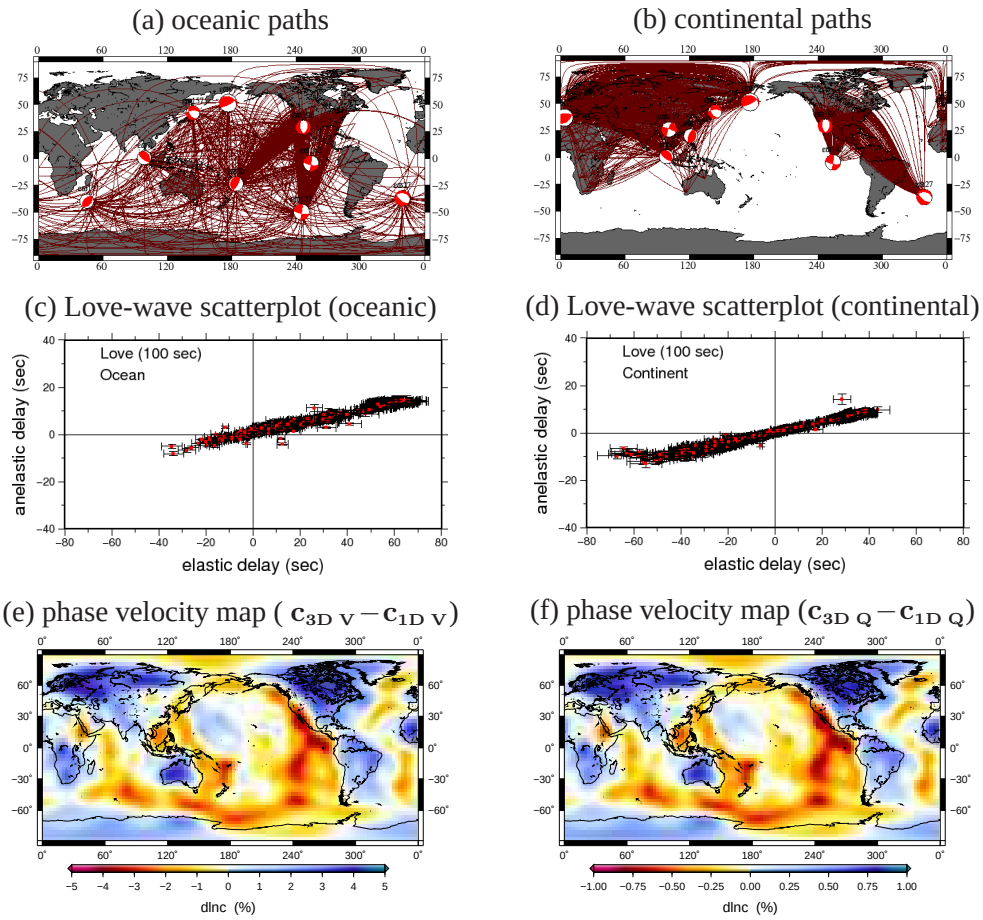

Figure 2.10: Path dependence of anelastic effects on Love-wave phase delays. Top: (a) and (b) are map views of oceanic paths (1502 paths) and continental paths (2665 paths), respectively. Love-wave delay-time scatterplots for the two groups of paths are plotted in (c) and (d), respectively. The continental scatterplot shows some "flattening" indicating that anelastic effects are weaker for continental paths than for oceanic paths. (e) and (f) are phase velocity maps of 100-second Love waves corresponding to 3-D velocity and 3-D Q structure, respectively. Fractional perturbations in phase velocity ($\delta \ln c$) varies from -4.1% to 4.7% in (e) and from -0.89% to 0.86% in (f). Note different color scales have been used in (e) and (f).

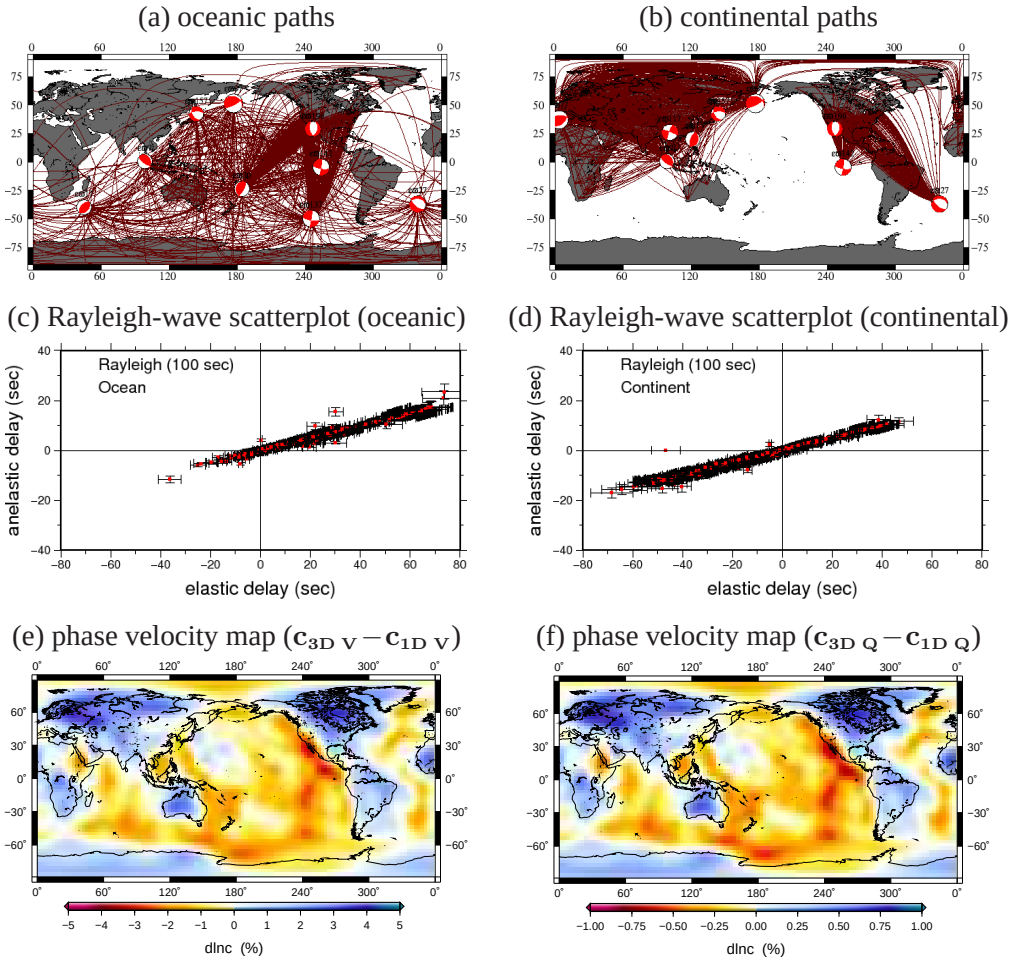

Figure 2.11: The same as Fig. 2.10 but for Rayleigh waves, there are 1,499 oceanic paths and 2,578 continental paths. The slope of the scatterplots is 0.25 for oceanic paths and is 0.24 for continental paths. (e) and (f) are phase-velocity maps of 100-second Rayleigh waves corresponding to 3-D velocity and 3-D Q structure, respectively. Fractional variations in phase velocity range from -3.5% to 3.9% in (e) and -0.79% to 0.82% in (f). Note different color scales have been used in (e) and (f).

2.7 Analytical verifications

Surface waves are mainly constructive interactions of multiple reflected S waves. To the first order for small perturbations in Q in eq. (2.3), local perturbations in S-wave velocity due to local perturbations in $Q \rightarrow Q + \delta Q$ can be written as

$$\left(\frac{\delta V_{\rm S}}{V_{\rm S}}\right)_{\rm 3-D\,Q} = -\frac{1}{Q\pi}\ln\left(\frac{\omega}{\omega_0}\right)\frac{\delta Q}{Q}, \tag{2.10}$$

where $Q = Q_\mu$ is the local quality factor for shear modulus. Assuming local Q perturbations are due to temperature perturbations, $\delta Q/Q$ can be related to perturbations in temperature δT in eq. (2.9), yielding

$$\left(\frac{\delta V_{\rm S}}{V_{\rm S}}\right)_{\rm 3-D\,Q} = \frac{\alpha}{Q\pi}\ln\left(\frac{\omega}{\omega_0}\right)\frac{E^* + PV^*}{RT^2}\delta T. \tag{2.11}$$

The temperature partial derivative in eq. (2.8) can be used to find the associated velocity perturbations at the reference Q value,

$$\left(\frac{\delta V_{\rm S}}{V_{\rm S}}\right)_{\rm 3-D\,Q} = \frac{\alpha}{Q\pi}\ln\left(\frac{\omega}{\omega_0}\right)\frac{E^* + PV^*}{RT^2}\left(\frac{\partial \ln V_{\rm S}}{\partial T}\right)^{-1}\left(\frac{\delta V_{\rm S}}{V_{\rm S}}\right)_{\rm 3-D\,V}. \tag{2.12}$$

To the first order assuming thermal anomalies, fractional perturbations in anelastic dispersion introduced by local variations in anelasticity $(\delta V_{\rm S}/V_{\rm S})_{\rm 3-D\,Q}$ are related to fractional perturbations in S-wave velocity $(\delta V_{\rm S}/V_{\rm S})_{\rm 3-D\,V}$ at the reference Q. This relation is not linear but dependent upon the background Q value as well as temperature T. In Fig. 2.12, we calculate local 3-D anelastic dispersions $(\delta V_{\rm S}/V_{\rm S})_{\rm 3-D\,Q}$ associated with velocity variations $(\delta V_{\rm S}/V_{\rm S})_{\rm 3-D\,V}$ in the range of -3% – 3% for reference Q and temperature values at depths of 100 km, 150 km, 200 km, 300 km and 400 km. We use an iterative approach and update temperature, Q and the partial derivative $\partial \ln V_{\rm S}/\partial T$ in the calculations of $(\delta V_{\rm S}/V_{\rm S})_{\rm 3-D\,Q}$ until eq. (2.12) converges. The mineralogical parameters as well as the reference thermal structure have been described in sect. 2.3.1.

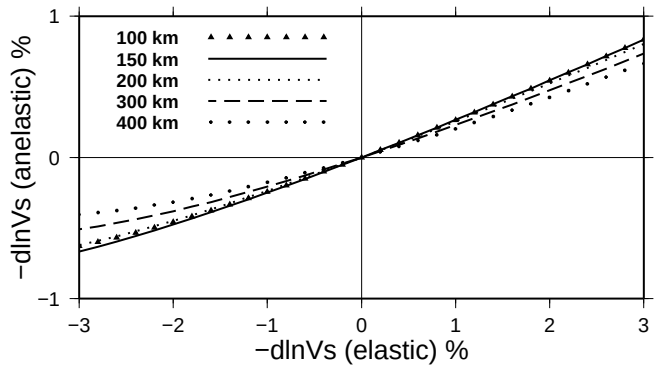

Figure 2.12: Predicted elastic velocity perturbations versus anelastic velocity perturbations for 100-second shear waves calculated using equation (2.12) at different depths using an iterative approach. The relation between elastic and anelastic velocity perturbations is not linear and the ratio between anelastic and elastic velocity perturbations becomes larger for "hot" anomalies. For example, at a depth of 100 km, 2% "elastic" velocity reduction is associated with 0.54% "anelastic" velocity reduction, while 2% "elastic" velocity increase is associated with 0.46% "anelastic" velocity increase. The ratio between anelastic and elastic velocity perturbations also depends upon the background Q value, for example, the ratio increases from 0.22 at 400 km (reference $Q = 157.6$) to 0.28 at 150 km (reference $Q = 81.7$). Note that these calculations are for local perturbations in velocity and Q, and can not be directly compared with phase-delay measurements as surface-wave delays are integrated effects of local perturbations over depth as well as over the ray path.

The relation between local perturbations in $(\delta V_{\rm S}/V_{\rm S})_{3-{\rm D\,Q}}$ and $(\delta V_{\rm S}/V_{\rm S})_{3-{\rm D\,V}}$ in Fig. 2.12 is generally consistent with our surface-wave phase delay measurements — the ratio between $(\delta V_{\rm S}/V_{\rm S})_{3-{\rm D\,Q}}$ and $(\delta V_{\rm S}/V_{\rm S})_{3-{\rm D\,V}}$ is roughly between 0.13 and 0.28. The curves flatten out for large negative perturbations in $-(\delta V_{\rm S}/V_{\rm S})_{3-{\rm D\,V}}$, indicating that the effects of 3-D anelastic dispersion in fast (cold) regions are not as significant as in slow (hot) regions for the same amount of absolute perturbations in local $(\delta V_{\rm S}/V_{\rm S})_{3-{\rm D\,V}}$. For example, when temperature increases, 1% "elastic" S-wave velocity reduction at a depth of 100 km is associated with 0.26% "anelastic" velocity reduction, while 2% "elastic" velocity reduction is associated with 0.54% "anelastic" velocity reduction. In the case of temperature decrease, 1% "elastic" velocity increase is associated with 0.24% "anelastic" velocity increase, and 2% "elastic" velocity increase is associated with 0.46% "anelastic" velocity increase. This is consistent with the "flattening" of anelastic phase advances observed for the continental paths as described in sect. 2.6.

It is important to point out this analysis is based purely upon local perturbations in Q and velocity.

The curves in Fig. 2.12 can not be directly compared with phase delay measurements as surface-wave phase delays are integrated effects of local perturbations over depth as well as over the ray path. For example, large surface-wave phase delays in 3-D velocity models do not necessary correspond to large local velocity perturbations but may be a result of surface waves propagating though large provinces of weak anomalies.

2.8 Conclusion

We investigate the effects of lateral variations in anelasticity (Q) on long-period surface-wave phase delays by simulating wave propagation in earth models with 3-D wavespeed structures and 3-D Q structures using the Spectral Element Method (Komatitsch & Tromp, 1999, 2002). We compare phase delays caused by 3-D Q structure with phase delays caused by 3-D wavespeed structure and conclude that 3-D Q structures in the mantle have significant effects on long-period surface-wave phase delays. At a period of 100 seconds, the ratio between phase delays caused by 3-D Q structure and those caused by 3-D velocity structure is roughly between 0.21-0.24, indicating that roughly 15-20% of observed phase delays are due to 3-D Q structure. These effects have so far been ignored in present-day tomographic studies and may have led to biased tomographic structures. The coupling between elastic and anelastic effects in surface-wave travel times indicates that a joint inversion of 3-D velocity and 3-D Q structure using both travel times and amplitudes is necessary. The resulting self-consistent 3-D velocity and 3-D Q models will be very helpful in mapping lateral thermal and compositional heterogeneities in the upper mantle.

Our numerical experiments show that 3-D anelastic dispersion effects on surface-wave phase delays depend upon the frequency of the waves due to local S-wave anelastic dispersion, frequency-dependent depth sensitivity of surface waves as well as the depth distribution of Q anomalies. The 3-D anelastic effects generally increase with increasing wave period and the frequency dependence

is most apparent in the period range between 60 – 150 seconds in our numerical experiments as Q variations are the strongest in the asthenosphere.

In a thermal model, the significance of the 3-D anelastic dispersion effects depend upon mineralogy parameters, i.e., activation energy and activation volume. The 3-D Q model used in this chapter is constructed using the 3-D wavespeed model S20RTS assuming that both velocity and Q perturbations are due to temperature variations. Delay times introduced by the 3-D velocity structure and those introduced by the corresponding 3-D Q structure are therefore correlated, but the correlation is not linear: the ratio between anelastic and elastic delays (or advances) becomes larger for "hotter" anomalies than for "colder" anomalies.

Bibliography

Anderson D. L. & Minster, J. B., 1979. The frequency dependence of Q in the Earth and implications for mantle rheology and Chandler wobble, *Geophys. J. Int.,* **58**, 431-440.

Béjina, F., Jaoul, O. & Liebermann, R. C., 2003. Diffusion in minerals at high pressure: a review, *Phys. Earth planet. Inter.,* **139**, 3-20.

Billien, M., Lèvêque, J.-J. & Trampert, J., 2000. Global maps of Rayleigh wave attenuation for periods between 40 and 150 seconds, *Geophys. Res. Lett.,* **27**, 3619–3622.

Dalton, C. & Ekström, G., 2006. Global models of surface wave attenuation, *J. geophys. Res.*, **111**, B05317, doi:10.1029/2005JB003997.

Dalton, C., Ekström, G. & Dziewoński, A. M., 2008. The global attenuation structure of the upper mantle, *J. geophys. Res.,* **113**, B09303, doi:10.1029/2007JB005429.

Dahlen, F. A. & Tromp, J., 1998. *Theoretical Global Seismology*, Princeton University Press, Princeton, New Jersey.

Duffy, T. S., and Anderson, D. L., 1989. Seismic velocities in mantle minerals and the mineralogy of the upper mantle, *J. geophys. Res.,* **94**, 1895-1912.

Durek, J. J., and Ekström, G., 1996. A radial model of anelasticity constraint with long-period surface wave attenuation, *Bull. seism. Soc. Am.,* **86**, 144-158.

Dziewonski, A. M. & Anderson, D. L., 1981. Preliminary reference Earth Model, *Phys. Earth planet. Inter.,* **25**, 297-356.

Faul, U. H. & Jackson, I., 2005. The seismological signature of temperature and grain size variations in the upper mantle, *Earth planet. Sci. Lett.,* **234**, 119-134.

Grand, S. P., 1987. Tomographic inversion for shear velocity beneath the North American plate. *J. geophys. Res.,* **92**, 14,065-14,090.

Gung, Y. & Romanowicz, B., 2004. Q tomography of the upper mantle using three-component long-period waveforms, *Geophys. J. Int.,* **157**, 813-830.

Isaak, D. G., 1992. High-temperature elasticity of iron-bearing olivines, *J. geophys. Res.,* **97**, 1871-1885.

Jackson, I., 2000. Laboratory Measurements of Seismic Wave dispersion and Attenuation: Recent Progress., in *Earth's Deep Interior: Mineral Physics and Tomography from the Atomic to the Global Scale, AGU Geophysicsl Monograph Service*, vol.**117**, S. Karato *et al.* (eds), 265-289.

Jackson, D. D. & Anderson, D. L, 1970. Physical Mechanisms of Seismic-Wave Attenuation, *Rev. Geophys.,* **8**, issue 1, 1-63.

Jackson, I. & M. S. Paterson, 1993. A high-pressure, high-temperature apparatus for studies of seismic wave dispersion and attenuation, *Pure appl. Geophys.*,**141**, 445-466.

Jackson, I., Fitz Gerald, J. D., Faul, U. H. & Tan, B. H., 2002. Grain-size sensitivity seismic wave attenuation in polycrystalline olivine, *J. geophys. Res.*, **107**, B12,2360, doi:10.1029/2001JB001225.

Kanamori, H. & Anderson, D.L., 1977. Importance of physical dispersion in surface-wave and free-oscillation problems - Review: *Rev. Geophys. Space Phys.*, **15**, 105–112.

Karato, Shun-ichiro, 1993. Importance of anelastic in the interpretation of seismic tomography, *Geophys. Res. Lett.,* **20**, NO. 15, 1623-1626.

Karato, S. & Spetzler., H. A., 1990. Defect microdynamics in mineral and solid-state mechanisms of seismic wave attenuation and velocity dispersion in the mantle, *Rev. Geophys.,* **28**, 399-421.

Komatitsch, D. & Tromp, J., 1999. Introduction to the spectral-element method for 3-D seismic wave propagation, *Geophys. J. Int.,* **139**, 806-822.

Komatitsch, D. & Tromp, J., 2002. Spectral-element simulations of global seismic wave propagation—I. Validation, *Geophys. J. Int.,* **149**, 390-412.

Laske, G. & Master, G., 1996. Constraints on global phase velocity maps from long-period polarization data, *J. geophys. Res.*, **101**, NO. B7, 16,059-16,075.

Liu, H. P., Anderson, D. L. & Kanamori, H., 1976. Velocity dispersion due to anelasticity; implications for seismology and mantle composition, *Geophys. J. R. astr. Soc.*, **47**, 41-58.

Master, G., Johnson, S., Laske, G., & Bolton, H., 1996. A shear-velocity model of the mantle, *Phil. Trans. R. Soc. Lond.* A, **354**, 1385-1411.

Reid, F. J. L., Woodhouse, J. H. & Van Heijst, H. J., 2001. Upper mantle attenuation and velocity structure from measurements of differential S phases, *Geophys. J. Int.,* **145**, 615-630.

Ritsema, J. & Van Heijst, H. J., 2000. Seismic imaging of structural heterogeneity in Earth's mantle: Evidence for large-scale mantle flow, *Science Progress*, **83**, 243-259.

Romanowicz, B., 1995. A global tomographic model of shear attenuation in the upper mantle, *J. geophys. Res.*, **100**, 12,375-12,394.

Selby, N. D. & Woodhouse, J. H., 2000. Controls on Rayleigh wave amplitudes: Attenuation and focusing, *Geophys. J. Int.*, **142**, 933-940.

Selby, N. D. & Woodhouse, J. H., 2002. The Q structure of the upper mantle: Constraints from Rayleigh wave amplitudes, *J. geophys. Res.*, **107**, NO. B5, 2097, 10.1029/2001JB000257.

Shapiro, N. M. & Ritzwoller, M. H., 2004. Thermodynamic constraints on seismic inversions, *Geophys. J. Int.*, **157**, 1175-1188.

Shito, A., Karato, S. & Park, J., 2004. Frequency dependence of Q in Earth's upper mantle inferred from continuous spectra of body waves, *Geophys. Res. Lett.*, **31**, L12603, doi:10.1029/2004GL019582.

Slepian, D., 1978. Prolate spheroidal wave functions, Fourier analysis and uncertainty, V, The discrete case, *Bell Syst. Tech. J.*, **57**, 1371-1429.

Smith, M. L. & Dahlen, F. A., 1981. The period and Q of the Chandler wobble, *Geophys. J. Int.*, **64**, 223-281.

Su, W.-J., Woodward, R. L., and Dziewonski, A. M., 1994. Degree 12 model of shear velocity heterogeneity in the mantle. *J. geophys. Res.*, **99**, 6945-6980.

Warren, L. M. & Shearer, P. M., 2002. Mapping lateral variations in upper mantle attenuation by stacking P and PP spectra, *J. geophys. Res.*, **107**, NO. B12,2342, doi:10.1029/2001JB001195.

Wessel, P. & Smith, W. H. F., 1995. New Version of the Generic Mapping Tools Released, *EOS, Trans. Am. geophys. Un.*, **76**, 329.

Zhou, Y., Dahlen, F. A. & Nolet, G., 2004. Three-dimensional sensitivity kernels for surface wave observables, *Geophys. J. Int.*, **158**, 142-168.

Zhou, Y., Nolet, G., Dahlen, F. A. & Laske, G., 2006. Global upper-mantle structure from finite-frequency surface-wave tomography, *J. geophys. Res.*, **111** B04304, doi:10.1029/2005JB003677.

Zhou, Y. 2009. Surface-wave Sensitivity to 3-D Anelasticity, *Geophys. J. Int.*, **178**, 1403-1410.

Chapter 3

The effects of 3-D anelasticity (Q) structure on surface wave amplitudes

(An edited version of this chapter has published by RAS. Ruan, Y. and Zhou Y., The effects of 3-D anelasticity (Q) structure on surface wave amplitudes, 2012, *Geophys. J. Int.* **189**, 967-983.)

3.1 Introduction

The anelasticity of Earth material causes energy dissipation of seismic waves through internal friction and it is often measured by the quality factor Q. In the past decades, progress made in mineral physics has allowed laboratory studies of anelasticity of upper-mantle minerals under high temperature and high pressure. Recent mineralogical experiments show that variations in temperature, water content, and composition have very different effects on seismic wave speed and anelasticity in the Earth's mantle (e.g., Isaak, 1992; Jackson *et al.*, 1992; Karato & Spetzler, 1990; Jackson, 2000; Jackson *et*

al., 2002; Karato, 2003; Faul & Jackson, 2005). Therefore high resolution 3-D anelastic structures, together with 3-D elastic wave speed structures, can provide important constraints on the thermal and chemical state of the Earth's interior.

The propagation of seismic waves can be affected by perturbations in both elastic and anelastic properties, therefore, seismic travel times and amplitudes depend upon both wave speed and anelasticity. In mapping lateral heterogeneities in the Earth's interior, seismic travel times are usually used to invert for wave speed and amplitudes are used to map anelasticity. In extending the finite-frequency theory of surface-wave anelasticity (Dahlen & Zhou, 2006) to account for anelastic dispersion, Zhou (2009) pointed out the importance of accounting for coupling of elastic and anelastic effects in both travel times and amplitudes and suggested that joint tomographic inversions of 3-D wave speed and 3-D anelasticity structures are necessary for long-period surface waves.

It has been long recognized that anelasticity can affect travel times of seismic waves by anelastic dispersion (e.g., Liu *et al.*, 1976; Kanamori & Anderson, 1977). However, in 3-D wave speed tomography, seismic travel times are typically used without considering anelastic dispersion caused by 3-D anelastic structures. Ruan & Zhou (2010) showed that anelastic dispersion due to lateral perturbations in Q can cause 15-20% of the observed phase delays (travel times) in long-period surface waves. Ignoring anelastic dispersion in surface wave inversions may therefore lead to biased tomographic models. In resolving the 3-D Q structures of the mantle, the difficulty is that elastic focusing and defocusing caused by 3-D wave speed structures can strongly affect seismic amplitudes (e.g., Woodhouse & Wong, 1986; Romanowicz, 1998; Selby & Woodhouse, 2000; Dalton & Ekström, 2006a,b; Yang & Forsyth, 2006; Zhou, 2009). To date, the relative importance of elastic focusing and anelastic effects have not been well understood. In global anelastic tomography, different research groups take different approaches in handling elastic focusing/defocusing effects on amplitude (e.g., Durek *et al.*, 1993; Romanowicz, 1995; Bhattacharyya *et al.*, 1996; Selby & Woodhouse, 2002; Gung & Romanowicz, 2004; Dalton & Ekström, 2006b). The additional anelastic focusing/defocusing ef-

fects associated with anelastic dispersion have always been ignored. Although the resulting 3-D Q models are comparable in magnitude, large-scale features can differ greatly from each other (e.g., Gung & Romanowicz, 2004; Dalton *et al.*, 2008). More recently, there has been growing interest in modeling 3-D anelastic effects on seismic travel times and amplitudes through numerical wave propagation using currently available 3-D Q models (e.g., Savage *et al.*, 2010).

In this study, we quantify the effects of anelastic (Q) and elastic structures on surface wave amplitudes through numerical wave propagation simulation using a Spectral Element Method (Komatitsch & Tromp, 1999, 2002a,b). Investigations of surface wave phase delays based upon the same simulations have been documented in Ruan & Zhou (2010). The effects of anelasticity are Incorporated using an absorption band model with three standard linear solids (Savage *et al.*, 2010). The Earth's bulk quality factor (Q_κ) is orders of magnitude larger than the shear quality factor (Q_μ), and the sensitivity of Rayleigh waves to perturbations in Q_κ is very weak; for Love waves, the sensitivity is zero. In this chapter, we consider lateral heterogeneities only in Q_μ and ignore perturbations in Q_κ, and Q in this chapter refers to Q_μ hereinafter. We simulate wave propagation in Earth models with and without the presence of 3-D heterogeneities, and measure the amplitude perturbations in fundamental-mode surface waves caused by 3-D wave speed structures as well as those caused by 3-D Q structures. Our amplitude measurements based on the 3-D models show that the effects of 3-D wave speed structures and 3-D Q structures are comparable in short-period surface waves, and the effects of 3-D wave speed structures are dominant in long-period surface waves.

In ray theory, amplitude perturbations due to 3-D heterogeneities can be decomposed into three contributing effects: elastic focusing and defocusing, anelastic attenuation, and anelastic focusing and defocusing. We calculate ray-theoretical amplitude perturbations in 3-D wave speed and 3-D Q models. Ray-theoretical calculations confirm that elastic focusing dominates amplitude perturbations in 3-D models used in this study. In addition, we shows that the effects of anelastic attenuation are less significant compared to anelastic focusing/defocusing effects in long-period surface waves. Finally,

we discuss the uncertainties in mineralogical parameters used in the numerical experiments.

3.2 Wave propagation in 3-D Q and 3-D wave speed models

In this section, we will briefly review Earth models and numerical wave propagation experiments used to quantify the effects of 3-D anelasticity and 3-D wave speed structures on surface waves. The same models have been used to quantify the effects of anelastic dispersion on travel time in Ruan & Zhou (2010). We construct a 1-D reference Q model based upon a reference geotherm assuming half space cooling of an adiabatic mantle. Parameters are shown in Table 3.1. The reference geotherm profile is plotted in Fig. 3.1. The corresponding reference 1-D Q model then can be constructed from the reference geotherm assuming a thermally activated mechanism of anelasticity (Jackson & Anderson, 1970; Karato & Spetzler, 1990),

$$Q(\omega, T) = A \ \exp\left[\frac{\alpha\,(E^* + PV^*)}{R\,T}\right], \tag{3.1}$$

where the activation energy $E^* = 470$ KJmol^{-1} and activation volume $V^* = 17$ cm^{3}mol^{-1} are estimated from laboratory studies of upper mantle minerals (e.g., Olivine). The constant A is chosen so that the reference Q model is close to model PREM (Fig. 3.1).

Table 3.1: Geothermal parameters used for reference temperature profile.

Parameters	Values
Surface temperature T_s	0 °C
Mantle temperature T_m	1300 °C
Thermal diffusivity κ	$1\times10^{-6}\mathrm{m}^2\mathrm{s}^{-1}$
Cooling age τ_c	60 Myr
Adiabatic gradient	$0.5\,^{\circ}\mathrm{C/km}$

Assuming a purely thermal origin of lateral perturbation in both wave speed and anelasticity (Q), we follow Ruan & Zhou (2010) and calculate temperature perturbations that correspond to shear wave

speed perturbations in model S20RTS (Ritsema & Van Heijst, 2000) using the temperature partial derivative of shear-wave speed (e.g., Karato, 1993; Ruan & Zhou, 2010),

$$\frac{\partial \ln V}{\partial T} = \frac{\partial \ln V_0}{\partial T} - \frac{1}{Q\pi}\frac{E^* + PV^*}{RT^2}. \tag{3.2}$$

The temperature partial derivative $\partial \ln V/\partial T$ depends on Q, so an iterative approach was used to compute perturbations in Q. The root-mean-square (rms) of the wavespeed and Q models are plotted in Fig 3.1 as a function of depth, and 3-D wavespeed and 3-D Q maps at a depth of 100 km are plotted in Fig. 3.2(a) and (b). The root-mean-square strength of $\delta \ln Q^{-1}$ in the Q model is comparable to recent tomographic 3-D Q models (e.g., Dalton *et al.*, 2008). Assuming current global tomographic 3-D Q models are correct in order of magnitude, our 3-D Q model should be reasonable for the investigation of 3-D anelastic effects on surface waves. The advantage of using the wave-speed-converted Q model is that the Q model is highly correlated with the 3-D wave speed model S20RTS, which allows us to investigate correlations between their corresponding effects.

We investigate the effects of 3-D wave speed and 3-D Q structures on surface wave amplitudes through wave propagation simulation in four different Earth models (Table 3.2) using a Spectral Element Method (Komatitsch & Tromp, 1999, 2002a,b). To examine the elastic focusing/defocusing effects on surface-wave amplitudes due to 3-D wave speed structures, we measure amplitude differences between synthetic seismograms generated in model (I) — 1-D velocity and 1-D Q (PREM) and model (II) — 3-D velocity and 1-D Q (S20RTS). The Q structures in model (I) and (II) are identical, therefore the measured perturbations in surface-wave amplitudes are due to the 3-D velocity structures, i.e., $(A_{\text{3–D V}} - A_{\text{1–D V}})/A_{\text{1–D V}}$ or *elastic* $\delta \ln A$. In the case of examining the effects of 3-D Q structures ("anelastic effects " hereinafter), we measure amplitude perturbations between synthetic seismograms generated in model (III) — 3-D velocity and 1-D Q and model (IV) — 3-D velocity and 3-D Q. The velocity structures are identical in these two models so the amplitude perturbations are due to the 3-D Q structures, i.e., $(A_{\text{3–D Q}} - A_{\text{1–D Q}})/A_{\text{1–D Q}}$ or *anelastic* $\delta \ln A$. The 1-D and 3-D Q

models are shown in Figs 3.1 and 3.2.

Table 3.2: Models used for 3-D SEM wave propagation simulation

	Model	Velocity	Anelasticity (Q)
Elastic effects	I	1D (PREM)	1D (PREM)
	II	3D (S20RTS)	1D (PREM)
Anelastic effects	III	3D (S20RTS)	1D ($\mathbf{Q1DM_M}$)
	IV	3D (S20RTS)	3D ($\mathbf{Q3DM_M}$)

We use twelve earthquake events and 801 seismic stations in our numerical simulations to provide a good global path coverage (Fig. 3.2). For each event, wave propagation simulations are run for all four models in Table 3.2. Examples of synthetic seismograms from SEM simulations and associated ray paths are plotted in Fig. 3.3. The transverse and vertical component seismograms at station BMN have been bandpass filtered between 8 and 15 mHz. The top two seismograms in Fig. 3.3(a) and (b) show amplitude perturbations caused by 3-D Q structures, while the bottom two seismograms show amplitude perturbations caused by 3-D wave speed structures. Amplitude variations measured at a period of 100 s (10 mHz) are shown beneath each two traces. For the transverse component (Love waves), lateral variations in Q cause a 3.5% increase in amplitude while variation in wave speed cause a 133.7% increase in amplitude. In the vertical component (Rayleigh waves), the 3-D Q and 3-D wave speed structures increase amplitude by -1.3% and 42.5% respectively. This indicates elastic effects on surface wave amplitudes, i.e., focusing/defocusing, can be much stronger than anelastic attenuation. In this example, both Love waves and Rayleigh waves show a strong elastic focusing (amplification) on amplitudes as they propagate through strong slow anomalies. We assume lateral heterogeneities in the Earth models are thermally-originated, therefore a slow anomaly is associated with a low Q anomaly where strong anelastic attenuation is expected (decrease in amplitude). However, synthetic seismograms show a slight increase in the amplitude of Love waves and a negligible decrease in the amplitude of Rayleigh waves. Such unexpected variation indicates anelastic focusing effects associated with anelastic dispersion are strong enough to cancel out the attenuation effects. The details of wave focusing effects associate with anelastic dispersion will be discussed in section 3.5.

Amplitude measurements as a function of wave period are shown in Fig 3.3(d) and (e) for Love waves and Rayleigh waves respectively. The strong frequency dependence of amplitude perturbations will be discussed in sections 3.4 and 3.5.

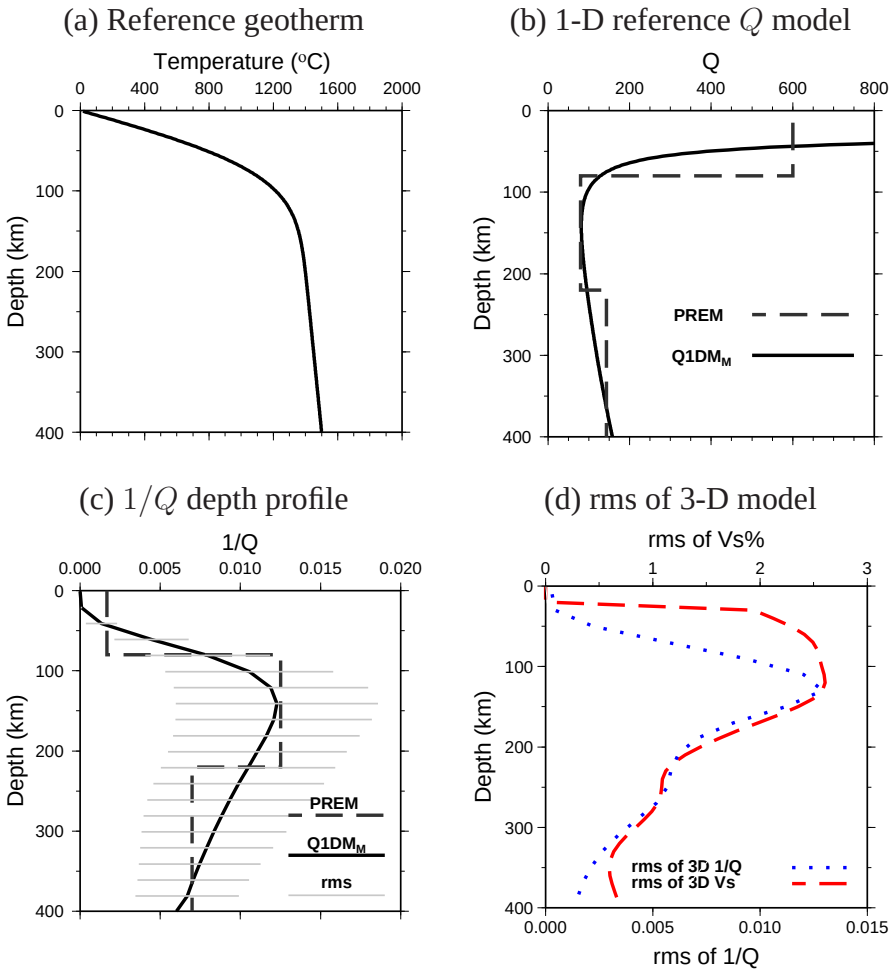

Figure 3.1: (a) Reference 1-D temperature model derived assuming halfspace cooling of an adiabatic mantle. Adiabatic thermal gradient is $0.5\,^{\circ}\mathrm{C/km}$, and geothermal parameters are shown in Table 3.1. (b) Reference Q model (Q_μ) constructed using the reference geotherm and mineralogical parameters $E^* = 470$ KJ/mol and $V^* = 17$ cm^3/mol. PREM Q_μ is also shown in dashed line for reference (Dziewonski & Anderson, 1981). (c) Depth profile of $1/Q$ where gray bars indicate root-mean-square (rms) variations of $1/Q$ at various depths in 3-D Q model. (d) Root-mean-square (rms) of 3-D wave speed and Q models as a function of depth.

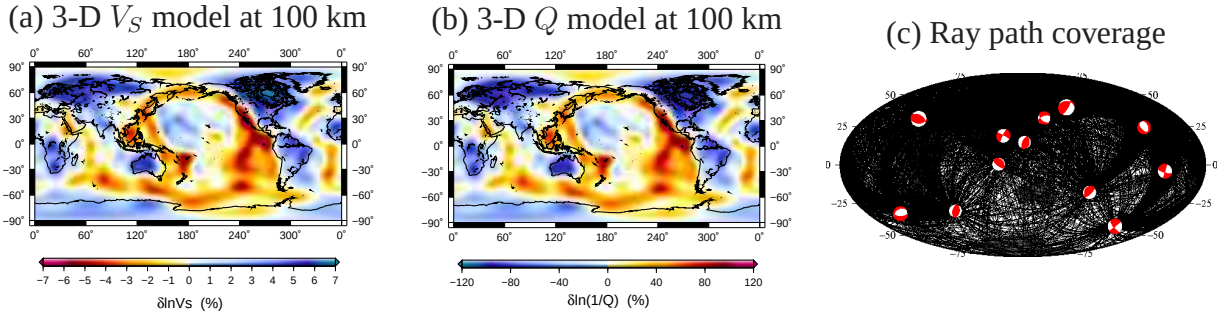

Figure 3.2: (a) 3-D shear wave speed model S20RTS (Ritsema & Van Heijst, 2000) at a depth of 100 km. (b) 3-D anelasticity (Q) model at a depth of 100 km, the perturbation magnitude of Q^{-1} are comparable to recent tomographic models (e.g., Dalton *et al.*, 2008). Note that perturbations in Q model and wave speed model are correlated as we assume both of them are caused by temperature variations. (c) Ray paths used in numerical simulations. Locations and focal mechanisms of the twelve earthquakes are indicated by beachballs.

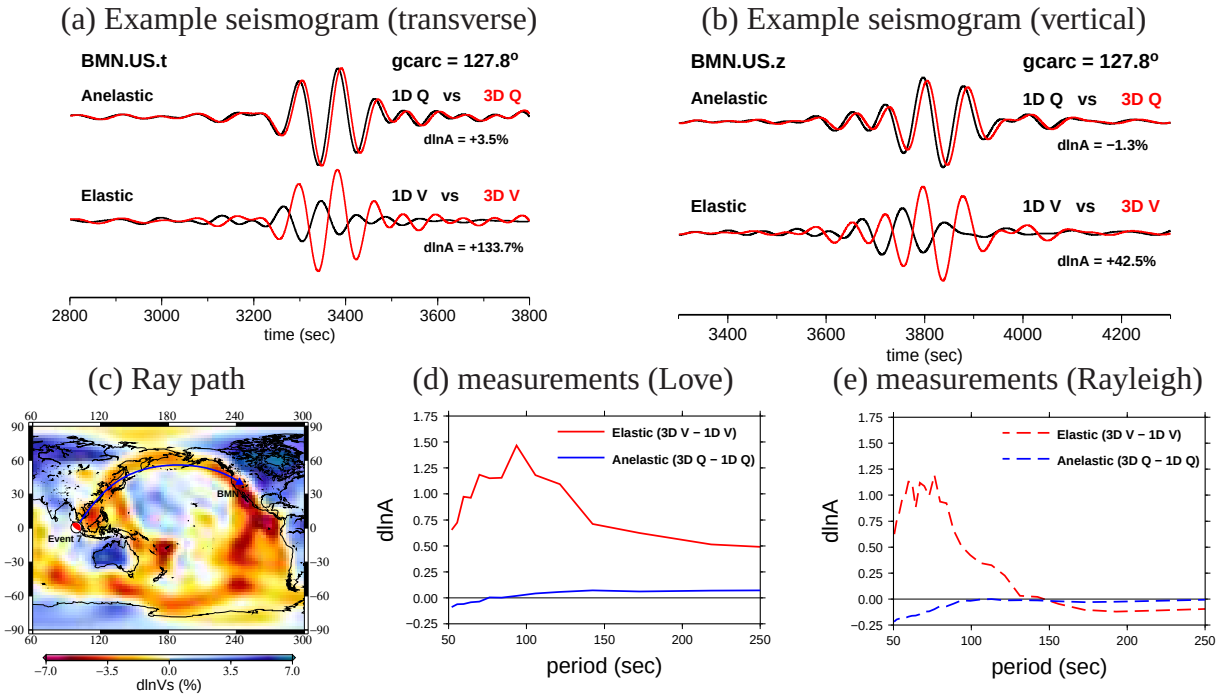

Figure 3.3: (a) transverse and (b) vertical components of synthetic seismograms at station BMN, bandpass filtered between 8 to 15 mHz. Top seismogram pairs show effects due to anelastic perturbations, black seismograms are generated using model (III)–3-D velocity and 1-D Q, red seismograms are generated using model (IV)–3-D velocity and 3-D Q. Bottom seismogram pairs show differences due to elastic perturbations: black seismograms are generated using model (I)–1-D velocity and 1-D Q; red seismograms are generated using model (II)–3-D velocity and 1-D Q. Amplitude perturbations measured at 100 seconds using a multi-taper technique are indicated below the trace pairs. The ray path of the seismograms is shown in (c) and measured elastic and anelastic amplitude perturbations as a function of period are plotted in (d) for Love waves and (e) for Rayleigh waves.

3.3 Measurements of surface wave amplitude variations

To reduce bias in spectral estimation, we measure surface-wave amplitude perturbations using a multi-taper method (MTM) (Laske & Masters, 1996; Zhou *et al.*, 2004). In this study, five 2.5-π prolate spheroidal eigentapers (Slepian, 1978) are used. Seismograms measured with these eigentapers have their spectra narrowly concentrated around the central frequency. Amplitude perturbations and associated errors are estimated by least-square fitting of measurements made with the five orthogonal tapers. We measure fundamental-mode surface wave amplitude perturbations at frequencies (periods) from 5 mHz (200 s) to 20 mHz (50 s).

Time windows are chosen for each seismogram to include group arrivals of surface waves at the period of measurement, and to exclude higher-mode surface waves whenever possible. The spectra of windowed seismograms depend on the time window applied in making measurements. To examine the effects of windowing on amplitude measurements, we compare amplitude perturbations of 100-s Rayleigh waves measured with different time windows. We start with a measurement window that is approximately five times as long as the period of the wave ($\sim$500 s) centered at the arrival of the fundamental-mode surface wave, we then extend the length of the window by 150 seconds in both directions to make it a longer window ($\sim$ 800 s), and the third measurement window is 1100 s centered at the same arrivals. Examples of measurement time windows as well as amplitude variations caused by different measurement time windows are shown in Fig. 3.4. Overall, amplitude variations due to differences in window length can be significant, especially when windows are extended to include higher-mode energy. A longer time window can increase the resolution of amplitude spectra, however, it may also increase the risk of higher-mode contamination. In this study, we carefully choose measurement windows to strike a balance between good spectra resolution and minimum higher-mode contamination. Due to the dispersion of surface waves, we select measurement windows based on visual examination of seismograms band-pass filtered at two different frequency bands, 20-

10 mHz (50-100 s) and 5-10 mHz (100-200 s). The final hand-picked measurement windows range from 600-800 seconds in the period range between 50-100 s and 1000-1600 seconds in the period range between 100-200 s respectively.

Fundamental-mode surface waves in model PREM and S20RTS have different group arrival times. This often makes it difficult to exclude higher-mode surface waves in determining the time window for measurements, especially in the case of Love waves. To examine the possible effects of including higher-mode surface waves in the measurement window, we compare measurements made with and without higher-mode surface waves. In the case with higher modes, we measure amplitude perturbations between seismograms generated in model PREM and S20RTS using SEM, therefore both seismograms include all seismic phases. In the case without higher modes, we measure amplitude perturbations between fundamental-mode-only seismograms generated in model PREM using surface wave mode calculations and seismograms generated in model S20RTS using SEM. Amplitude measurements made with and without higher modes for 100-s Love waves and 100-s Rayleigh waves are shown in Fig. 3.5. Higher-mode surface waves have some effects on Rayleigh wave amplitudes (Fig. 3.5(b)), but in general they are not significant compared to uncertainties in measurements. The effects of higher-mode surface waves are stronger in Love waves than in Rayleigh waves (Fig. 3.5(a)). This is expected because fundamental-mode Rayleigh waves travel much slower than higher-mode Rayleigh waves, but the difference in traveling speed between fundamental-mode Love waves and higher-mode Love waves are much smaller and therefore they are not well separated in seismograms. It's also noteworthy that amplitudes of fundamental-mode and higher-mode surface waves are caused by the same subsurface structures but with different depth sensitivity. Unless the structure varies rapidly with depth, bias introduced by high-mode contamination will be limited, as shown in Fig. 3.5. In Fig. 3.5, the calculations are for an extreme case and effect of higher-mode contamination is in general less significant in the measurements that we will discuss in section 3.4.

The excitation of surface wave amplitudes by a moment tensor source depends on local structure at

the source. In 3D models, local structures in source regions are often different from that in 1D models. In Fig. 3.6, we show that the effects of source radiation differences on surface wave amplitudes are not significant as we have excluded paths close to nodal planes where source local structures may have stronger influences on source excitations. The amplitude variations due to direct source excitation differences are generally smaller than measurement error bars.

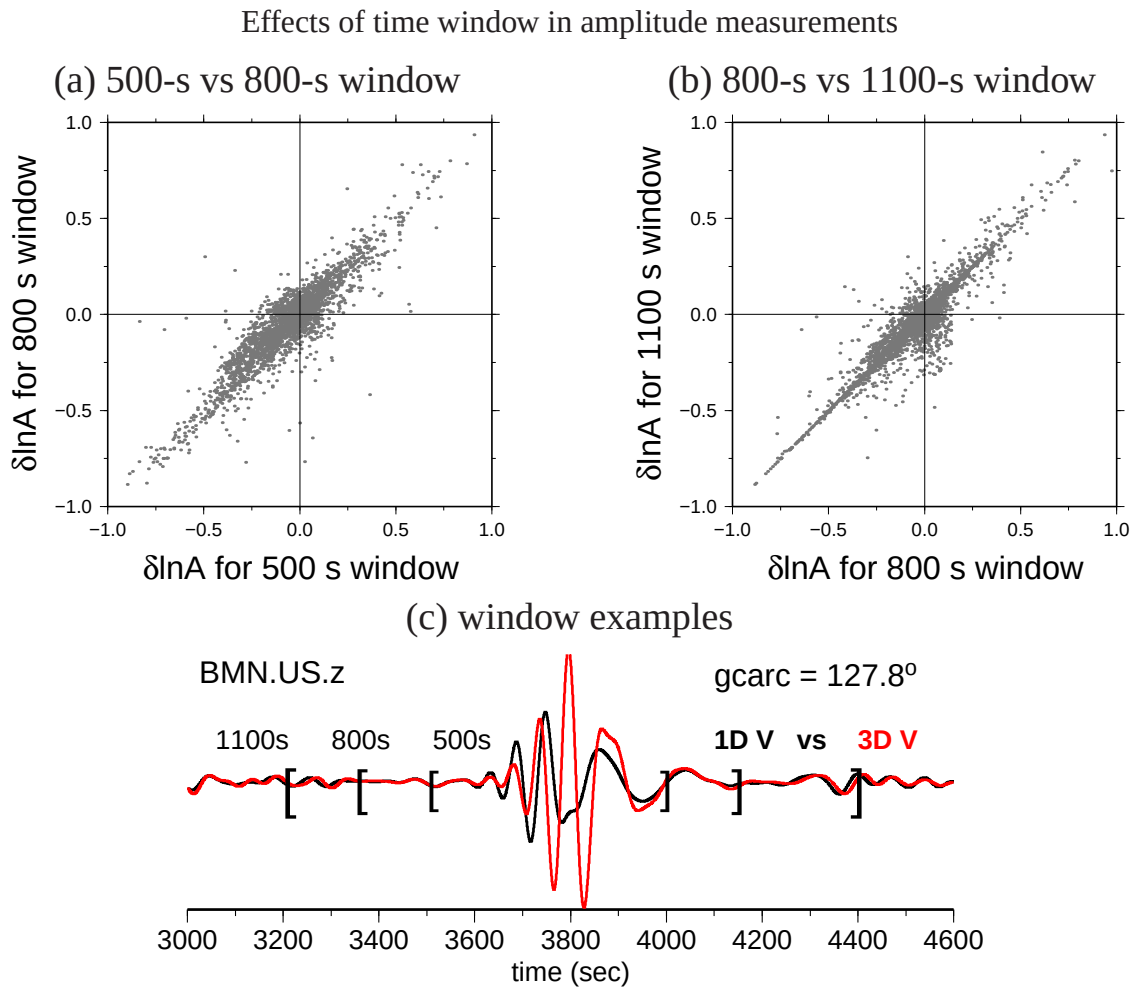

Figure 3.4: Comparison of elastic amplitude variations ($(A_{3DV} - A_{1DV})/A_{1DV}$) of 100 s Rayleigh waves measured with different time windows. (a) shows amplitude perturbations measured using 500-second time windows plotted against measurements made with 800-second time windows, and (b) is the same as (a) but for 800-second time windows and 1100-second time windows. Examples of time windows are shown in (c) for a seismogram at station BMN. The seismogram is the same as in Fig.3.3 (b) but bandpass filtered between 4 mHz and 20 mHz. Amplitude perturbations measured using different windows show significant differences, especially when the time window is long enough to include significant higher-mode energy. Time windows in our study are chosen to provide a good spectra resolution but minimum higher-mode contamination.

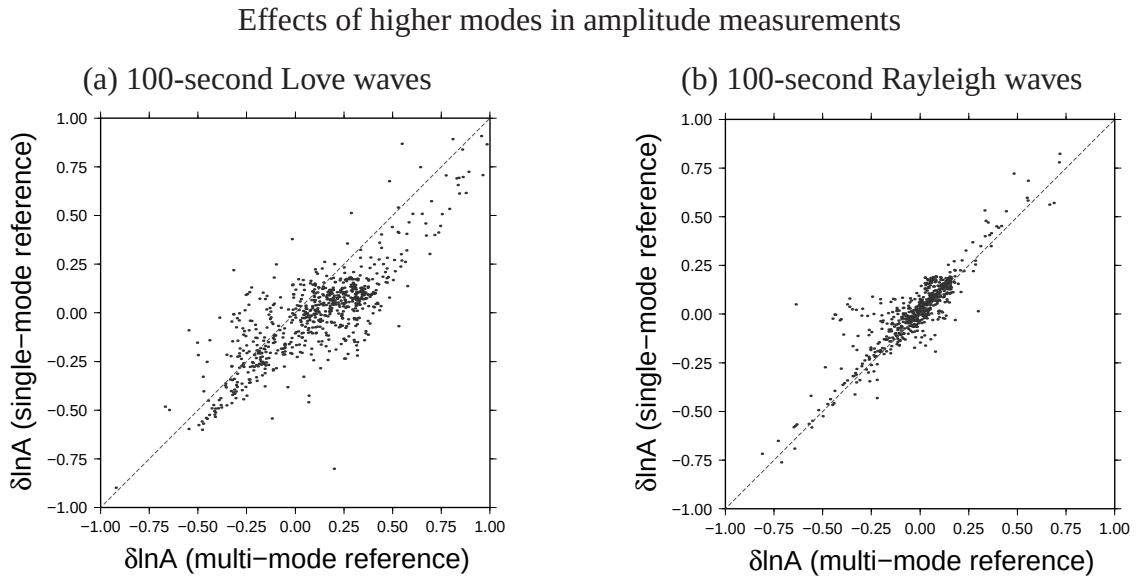

Figure 3.5: Comparison between amplitude perturbation measurements with and without higher-mode surface wave effects. (a) Amplitude measurements made using single-mode reference seismograms plotted against measurements made with multi-mode reference seismograms for 100-s Love waves. In single-mode reference measurements, $\delta \ln A$ is measured between fundamental-mode-only seismograms generated in PREM using surface wave mode calculations and seismograms generated in model S20RTS using SEM. In multi-mode reference measurements, $\delta \ln A$ is measured between seismograms generated in PREM and S20RTS using SEM. (b) is the same as (a) but for 100-s Rayleigh waves.

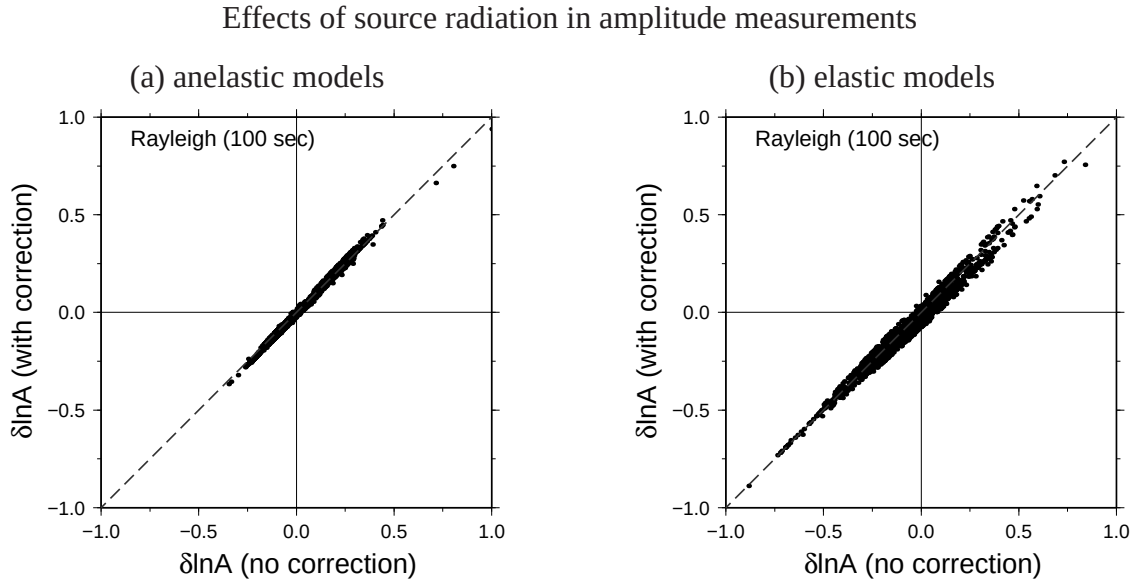

Figure 3.6: Examples of 100-s Rayleigh-wave amplitude measurements made with and without corrections of source radiation differences between 1-D and 3-D models for (a) anelastic models and (b) elastic models. The effects of source radiation differences on amplitudes are not significant compared to measurement error bars.

3.4 3-D anelastic effects on surface waves and frequency dependence

It's well known that amplitudes of seismic waves can be affected by the magnitude of earthquakes, geometrical spreading, source radiation pattern, wave attenuation and focusing/defocusing effects. In this study, we focus on amplitude perturbations caused by wave attenuation and focusing/defocusing effects, and quantify the effects of 3-D wave speed and 3-D Q structure as a function of wave period. Lateral perturbations in wave speed affect the amplitude of seismic waves through elastic focusing/defocusing without energy loss. In the presence of 3-D anelastic heterogeneities, amplitude of seismic waves can be attenuated due to energy loss caused by internal friction in mantle materials. In addition to anelastic attenuation, anelastic structures also cause physical dispersion, introducing additional focusing/defocusing effects which we have referred to as *anelastic focusing/defocusing*. Anelastic focusing/defocusing effects strongly depend upon wave frequency because of physical dispersion. It's worth emphasizing that this type of focusing effects is associated with 3-D Q structures.

In Fig. 3.7, we compare Love- and Rayleigh-wave amplitude variations caused by 3-D wave speed structures, elastic $\delta \ln A$ and those caused by 3-D Q structures, anelastic $\delta \ln A$. Vertical and horizontal coordinates in the scatterplot represent elastic $\delta \ln A$ and anelastic $\delta \ln A$ measured for the same source-receiver pair. Black crosses on each dot show the measurement errors estimated using multi-taper technique. We exclude measurements with large error bars, which leaves approximately 3,000 to 6,000 measurements in each scatterplot.

Our measurements show that 3-D anelastic effects on surface wave amplitudes are frequency dependent; anelastic effects in long-period surface waves are much weaker than in short-period surface waves. For 50-s Love waves (Fig. 3.7(a)), anelastic effects on amplitude are comparable to elastic effects, and they are in general negatively correlated. For surface waves at longer periods (100 s and 200 s), 3-D Q structures cause much smaller amplitude perturbations than 3-D wave speed structures,

i.e., anelastic effects on amplitudes are much weaker than elastic focusing. In addition, the correlation between anelastic effects and elastic focusing is positive, indicating that the dominant effect of 3-D Q structures is anelastic focusing rather than attenuation as anelastic focusing correlates positively with elastic focusing. Similar patterns are seen in Rayleigh waves (Fig. 3.7). In 50-s Rayleigh waves, the effects of 3-D wave speed and 3-D Q structures are almost equally important, and they show roughly a negative correlation. In 100-s and 200-s Rayleigh waves, the anelastic effects become much weaker than elastic focusing/defocusing effects, and correlate positively with elastic focusing effects.

To better illustrate the relative importance of elastic and anelastic effects, we calculate the average absolute amplitude perturbations caused by 3-D wave speed and 3-D Q structures at periods of 50 s, 100 s, 150 s and 200 s (Fig. 3.8). The average absolute amplitude perturbation is defined as

$$|\delta \ln A|_{\text{ave}} = \frac{1}{N} \sum_{i=1}^{N} |\delta \ln A_i|. \tag{3.3}$$

The black bars in Fig. 3.8 indicate amplitude perturbations caused by 3-D wave speed structures (elastic $\delta \ln A$), while the gray bars are those caused by 3-D Q structures (anelastic $\delta \ln A$). At all periods, elastic $\delta \ln A$ is larger than anelastic $\delta \ln A$ except for short-period (50 s) Rayleigh waves where anelastic effects on amplitudes are comparable to elastic focusing effects. This is expected because 50-s Rayleigh waves are more sensitive to the low Q zone (Fig. 3.7), and therefore experience stronger attenuation in amplitude than Love waves. At longer periods ($>$ 100 s), anelastic effects decrease very quickly with increasing wave period, and elastic focusing/defocusing effects dominate surface-wave amplitude variations. We conclude that focusing/defocusing caused by 3-D wave speed structures are the dominant effects in surface wave amplitudes, tomographic studies without full consideration of focusing/defocusing effects may strongly bias tomographic results. In current 3-D Q tomographic studies, elastic focusing/defocusing effects are sometimes ignored (e.g., Gung & Romanowicz, 2004). This does not simply imply that tomographic Q perturbations have been overestimated because to-

mography is often an ill-posed problem due to limited data coverage, noise in data as well as errors in tomographic theory. How errors in tomographic theory are mapped into tomographic models depends on regularization (damping or smoothing) applied in inversions.

The correlation between elastic and anelastic effects on amplitude variations is frequency dependent (Fig. 3.7). At 50 seconds, the correlation between anelastic and elastic effects is largely negative; while at longer periods ($>$ 100 s) the correlation becomes positive. We have assumed lateral heterogeneities in the models are purely thermal, therefore a slow anomaly is associated with a hot region where strong attenuation is expected. A slow anomaly along a ray path will result in elastic focusing (amplification) and therefore an increase in amplitude, while the higher-than-normal temperature of the anomaly will lead to stronger anelasticity. If we assume the dominant effect of a low Q region is anelastic attenuation, an *increase* in elastic $\delta \ln A$ should correspond to a *decrease* in anelastic $\delta \ln A$, and one should expect a "negative" correlation between anelastic and elastic effects on amplitude.

At short period (50 s), the correlation between elastic focusing and anelastic effects is in general negative, the correlation coefficient is -0.05 in Love waves and -0.38 in Rayleigh waves. It's known that elastic focusing/defocusing effects are associated with the roughness (second spatial derivative) of 3-D wave speed structures and the attenuation of amplitudes is associated with 3-D Q structures; lateral variations in Q structures and roughness of wave speed structures are not necessarily well correlated, which explains the small correlation coefficients at short periods where anelastic effects are dominated by wave attenuation.

The correlation between anelastic and elastic effects becomes positive in long-period surface waves (100 s and 200 s). While the positive correlation seems to be "counter-intuitive", it can be well explained by 3-D anelastic focusing/defocusing effects associated with additional wave speed perturbations caused by anelastic dispersion. In anelastic material, relaxation of elastic moduli depends upon the frequency of the waves, resulting in frequency-dependent wave speed, i.e., anelastic

dispersion (Dahlen & Tromp, 1998):

$$c(\omega) = c(\omega_0) \left[1 + \frac{1}{\pi Q} \ln\left(\frac{\omega}{\omega_0}\right)\right], \tag{3.4}$$

where $c(\omega_0)$ is the wave speed at a reference angular frequency ω_0, and Q is the quality factor. In the presence of 3-D Q anomalies, anelastic focusing effects are associated with the roughness (second spatial derivative) of 3-D Q structures. In our Earth model, lateral perturbations in Q and wave speed structures are well correlated, so do the roughness structures of 3-D Q and 3-D wave speed models, therefore a positive correlation between elastic focusing and anelastic effects is expected when the dominant effect of 3-D Q structures is anelastic focusing. At long period ($>$ 100 s), the positive correlation indicates 3-D Q structures affect surface-wave amplitudes mainly through anelastic focusing and anelastic attenuation is minimum.

It is worth noting that wave speeds in anelastic media have been decomposed into "elastic speed" (speed at a reference frequency) and "anelastic speed" associated with additional physical dispersion. At the reference frequency ω_0, "anelastic speed" is strictly zero and independent of Q perturbations (eq. 3.4). The effects of Q perturbations on wavespeed at the reference frequency are included in "elastic wavespeed". If the reference frequency is close to the high-frequency end of a mantle absorption band model, the "elastic speed" will be close to wave speed associated with unrelaxed modulus. In this chapter, we have chosen a reference frequency of 1 Hz for two reasons: (1) mantle models are often developed at a reference frequency of 1 Hz due to limited bandwidth of teleseismic data and (2) our calculations at 1-Hz reference frequency will provide a lower limit estimates of 3-D anelastic dispersion effects in surface wave amplitudes.

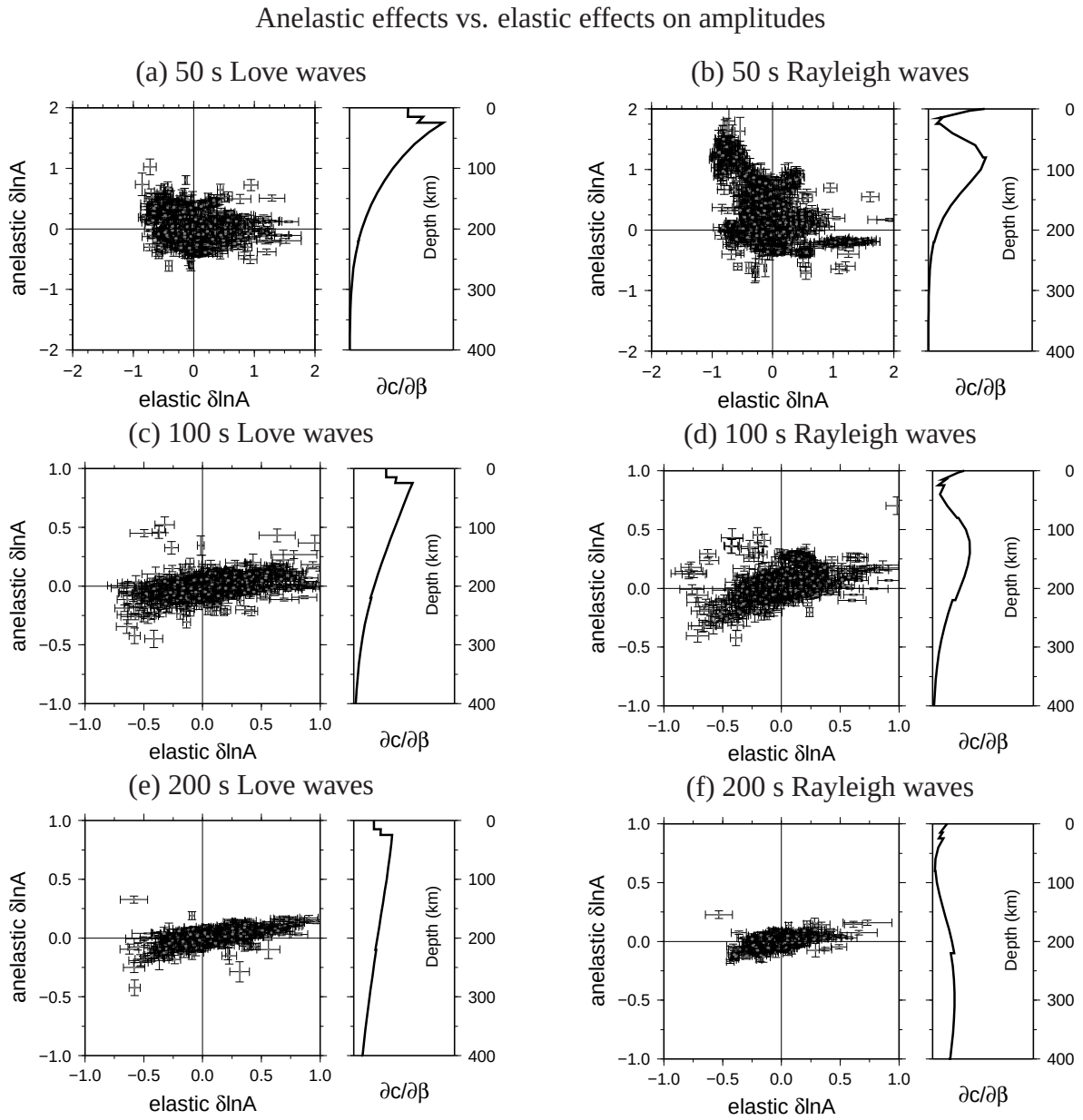

Figure 3.7: Comparison between anelastic and elastic effects on Love- and Rayleigh-wave amplitudes at periods of 50 s, 100 s, and 200 s. Measurement error bars are estimated from multi-taper analysis. Radial sensitivity ($\partial c/\partial \beta$) of fundamental-mode Love and Rayleigh waves are also plotted for reference. At 50 s, the anelastic effects on amplitudes are comparable to elastic effects, they are in general negatively correlated. At longer periods (100 s and 200 s), anelastic effects become weaker with increasing wave period, and begin to show a positive correlation with elastic effects. Anelastic effects in 50- and 100-sec Rayleigh waves are stronger than in Love waves due to its stronger sensitivity to the low Q zone.

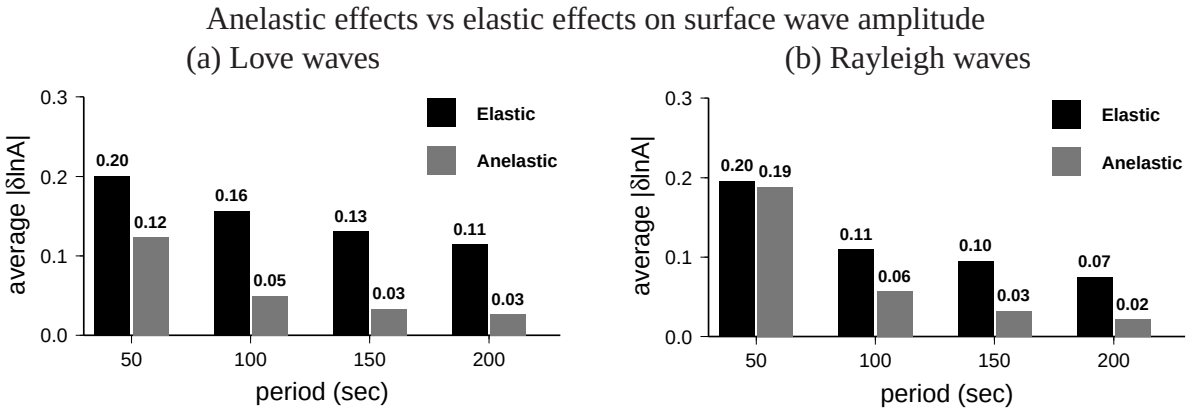

Figure 3.8: Comparison between the anelastic and elastic effects on surface wave amplitudes as a function of periods. The average amplitude perturbations, $|\delta \ln A|$, are calculated using eq. (3.3). Anelastic effects are less significant than elastic focusing on amplitudes except for in short-period (50 s) Rayleigh waves.

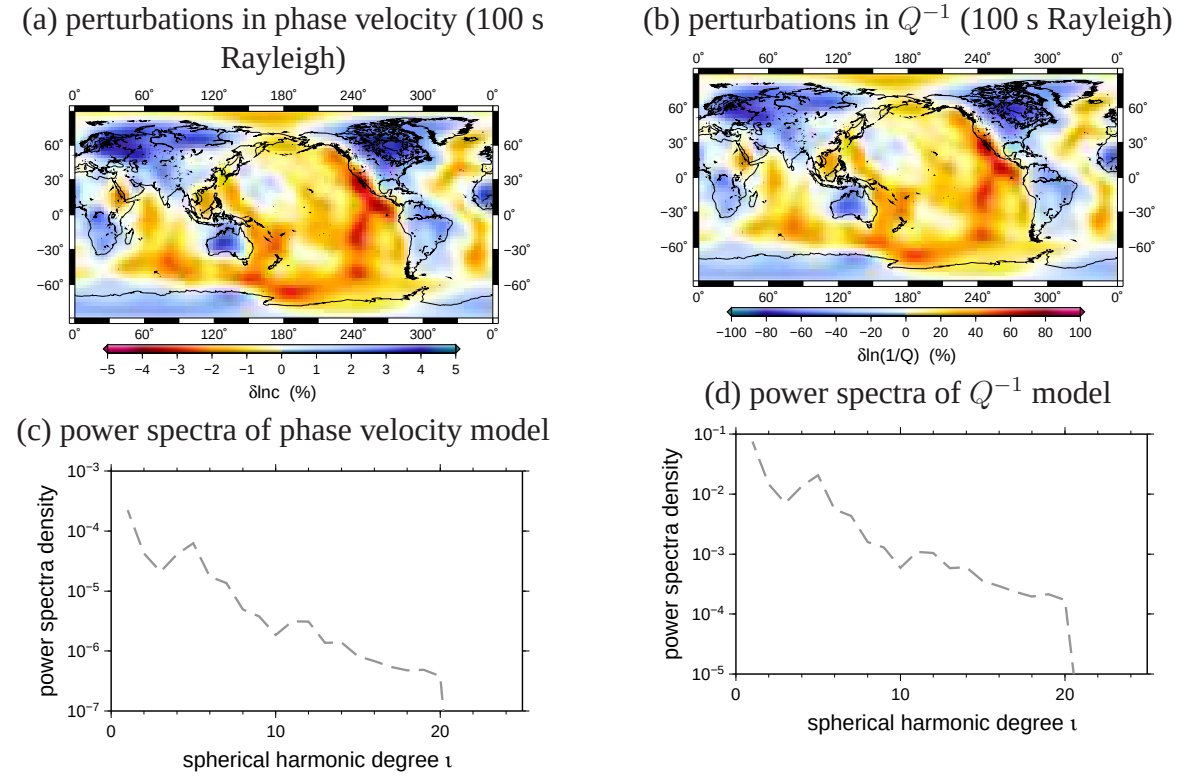

Figure 3.9: (a) Perturbations in 100 s Rayleigh-wave phase velocity due to 3-D wave speed structures. (b) Perturbations in 100 s Rayleigh-wave Q^{-1} due to 3-D Q structures; (c) and (d) are the corresponding power spectra (eq. (3.9)) of perturbations in phase velocity and Q^{-1}. Power density of perturbations in both phase velocity and Q^{-1} models decreases with increasing harmonic degree, indicating that long-wavelength anomalies are dominant in both models.

3.5 Ray-theoretical predictions of surface wave amplitudes

In a 3-D Earth model with lateral variations in both wave speed and anelasticity (Q), amplitude perturbations can be decomposed into three components in the framework of ray theory (Zhou, 2009),

$$\delta \ln A = \delta \ln A_{V\mathrm{foc}} + \delta \ln A_{Q\mathrm{att}} + \delta \ln A_{Q\mathrm{foc}}. \tag{3.5}$$

The first term,

$$\delta \ln A_{V\mathrm{foc}} = \frac{1}{2\sin\Delta} \int_0^\Delta \sin x \, \sin(\Delta - x) \partial_y^2 \frac{\delta c}{c} \, \mathrm{d}x, \tag{3.6}$$

is the elastic focusing/defocusing term which depends on the roughness (second spatial derivatives) of perturbations in phase velocity ($\delta c/c$).

The second term,

$$\delta \ln A_{Q\mathrm{att}} = -\frac{\omega}{2CQ} \int_0^\Delta \frac{\delta Q^{-1}}{Q^{-1}} \, \mathrm{d}x, \tag{3.7}$$

accounts for wave attenuation which depends upon the perturbations of anelasticity (δQ^{-1}).

The third term,

$$\delta \ln A_{Q\mathrm{foc}} = \frac{c}{2\pi CQ \sin\Delta} \ln\left(\frac{\omega}{\omega_0}\right) \int_0^\Delta \sin x \sin(\Delta - x) \partial_y^2 \frac{\delta Q^{-1}}{Q^{-1}} \, \mathrm{d}x, \tag{3.8}$$

accounts for anelastic focusing/defocusing and depends upon the roughness of perturbations in anelasticity. In the above equations, Δ is epicentral distance in radian, c and C are local phase and group velocities measured in $rad \cdot s^{-1}$ on the unit sphere, Q is local Love-wave or Rayleigh-wave quality factor, ω is angular frequency, and integrations are along the great circle ray path. It is worth emphasizing again that anelastic focusing in this chapter is defined with respect to the reference frequency ω_0. At the reference frequency, the third term is zero, it does not indicate that Q perturbations have no affect on amplitudes through anelastic focusing but that the effects have been included in "elastic

focusing" caused by perturbations in "elastic speed" (speed at the reference frequency).

To calculate the ray-theoretical surface-wave amplitude variations caused by 3-D wave speed and 3-D Q structures, we construct local 1-D wave speed and Q models on $2^\circ \times 2^\circ$ cells. This produces 16,200 1-D local models for each of the 3-D models shown in Table 3.2. For each 1-D model, we calculate phase velocities and Q values for both Love waves and Rayleigh waves at periods of 50 s, 100 s, 150 s, and 200 s by solving radial equations for spherically symmetrical Earths models. Phase velocity maps ($\delta c/c$) associated with 3-D wave speed structures are calculated based on model I and model II (Table 3.2). Example phase velocity maps ($\delta c/c$) and Q maps ($\delta Q^{-1}/Q^{-1}$) are shown in Fig. 3.9(a) and (b) for 100 s Rayleigh waves. They are well correlated because both are derived from a thermal model. Note that fractional perturbations in Q^{-1} are about one order of magnitude stronger than in phase velocity. The power spectra of the phase velocity and Q maps are calculated as

$$P_l = \frac{1}{2l+1}\left[a_{l0}^2 + \sum_{m=1}^{l}(a_{lm}^2 + b_{lm}^2)\right], \tag{3.9}$$

where a_{lm} and b_{lm} are the coefficients when the maps are decomposed using the real spherical harmonics (Dahlen & Tromp, 1998, Appendix B),

$$\psi(\theta,\phi) = \sum_{l=0}^{\infty}\left[a_{l0}X_{l0} + \sqrt{2}\sum_{m=1}^{l}X_{lm}(a_{lm}\cos m\phi + b_{lm}\sin m\phi)\right], \tag{3.10}$$

where $\psi(\theta,\phi)$ represents the perturbation field of phase velocity or Q^{-1}. The power spectra are plotted in Fig. 3.9(c) and (d) for 100 s Rayleigh waves. The power spectra of perturbations in both phase velocity and Q^{-1} show that long-wavelength anomalies ($l < 10$) are the dominant features in both models and the power spectra in general decrease with harmonic degree. Roughness of perturbations in phase velocity and Q^{-1} (second spatial derivative) are calculated using surface Laplacian

$$\nabla^2\psi \;=\; \frac{\partial^2\psi}{\partial\theta^2} + \cot\theta\frac{\partial\psi}{\partial\theta} + \frac{1}{\sin^2\theta}\frac{\partial^2\psi}{\partial\phi^2}.$$

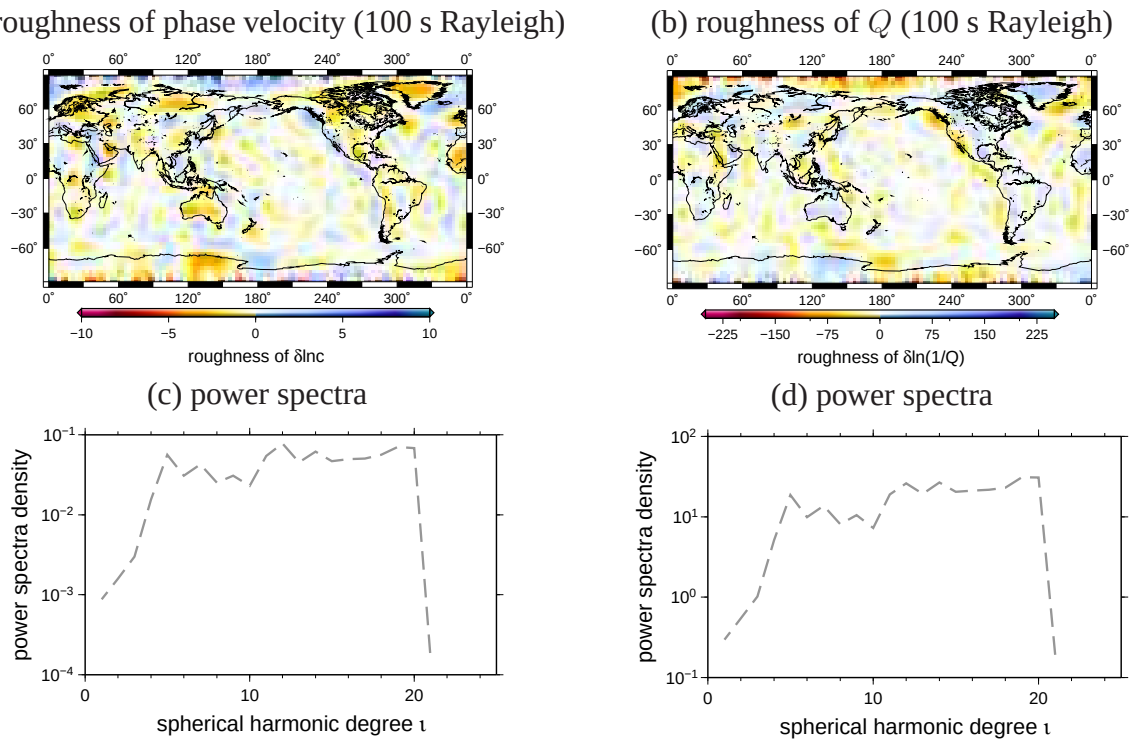

Figure 3.10: Roughness of perturbations in (a) phase velocity and (b) Q^{-1} models for 100-s Rayleigh waves. (c) and (d) are their corresponding power spectra, both show a flat spectra between harmonic degree 5 and 20, indicating larger-scale structures ($l < 5$) are relatively insignificant in the roughness maps. Two roughness maps are well correlated with a correlation coefficient of -0.99.

Example roughness maps for 100 s Rayleigh waves are shown in Fig. 3.10. For both Q^{-1} and phase velocity models, the roughness maps show much smaller scale structures than the perturbation fields in Fig. 3.9, and, unlike the perturbation maps Fig. 3.9, there is no apparent difference between oceans and continents. The roughness map of Q^{-1} and the roughness map of phase velocity are well correlated, and both roughness maps have flat spectra between degree 5 and 20; the largest scale structures ($l < 5$) are relatively insignificant in roughness maps. Given that model S20RTS contains structures limited to harmonic degree $l \leq 20$, we do not expect smaller-scale structures in both phase velocity and Q^{-1} models and their roughness maps.

To calculate ray-theoretical predictions, we compute the second spatial partial derivative (roughness) of $\delta c/c$ and $\delta Q^{-1}/Q^{-1}$ in the direction perpendicular to the geometrical ray path in the ray-

coordinates by rotating the coordinates such that the source and receiver are on the equator. The calculation of the second partial derivatives in path integration can be found in the Appendix.

Ray-theoretical calculations of amplitude perturbations confirm: (1) elastic focusing/defocusing effects caused by 3-D wave speed structures dominate amplitude variations; and (2) anelastic effects caused by 3-D Q structures are important at short period but decrease quickly at longer periods. Fig. 3.11 shows the predicted 3-D elastic focusing/defocusing effects ($\delta \ln A_{V\mathrm{foc}}$) and 3-D anelastic effects ($\delta \ln A_{Q\mathrm{att}}$ + $\delta \ln A_{Q\mathrm{foc}}$) on Love and Rayleigh-wave amplitudes at 50 s, 100 s and 200 s. In short-period surface waves ($\sim$ 50 s), elastic focusing/defocusing effects are comparable to anelastic effects, i.e., $\delta \ln A_{V\mathrm{foc}}$ is comparable to ($\delta \ln A_{Q\mathrm{att}}$ + $\delta \ln A_{Q\mathrm{foc}}$). Elastic effects can cause an amplitude perturbation of approximately $\pm 100\%$ while anelastic effects can result in an amplitude perturbation up to $\pm 75\%$ in 50-s Rayleigh waves, and approximately $\pm 50\%$ in 50-s Love waves. The anelastic effects in Rayleigh waves are relatively stronger than in Love waves at 50 seconds due to their stronger sensitivity in the low Q zone. Elastic and anelastic effects at this period in general show a negative correlation, consistent with SEM simulations in 3-D models. In long-period surface waves ($>$ 100 s), elastic focusing/defocusing effects on amplitudes are the dominant effects, i.e., $\delta \ln A_{V\mathrm{foc}} >> (\delta \ln A_{Q\mathrm{att}}$ + $\delta \ln A_{Q\mathrm{foc}})$. While elastic focusing can cause $\pm 100\%$ amplitude perturbations in both Love and Rayleigh waves, anelastic effects cause approximately $\pm 50\%$ amplitude perturbations in 100 s Rayleigh waves and $\pm 35\%$ in 100 s Love waves, and anelastic perturbations decrease to less than $\pm 25\%$ in both Love waves and Rayleigh waves at 200 seconds. At long periods, anelastic effects and elastic effects are positively correlated.

To better understand the relative importance of anelastic focusing/defocusing and anelastic attenuation in amplitude perturbations as a function of period, we plot anelastic attenuation, $\delta \ln A_{Q\mathrm{att}}$ and anelastic focusing, $\delta \ln A_{Q\mathrm{foc}}$, against elastic focusing, $\delta \ln A_{V\mathrm{foc}}$ in Fig. 3.12. In 50 s Rayleigh waves, as shown in Fig. 3.12(a), the effects of elastic focusing/defocusing and attenuation are comparable ($\delta \ln A_{V\mathrm{foc}} \sim \delta \ln A_{Q\mathrm{att}}$). In general, they are negatively correlated as expected. The correlation

plot shows strong scattering. This is because attenuation ($\delta \ln A_{Q\mathrm{att}}$) depends upon perturbations in Q^{-1} while elastic focusing/defocusing depends upon the roughness of phase velocity perturbations ($\partial_y^2 \delta \ln c$). Although $\delta \ln Q^{-1}$ and $\delta \ln c$ are correlated, $\delta \ln Q^{-1}$ (Fig. 3.9b) and the roughness of $\delta \ln c$ (Fig. 3.10a) are not well correlated. In Fig. 3.12(b), we compare anelastic focusing/defocusing effects with elastic focusing/defocusing effects, and show that they are well correlated as expected based upon the correlation between the roughness maps (Fig. 3.10). Note the roughness $\partial_y^2 \delta \ln c$ and $\partial_y^2 \delta \ln Q^{-1}$ have opposite signs and the $\ln(\omega/\omega_0)$ term in eq. (3.8) is negative as we consider wave frequency lower than reference frequency of 1 Hz. Therefore the correlation between the elastic focusing and anelastic focusing effects is positive.

Ray-theoretical calculations show anelastic attenuation and anelastic focusing/defocusing effects have different frequency dependence. Anelastic attenuation decreases quickly with increasing wave period. At 50 s, anelastic attenuation in Rayleigh waves is comparable to elastic focusing/defocusing, while at 200 s, anelastic attenuation is almost negligible compared with elastic focusing/defocusing ($\delta \ln A_{V\mathrm{foc}} >> \delta \ln A_{Q\mathrm{att}}$) as shown in Fig. 3.12(a) and (c). The decrease of anelastic attenuation with wave period is expected as long-period waves experience fewer cycles compared to short-period waves. However, anelastic focusing/defocusing is much less frequency-dependent than anelastic attenuation. In Fig. 3.12(d), anelastic focusing/defocusing effects ($\delta \ln A_{Q\mathrm{foc}}$) is about 20% of the elastic focusing/defocusing effects ($\delta \ln A_{V\mathrm{foc}}$) in 200 s Rayleigh waves, this ratio is close to the ratio at 50 s. The frequency-independent ratio between elastic and anelastic focusing is a result of largely frequency-independent correlation between velocity and Q models. The correlation coefficient between the roughness field of phase velocity and roughness field of Q^{-1} is -0.99 for 50 s Rayleigh waves and -0.92 for 200 s Rayleigh waves.

We have assumed that mantle heterogeneities in wavespeed and anelasticity are caused by temperature perturbations, therefore, the wave speed and anelasticity models as well as their roughness maps are well correlated. In the mantle, variations in composition, water content and partial melting

may also introduce seismic heterogeneities with roughness structures that may be different from those caused by purely thermal (diffusion) process. In Fig. 3.13, we vary the roughness of the wavespeed and Q models and compare elastic and anelastic ray-theoretical amplitudes. The smoother degree-12 models used in the calculations are the same as the degree-20 models shown in Fig.3.9 but with structures limited to spherical harmonic degrees $l \leq 12$. Compared to calculations in degree-20 models (Fig. 3.11), the scatterplots in Fig. 3.13 show that elastic (or anelastic) focusing effects become weaker in a smoother model where spherical harmonic degree $l > 12$ structures are excluded. This is expected because overall model perturbations are weaker in degree-12 models. The correlation between elastic and anelastic effects also becomes weaker when we compare calculations in degree-12 wavespeed model and degree-20 Q model (or in degree-20 wavespeed model and degree-12 Q model). However, the relative significance of elastic and anelastic effects as well as their frequency dependent correlation are not particular sensitive to model roughness: at 50 seconds, the correlation is largely negative and it becomes positive at longer periods.

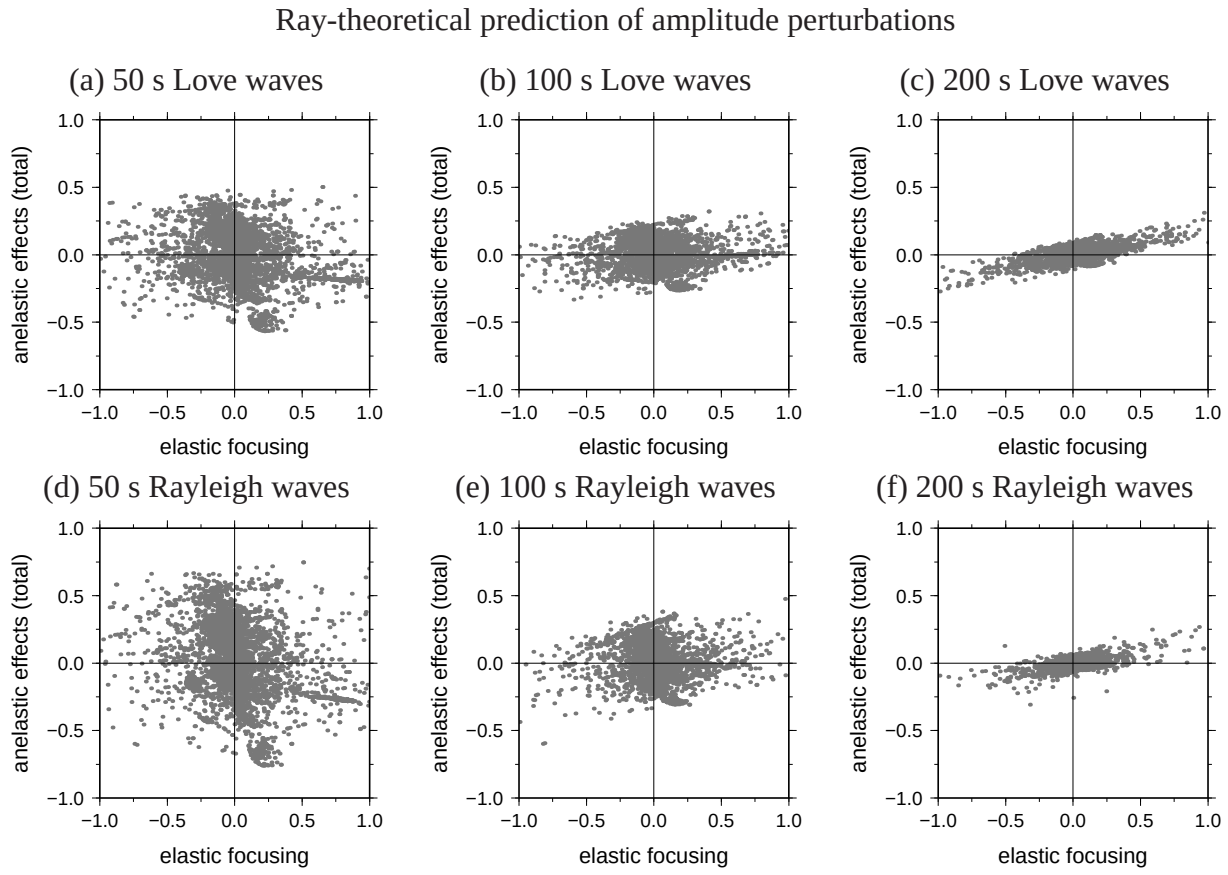

Figure 3.11: Ray-theoretical predictions of 3-D anelastic and 3-D elastic effects on Love- and Rayleigh-wave amplitude variations at periods of 50 s, 100 s and 200 s. At 50 seconds, (a) and (d), anelastic effects on amplitudes are comparable to elastic effects (focusing/defocusing), and they are in general negatively correlated. Anelastic effects on Rayleigh waves are stronger than Love waves due to their better sensitivity to the low Q zone in reference model. At 100 seconds, (b) and (e), anelastic effects become weaker and the correlation between anelastic and elastic effects becomes positive. At 200 seconds, (c) and (f), anelastic effects become very weak, and they are positively correlated with elastic effects.

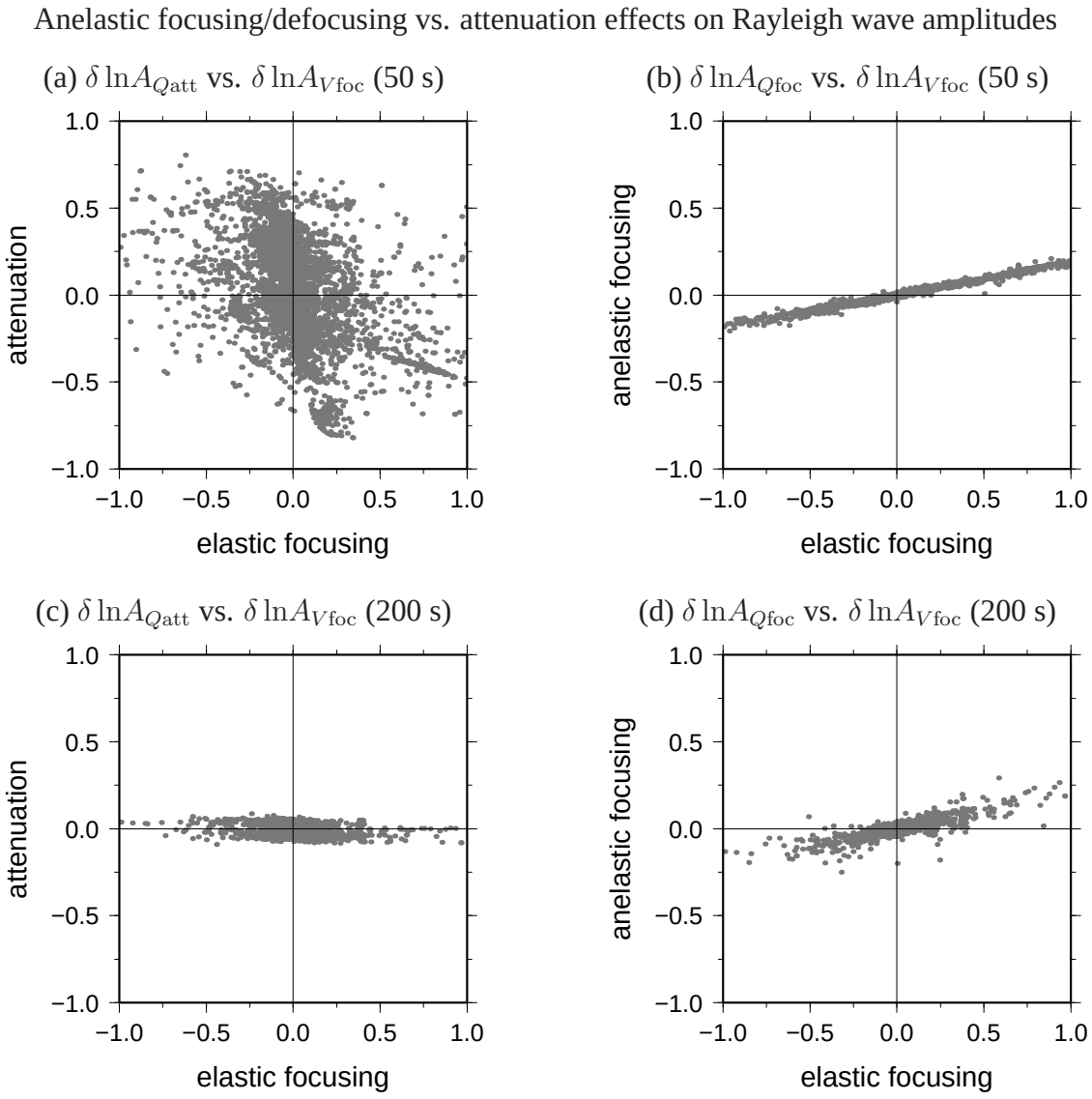

Figure 3.12: Comparison of anelastic attenuation ($\delta \ln A_{Q\mathrm{att}}$) and anelastic focusing/defocusing effects ($\delta \ln A_{Q\mathrm{foc}}$) on Rayleigh wave amplitudes. (a) Anelastic attenuation ($\delta \ln A_{Q\mathrm{att}}$) versus elastic focusing/defocusing ($\delta \ln A_{V\mathrm{foc}}$) on 50-s Rayleigh wave; they are comparable and in general negatively correlated. (b) anelastic focusing/defocusing ($\delta \ln A_{Q\mathrm{foc}}$) versus elastic focusing/defocusing ($\delta \ln A_{V\mathrm{foc}}$), $\delta \ln A_{Q\mathrm{foc}}$ is much weaker than $\delta \ln A_{V\mathrm{foc}}$ and they are positively correlated. (c) and (d) are the same as (a) and (b) but for 200-s Rayleigh waves. At long periods, anelastic attenuation is the least significant effect, i.e., $\delta \ln A_{Q\mathrm{att}} < \delta \ln A_{Q\mathrm{foc}} < \delta \ln A_{V\mathrm{foc}}$.

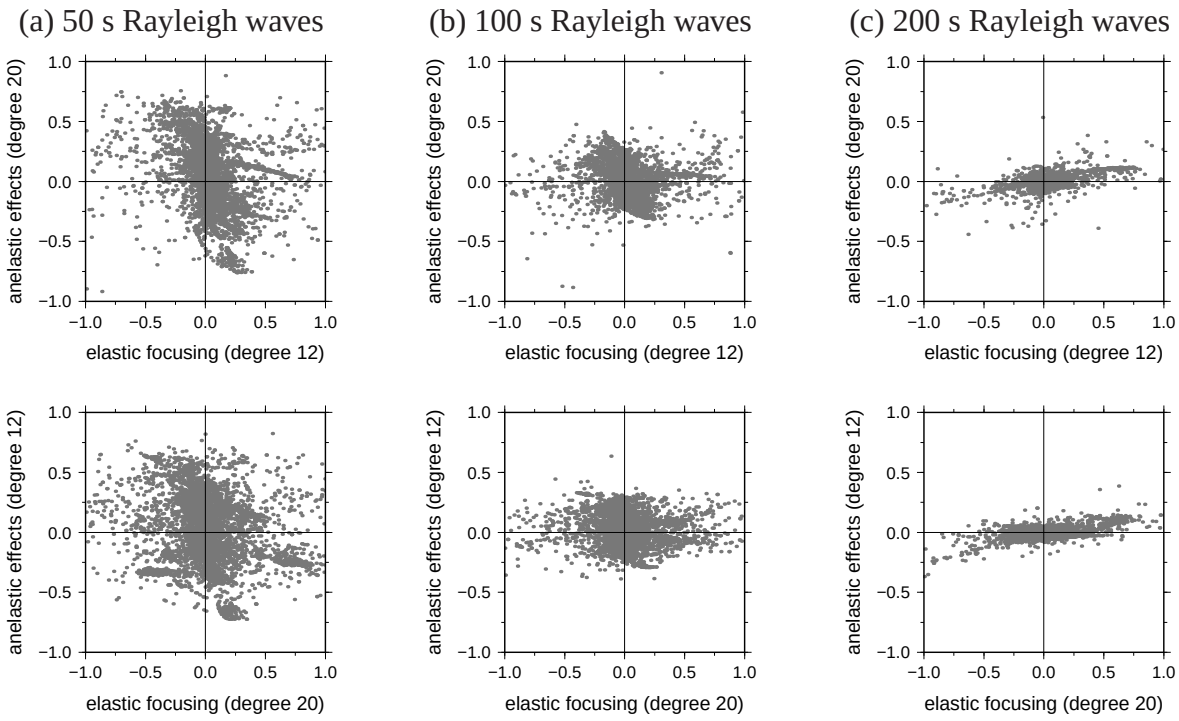

Figure 3.13: Comparison of elastic and anelastic effects calculated in models with different model roughness. The degree-20 models are the same as in Fig. 3.9, and degree-12 models are the same as degree-20 models but with structures limited to spherical harmonic degree $l \leq 12$. Top row in each column shows elastic focusing in degree-20 model versus anelastic effects (attenuation and anelastic focusing) in degree-12 model. Bottom row shows elastic focusing in degree-12 model versus anelastic effects in degree-20 model. Compared to calculations in degree-20 models (Fig. 3.11), elastic (or anelastic) focusing effects become weaker in degree-12 models, and the correlation between elastic and anelastic effects also becomes weaker when we compare calculations in degree-12 wavespeed model and degree-20 Q model (or in degree-20 wavespeed model and degree-12 Q model). However, the relative significance of elastic and anelastic effects as well as their frequency dependent correlation are not particular sensitive to model roughness.

In conclusion, ray-theoretical calculations confirm that elastic focusing/defocusing effects on surface-wave amplitudes caused by 3-D wave speed structures are comparable to anelastic effects caused by 3-D Q structures at short periods ($\sim$50 s); at longer periods ($>$ 100 s), elastic focusing/defocusing effects become dominant. Attenuation effects decrease quickly with wave period and become the least significant effects on amplitude perturbations at long periods, weaker than anelastic focusing/defocusing effects. Our calculations suggest that both elastic focusing and anelastic focusing effects need to be taken into account when long-period surface-wave amplitude data are used in tomographic studies. The effects can be accounted for by joint inversions of wavespeed and Q structure using finite-frequency sensitivity kernels in anelastic media (Zhou, 2009).

3.6 Effects of mineralogical parameters

The construction of the 1-D reference Q model and the 3-D Q model both depend upon mineralogical parameters. In this section, we experiment with two additional parameter sets to examine the dependence of 3-D anelastic effects on mineralogical parameters. The additional sets of mineralogical parameters, $\mathbf{M_L}$ and $\mathbf{M_H}$ are shown in Table 2.2, and their corresponding 1-D Q models, $\mathbf{Q1DM_L}$ and $\mathbf{Q1DM_H}$ are plotted in Fig. 2.8. Compared with PREM Q profile, $\mathbf{Q1DM_L}$ has much smaller Q values while $\mathbf{Q1DM_H}$ has overall larger Q values. The PREM-like 1-D Q model $\mathbf{Q1DM_M}$ is the model we used in Sections 3.3 and 3.4. Following the same algorithm discussed in Section 3.2, we use the additional parameter sets ($\mathbf{M_L}$ and $\mathbf{M_H}$) to construct the corresponding 3-D Q models, $\mathbf{Q3DM_L}$ and $\mathbf{Q3DM_H}$, from the same 3-D wave speed model S20RTS. The 3-D Q models at a depth of 100 km are shown in Fig. 3.14. We simulate wave propagation in these two additional global Q models and make amplitude measurements following the same process as described in Section 3.3.

Comparisons of 3-D elastic effects and 3-D anelastic effects on both Love waves and Rayleigh waves are shown in Fig. 3.14 as a function of period (50 s, 100 s, 150 s, and 200 s) for each mineralog-

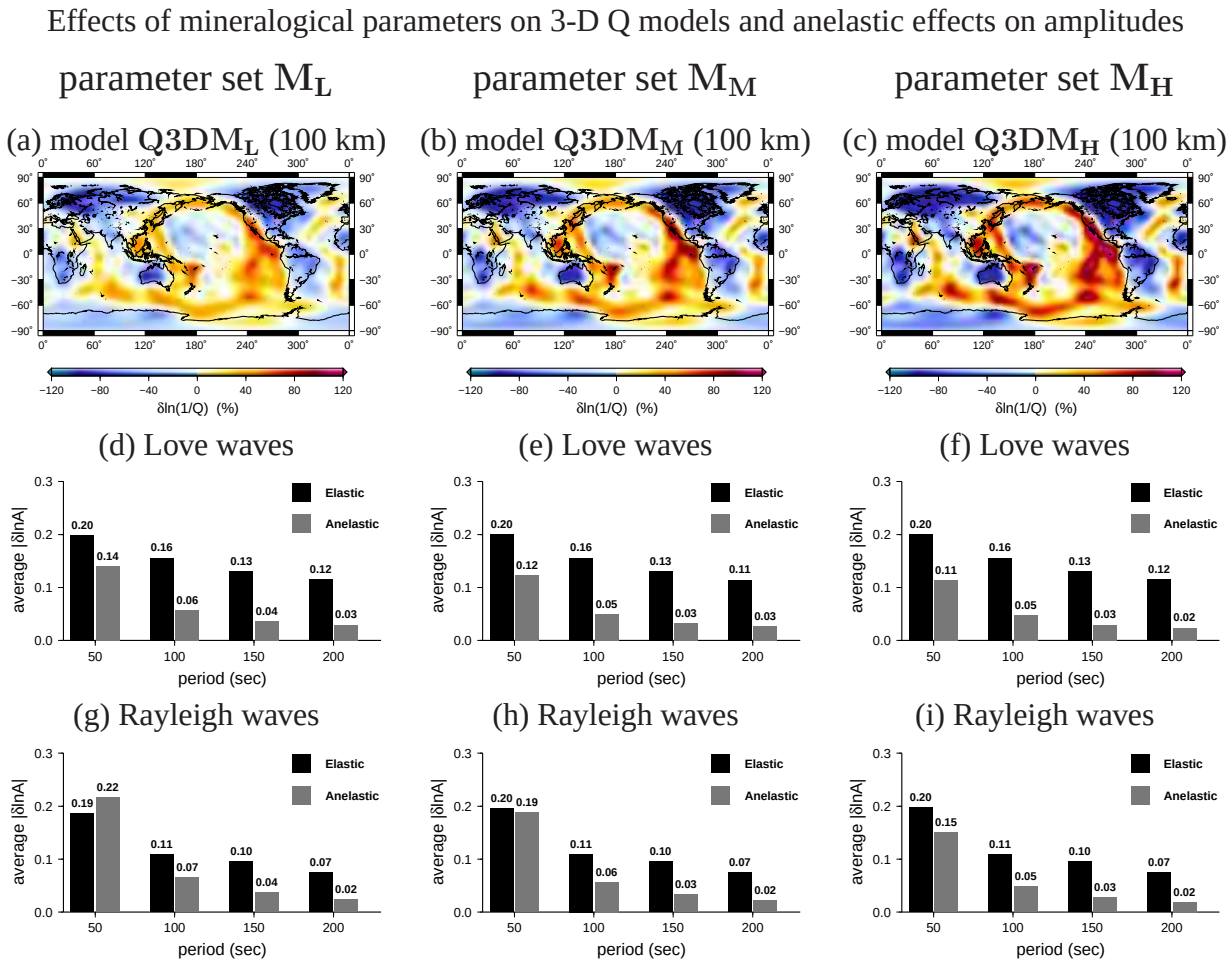

Figure 3.14: Anelastic effects on surface wave amplitudes measured in three 3-D Q models generated using mineralogical parameter sets $\mathbf{M_L}$, $\mathbf{M_M}$, and $\mathbf{M_H}$. (a), (b), and (c) are maps of perturbations in Q^{-1} ($\delta \ln Q^{-1}$) at a depth of 100 km, the corresponding 1-D reference Q models are shown in Fig. 2.8. (d), (e), and (f) are comparisons between anelastic effects (gray bars) and elastic effects (black bars) on amplitude perturbations of Love waves. Amplitude perturbations shown above each bar are the average absolute values,$|\delta \ln A|$. (g), (h), and (i) are the same as (d), (e), and (f) but for Rayleigh waves. Measurements with large error bars have been excluded. Although fractional perturbations in Q^{-1} are the smallest in model $\mathbf{Q3DM_L}$, the absolute amplitude perturbations are the largest among the models due to the associated low Q values in the reference model $\mathbf{Q1DM_L}$ (Fig. 2.8).

ical parameter set. The elastic focusing/defocusing effects on amplitudes (black bars) are identical in these three groups but the anelastic effects (gray bars) are associated with 3-D Q models generated using different mineralogical parameter sets. The values above each bar are average absolute amplitude perturbations ($|\delta \ln A|$).

Our measurements show that 3-D anelastic effects on short-period surface waves depend upon mineralogical parameters. For 50 s Love waves in model $\mathbf{Q3DM_L}$ (parameter set $\mathbf{M_L}$), the average amplitude perturbation $|\delta \ln A|$ caused by 3-D Q structures is 0.14, this value decreases to 0.12 in model $\mathbf{Q3DM_M}$ and to 0.11 in model $\mathbf{Q3DM_H}$. A similar pattern is shown in 50-s Rayleigh waves: the average amplitude perturbation $|\delta \ln A|$ caused by 3-D Q structures is 0.22 in model $\mathbf{Q3DM_L}$, stronger than amplitude perturbations caused by 3-D wave speed structures (0.20), and decrease to 0.19 in $\mathbf{Q3DM_M}$ and 0.15 in model $\mathbf{Q3DM_H}$. At short periods, the dominant effect of 3-D Q structures is anelastic attenuation which depends upon δQ^{-1}. While fractional perturbations $\delta \ln Q^{-1}$ are the weakest in $\mathbf{Q3DM_L}$, absolute perturbations δQ^{-1} are the largest among the models. The effects of variations in mineralogical parameters on anelastic amplitude perturbations are in general small, especially at longer periods ($>$ 100 s). This is because anelastic focusing becomes the dominant anelastic effect at long periods, and it depends upon the roughness of perturbations in Q^{-1} which do not vary greatly with mineralogical parameters, and moreover, anelastic attenuation and anelastic focusing/defocusing have opposite effects on amplitudes.

3.7 Effects of measurement techniques

We have used Slepian multi-tapers to measure amplitude variations in frequency domain. The Slepian multi-taper method (MTM) has been introduced in surface-wave measurements to reduce bias in spectral estimates (e.g., Laske & Masters, 1996; Zhou *et al.*, 2004). In Fig. 3.15, we compare amplitude measurements of 50 s, 100 s, and 200 s Rayleigh waves made with box-car tapers, cosine (Hann)

tapers and Slepian multi-tapers. The comparisons show that amplitude measurements are dependent upon measurement techniques. This is because different tapers emphasizes different part of the seismogram in the measurement window. The differences in measurements can be minimized when when surface waves group energy at measurement frequency arrives approximately at the center of the time window. In practice, the length of the time window is determined by spectra resolution, and arrival-centered measurement windows often include higher-mode energy.

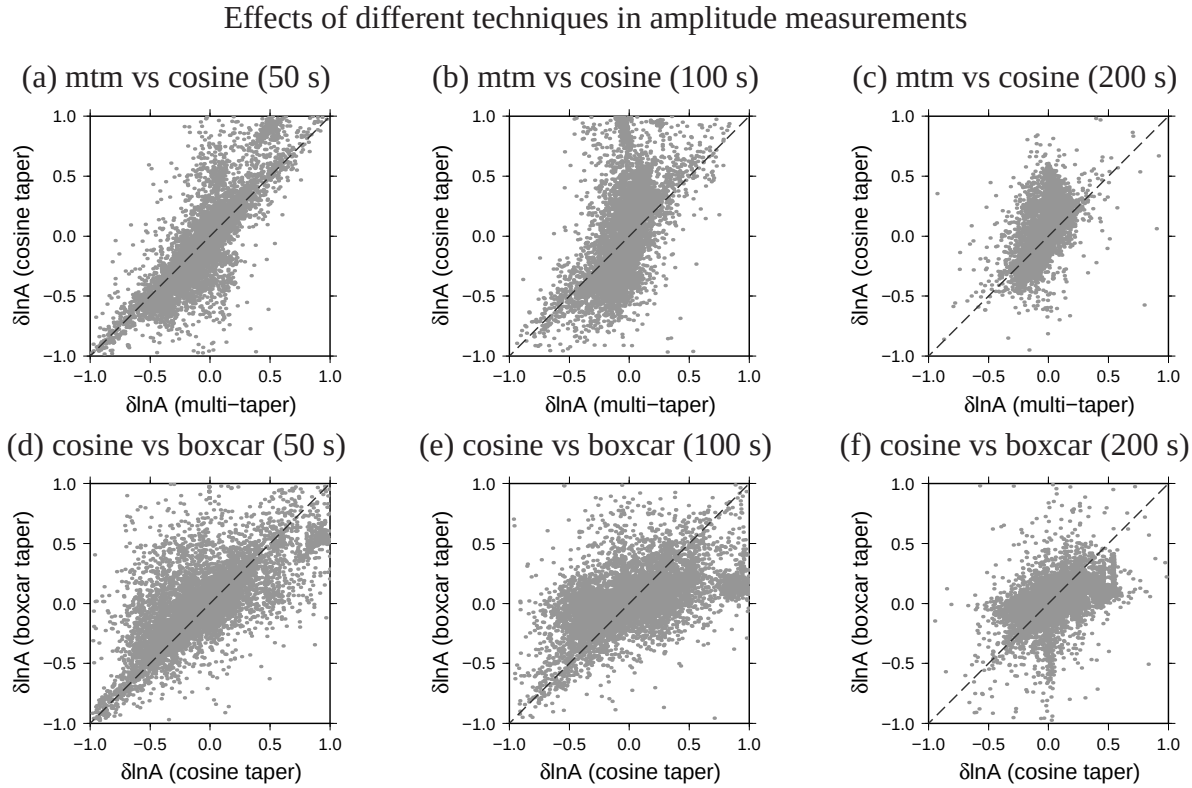

Figure 3.15: Comparison of Rayleigh-wave amplitude variations measured using different measurement techniques at periods of 50 s, 100 s and 200 s. (a), (b) and (c) are multi-taper measurements (mtm) plotted against measurements made with cosine tapers. (d), (e) and (f) are cosine taper measurements versus box-car taper measurements. Note that amplitude perturbations are dependent upon the measurement techniques.

In conclusion, surface wave amplitude measurements are sensitive to measurement techniques. In traditional ray theory, the effects of measurement techniques can not be accounted for. Finite-frequency kernels account for the effects of measurement technique and detailed comparison between SEM measurements and finite-frequency kernel predictions as well as ray-theoretical predictions will

be discussed in chapter 4.

3.8 Discussion and Conclusion

We investigate the effects of lateral variations in both wave speed and anelastic structure (Q) on surface wave amplitudes. Assuming that mantle heterogeneities are dominantly thermal and current tomographic models are accurate in order of magnitude, we construct 3-D Earth models and compute synthetic seismograms using a Spectral Element Method (Komatitsch & Tromp, 1999, 2002a,b). We compare surface-wave amplitude perturbations caused by 3-D wave speed structure with those caused by 3-D anelastic structure. The comparison shows that 3-D anelastic effects on amplitude are significant only in short-period ($\sim$ 50 s) surface waves, and become less significant in long-period (> 100 s) surface waves. The elastic and anelastic effects on amplitude are negatively correlated at short period and the correlation becomes positive at long period because anelastic focusing/defocusing associated with anelastic dispersion becomes stronger than anelastic attenuation.

We calculate ray-theoretical amplitude perturbations of surface waves due to elastic focusing/defocusing ($\delta \ln A_{V\mathrm{foc}}$), attenuation ($\delta \ln A_{Q\mathrm{att}}$) and anelastic focusing/defocusing ($\delta \ln A_{Q\mathrm{foc}}$). The calculations confirm that (1) at short period ($\sim$ 50 s), anelastic effects are comparable with elastic focusing/defocusing ($\delta \ln A_{Q\mathrm{att}} \sim \delta \ln A_{V\mathrm{foc}}$) on surface-wave amplitudes, but decrease rapidly with increasing wave period; (2) at longer period (> 100 s), anelastic attenuation is less significant than anelastic focusing/defocusing ($\delta \ln A_{Q\mathrm{att}} < \delta \ln A_{Q\mathrm{foc}}$); and (3) anelastic focusing is positively correlated with elastic focusing if mantle heterogeneities are dominantly thermal. The frequency dependence of anelastic amplitude perturbations is in general not sensitive to mineralogical parameters used in thermal models, especially at long periods ($>$ 100 s).

Bibliography

Bhattacharyya, J., Masters G., and Shearer P., 1996. Global lateral variations of shear wave attenuation in the upper mantle, *J. geophys. Res.*, **101**, 22,273-22,289.

Dahlen, F. A. & Tromp, J., 1998. *Theoretical Global Seismology*, Princeton University Press, Princeton, New Jersey.

Dahlen, F. A. & Zhou, Y., 2006. Surface-wave group-delay and attenuation kernels, *Geophys. J. Int.*, , **165**, 545–554.

Dalton, C. & Ekström, G., 2006. Constraints on global maps of phase velocity from surface-wave amplitudes, *Geophys. J. Int.*, , **167**, 820–826.

Dalton, C. & Ekström, G., 2006. Global models of surface wave attenuation, *J. geophys. Res.*, **111**, B05317, doi:10.1029/2005JB003997.

Dalton, C., Ekström, G. & Dziewoński, A. M., 2008. The global attenuation structure of the upper mantle, *J. geophys. Res.*, **113**, B09303, doi:10.1029/2007JB005429.

Durek, J. J.,Ritzwoller, M. H., and Woodhouse, J. H., 1993. Constraining upper mantle anelasticity using surface-wave amplitudes, *Geophys. J. Int.*, **114**, 249-272.

Dziewonski, A. M. & Anderson, D. L., 1981. Preliminary reference Earth Model, *Phys. Earth planet. Inter.*, **25**, 297-356.

Faul, U. H. & Jackson, I., 2005. The seismological signature of temperature and grain size variations in the upper mantle, *Earth planet. Sci. Lett.*, **234**, 119-134.

Gung, Y. & Romanowicz, B., 2004. Q tomography of the upper mantle using three-component long-period waveforms, *Geophys. J. Int.*, **157**, 813-830.

Isaak, D. G., 1992. High-temperature elasticity of iron-bearing olivines, *J. geophys. Res.*, **97**, 1871-1885.

Jackson, I., 2000. Laboratory Measurements of Seismic Wave dispersion and Attenuation: Recent Progress., in *Earth's Deep Interior: Mineral Physics and Tomography from the Atomic to the Global Scale, AGU Geophysical Monograph Series*, vol.**117**, S. Karato *et al.* (eds), 265-289.

Jackson, D. D. & Anderson, D. L, 1970. Physical Mechanisms of Seismic-Wave Attenuation, *Rev. Geophys.*, **8**, issue 1, 1-63.

Jackson, I., M. S. Paterson, and J. D. Fitz Gerald, 1992. Seismic wave attenuation in Aheim dunite: An experiment study, *Geophys. J. Int.*, **108**, 517-534.

Jackson, I., J. D. Fitz Gerald, U. H. Faul, and B. H. Tan, 2002. Grain-size-sensitive seismic wave attenuation in polycrystalline olivine, *J. geophys. Res.*, **107**B(12), 2360, doi:10.1029/2001JB001225.

Kanamori, H. & Anderson, D.L., 1977. Importance of physical dispersion in surface-wave and free-oscillation problems - Review: *Rev. Geophys. Space Phys.*, **15**, 105–112.

Karato, Shun-ichiro, 1993. Importance of anelastic in the interpretation of seismic tomography, *Geophys. Res. Lett.*, **20**, NO. 15, 1623-1626.

Karato, Shun-ichiro, 2003. Mapping water content in the upper mantle, in *Inside the subduction factory, AGU Geophysical Monograph Series*, vol.**138**, 135-152, AGU, Washington, D. C.

Karato, S. & Spetzler., H. A., 1990. Defect microdynamics in mineral and solid-state mechanisms of seismic wave attenuation and velocity dispersion in the mantle, *Rev. Geophys.*, **28**, 399-421.

Komatitsch, D. & Tromp, J., 1999. Introduction to the spectral-element method for 3-D seismic wave propagation, *Geophys. J. Int.*, **139**, 806-822.

Komatitsch, D. & Tromp, J., 2002. Spectral-element simulations of global seismic wave propagation—I. Validation, *Geophys. J. Int.,* **149**, 390-412.

Komatitsch, D. & Tromp, J., 2002. Spectral-element simulations of global seismic wave propagation—II. Three-dimensional models, oceans, rotation and self-gravitation, *Geophys. J. Int.*, **150**, 303-318

Laske, G. & Master, G., 1996. Constraints on global phase velocity maps from long-period polarization data, *J. geophys. Res.,* **101**, NO. B7, 16,059-16,075.

Liu, H. P., Anderson, D. L. & Kanamori, H., 1976. Velocity dispersion due to anelasticity; implications for seismology and mantle composition, *Geophys. J. R. astr. Soc.*, **47**, 41-58.

Master, G. & Richards-Dinger, K., 1998. On the efficient calculation of ordinary and generalized spherical harmonics, *Geophys. J. Int.,* **135**, 307-309.

Ritsema, J. & Van Heijst, H. J., 2000. Seismic imaging of structural heterogeneity in Earth's mantle: Evidence for large-scale mantle flow, *Science Progress*, **83**, 243-259.

Romanowicz, B., 1995. A global tomographic model of shear attenuation in the upper mantle, *J. geophys. Res.,* **100**, 12,375-12,394.

Romanowicz, B., 1998. Attenuation Tomography of the Earth's Mantle: A Review of Current Status, *Pure appl. Geophys.*,**153**, 257-272.

Ruan, Y. and Zhou Y. 2010, The effects of 3-D anelasticity (Q) structure on surface wave phase delays, *Geophys. J. Int.,* **181**, 479-492.

Savage, B., Komatitsch, D., & Tromp, J., 2010. Effects of 3D attenuation on seismic wave amplitude and phase measurements, *Bull. seism. Soc. Am.,* **100**, No. 3, 1241-1251, 10.1785/0120090263.

Selby, N. D. & Woodhouse, J. H., 2000. Controls on Rayleigh wave amplitudes: Attenuation and focusing, *Geophys. J. Int.*, **142**, 933-940.

Selby, N. D. & Woodhouse, J. H., 2002. The Q structure of the upper mantle: Constraints from Rayleigh wave amplitudes, *J. geophys. Res.*, **107**, No. B5, 2097, 10.1029/2001JB000257.

Shapiro, N. M. & Ritzwoller, M. H., 2004. Thermodynamic constraints on seismic inversions, *Geophys. J. Int.*, **157**, 1175-1188.

Slepian, D., 1978. Prolate spheroidal wave functions, Fourier analysis and uncertainty, V, The discrete case, *Bell Syst. Tech. J.*, **57**, 1371-1429.

Woodhouse, J. H. & Wong, Y. K., 1986. Amplitude, phase and path anomalies of mantle waves, *Geophys. J. R. astr. Soc.*, **87**, 753-773.

Yang, Y., & D.W. Forsyth, 2006. Regional tomographic inversion of amplitude and phase of Rayleigh waves with 2-D sensitivity kernels, *Geophys. J. Int.*, , **166**, 1148-1160.

Zhou, Y., Dahlen, F. A. & Nolet, G., 2004. Three-dimensional sensitivity kernels for surface wave observables, *Geophys. J. Int.*, **158**, 142-168.

Zhou, Y. 2009. Surface-wave sensitivity to 3-D anelasticity, *Geophys. J. Int.*, **178**, 1403-1410.

3.A Calculation of amplitude focusing

In the computation of the focusing/defocusing of surface-wave amplitudes, we calculate the second spatial derivative (roughness) of perturbations in both phase velocity and Q models. In spherical coordinates the surface Laplacian can be written as,

$$\nabla^2\psi = \frac{\partial^2\psi}{\partial\theta^2} + \cot\theta\frac{\partial\psi}{\partial\theta} + \frac{1}{\sin^2\theta}\frac{\partial^2\psi}{\partial\phi^2}, \tag{3.11}$$

where ψ represents the perturbation field of phase velocity or Q^{-1}. We expand the perturbation field using spherical harmonics

$$\psi(\theta,\phi) \quad = \quad \sum_{l=0}^{\infty}\left[a_{l0}X_{l0}+\sqrt{2}\sum_{m=1}^{l}X_{lm}(a_{lm}\cos m\phi+b_{lm}\sin m\phi)\right], \tag{3.12}$$

where X_{lm} is the spherical harmonics (Dahlen & Tromp, 1998, Appendix B). The roughness of the function, $\nabla^2\psi$, can then be expressed in terms of the real spherical harmonics X_{lm} and its derivative $dX_{lm}/d\theta$,

$$\frac{1}{\sin^2\theta}\frac{\partial^2\psi}{\partial\phi^2} = \sum_{l=0}^{\infty}-\frac{\sqrt{2}}{\sin^2\theta}\sum_{m=1}^{l}X_{lm}m^2(a_{lm}\cos m\phi+b_{lm}\sin m\phi), \tag{3.13}$$

$$\cot\theta\frac{\partial\psi}{\partial\theta} = \sum_{l=0}^{\infty}\cot\theta\left[a_{l0}\frac{dX_{l0}}{d\theta}+\sqrt{2}\sum_{m=1}^{l}\frac{dX_{lm}}{d\theta}(a_{lm}\cos m\phi+b_{lm}\sin m\phi)\right], \tag{3.14}$$

$$\begin{aligned}\frac{\partial^2\psi}{\partial\theta^2} &= \sum_{l=0}^{\infty}\left[a_{l0}\sqrt{l(l+1)}(\cot\theta X_{l1}+\sqrt{(l+2)(l-1)}X_{l2})\right]\\ &+ \sum_{l=0}^{\infty}\left[\sqrt{2}\sum_{m=1}^{l}(-\frac{m}{\sin^2\theta}X_{lm}+m\cot\theta\frac{dX_{lm}}{d\theta}\right.\\ &+ \left.\sqrt{(l+m+1)(l-m)}\frac{dX_{l(m+1)}}{d\theta})(a_{lm}\cos m\phi+b_{lm}\sin m\phi)\right].\end{aligned} \tag{3.15}$$

The roughness maps in Fig. 3.10 are calculated using eqs. (3.13-3.15). In the calculation of the path integrals in eqs (3.6) and (3.8), we rotate the coordinates such that source and receiver are on the equator, and only the colatitudinal second partial derivatives $\partial^2/\partial\theta^2$ are needed after rotation.

The colatitudinal derivative $dX_{lm}/d\theta$ are calculated using a pair of coupled recurrence relations (Master & Richards-Dinger, 1998):

$$X_{l(m-1)} \quad = \quad -\frac{dX_{lm}/d\theta+m\cot\theta X_{lm}}{\sqrt{(l+m)(l-m+1)}}, \tag{3.16}$$

$$\frac{dX_{l(m-1)}}{d\theta} \quad = \quad (m-1)\cot\theta X_{l(m-1)}+\sqrt{(l+m)(l-m+1)}X_{lm} \tag{3.17}$$

For this recurrence relations, the stable iteration direction is downward from $m = l$ to $m = 0$; the starting values in this case are

$$X_{ll} = (-1)^l \left(\frac{2l+1}{4\pi}\right)^{1/2} \frac{\sqrt{(2l)!}}{2^l l!} (\sin\theta)^l, \tag{3.18}$$

$$\frac{dX_{ll}}{d\theta} = l \cot\theta X_{ll}. \tag{3.19}$$

Chapter 4

Finite frequency effects of surface waves in 3-D anelastic earth models

(This Chapter is about to be submitted to the *Geophysical Journal International* as: Ruan, Y. and Zhou Y., Finite frequency effects of surface waves in 3-D anelastic earth models.)

4.1 Introduction

Traditional seismic tomography studies based upon ray theory have been successful in mapping large-scale wave speed heterogeneities in earth's deep interior (e.g., Grand, 1987; Su *et al.*, 1994; Master *et al.*, 1996; Ritsema & Van Heijst, 2000). The limitation of ray-theoretical tomography is poor resolution in imaging heterogeneities of length scales comparable or less than seismic wavelengths. Finite-frequency theory, which can account for diffractional effects of waves, have been developed to improve resolution of small-scale heterogeneities in seismic tomography (e.g., Marquering *et al.*, 1998; Zhao *et al.*, 2000; Dahlen *et al.*, 2000; Zhou *et al.*, 2004; Tromp et al., 2005; Liu & Tromp,

2008).

Recent applications of finite frequency tomography in global and regional studies have led to high resolution models of wave speed structures (e.g., Zhou *et al.*, 2006; Tape *et al.*, 2009; Tian *et al.*, 2009; Tape *et al.*, 2010; Tian *et al.*, 2011). Compared to 3-D wave speed tomography models, current 3-D Q tomography models based upon ray theory are mapped at relative lower resolution ($\leq$ degree 12) and they considerably differ from each other (e.g., Gung & Romanowicz, 2004; Dalton *et al.*, 2008). This is mainly due to the fact that amplitudes can be strongly affected by wave focusing and defocusing caused by 3-D wave speed structures. In addition, windowing and tapering techniques can influence the measurements of surface wave amplitude perturbations (Ruan & Zhou, 2012), and this effect can not be accounted for in ray theory. To overcome these shortcomings of ray theory, finite frequency kernels have been developed for wave speed perturbations (Zhou *et al.*, 2004) and for Q perturbations in elastic reference models (Dahlen & Zhou, 2006), and have been further extended to anelastic reference model for anelasticity perturbations (Zhou, 2009). These kernels can fully account for coupling effects of 3-D wave speed and 3-D Q structures on surface wave travel times and amplitudes which have been shown to be important in recent numerical wave propagation experiments. Ruan & Zhou (2010) showed that about 15-20 per cent of observed phase delays in long-period surface wave ($>$ 50 s) are caused by 3-D Q through anelastic (physical) dispersion. In Ruan & Zhou (2012), elastic focusing effects due to 3-D wave speed are dominant on amplitude perturbations of long-period surface waves, and a long-been-ignored *anelastic* focusing and defocusing effects on amplitude caused by 3-D anelastic dispersion can be more significant that attenuation in long periods ($>$ 100 s).

In this Chapter we shall compare ray theory and finite frequency theory in predicting surface-wave amplitudes and travel times to investigate finite frequency effects. We simulate wave propagation in a shear wave speed model S20RTS and a 3-D Q model using Spectral Element Method (SEM). The 3-D Q model is constructed from S20RTS assuming lateral perturbations in both wave speed and anelasticity are caused by temperature perturbations. As expected, comparisons between theoretical

predictions and SEM measurements at period range of 50 s to 200 s show that finite frequency effects are stronger in long-period surface waves due to its longer wavelength and a wider Fresnel zone. Finite frequency effects in amplitudes are shown to be stronger than those in phase delays in 3-D wave speed model due to the fact that amplitudes are sensitive to the second derivative of wave speed structures while travel times depend on wave speed itself. Finite frequency effects in 3-D Q models are relatively weaker than in 3-D wave speed models and become pronounced only at long period (200 s). The 3-D wave speed and anelasticity model we used contain anomalies at length scale larger than harmonic degree 20. Therefore, finite frequency effects shown in this study probably under represent the effects in the real earth where smaller scale heterogeneities are expected.

4.2 Surface wave finite-frequency kernels

In this section, we will briefly review surface wave Born theory in the presence of 3-D elastic and 3-D anelastic heterogeneities in Zhou *et al.* (2004) and Zhou (2009). First, we consider a spherically symmetric reference earth model subject to perturbations in elastic parameters. In response to the perturbations in reference model, the vertical, radial or transverse component displacement seismogram can be written as $s(\omega) + \delta s(\omega)$, where $s(\omega) = A(\omega)e^{i\phi(\omega)}$ represents the seismogram in reference model and $\delta s(\omega)$ represents the perturbation in displacement, and ω is the angular frequency of wave. To the first order, measured phase delays and amplitude perturbations are associated with perturbations in displacement (Zhou *et al.*, 2004),

$$\delta\phi(\omega) = -\mathrm{Im}\left(\frac{\delta s(\omega)}{s(\omega)}\right), \qquad \ln\left(1 + \frac{\delta A(\omega)}{A(\omega)}\right) = \mathrm{Re}\left(\frac{\delta s(\omega)}{s(\omega)}\right). \tag{4.1}$$

Commonly in tomographic practice, a time domain taper or multitapers are applied to estimate the spectra of displacement seismograms. The tapered reference seismograms and their perturbations can

be expressed as

$$s_j(\omega) = s(\omega) \otimes h_j(\omega), \qquad \delta s_j(\omega) = \delta s(\omega) \otimes h_j(\omega), \tag{4.2}$$

where $h_j(\omega)$ denotes the spectrum of the jth taper $h_j(t)$, $j = 1, ..., N$, and $\otimes$ is the convolution operator. Taking into account the effects of tapering, measured phase delays and amplitude perturbations are then expressed as (Zhou *et al.*, 2004),

$$\delta\phi(\omega) = -\mathrm{Im}\left[\frac{\sum_j \delta s_j(\omega) s_j^*(\omega)}{\sum_j s_j(\omega) s_j^*(\omega)}\right], \qquad \ln\left(1 + \frac{\delta A(\omega)}{A(\omega)}\right) = \mathrm{Re}\left[\frac{\sum_j \delta s_j(\omega) s_j^*(\omega)}{\sum_j s_j(\omega) s_j^*(\omega)}\right], \tag{4.3}$$

where $s_j^*(\omega)$ is complex conjugate of $s_j(\omega)$. Based on single-scattering (Born) approximation, phase delays and amplitude perturbations are linearly related to the fractional perturbations in P-wave speed (α), S-wave speed (β), and density,

$$\delta\phi(\omega) = \iiint_{\oplus} \left[K_\phi^\alpha \left(\frac{\delta\alpha}{\alpha}\right) + K_\phi^\beta \left(\frac{\delta\beta}{\beta}\right) + K_\phi^\rho \left(\frac{\delta\rho}{\rho}\right)\right] d^3\mathbf{x}, \tag{4.4}$$

$$\ln\left(1 + \frac{\delta A(\omega)}{A(\omega)}\right) = \iiint_{\oplus} \left[K_A^\alpha \left(\frac{\delta\alpha}{\alpha}\right) + K_A^\beta \left(\frac{\delta\beta}{\beta}\right) + K_A^\rho \left(\frac{\delta\rho}{\rho}\right)\right] d^3\mathbf{x}, \tag{4.5}$$

where $K_\phi^{\alpha,\beta,\rho}(\omega, \mathbf{x})$ and $K_A^{\alpha,\beta,\rho}(\omega, \mathbf{x})$ are the corresponding phase and amplitude sensitivity kernels to wave speed and density perturbations (Zhou *et al.*, 2004).

In the presence of lateral perturbations in anelasticity (Q), phase delays and amplitude perturbations are associated with fractional perturbations in Q_μ^{-1} and Q_κ^{-1},

$$\delta\phi(\omega) = \iiint_{\oplus} \left[K_\phi^{Q_\mu} \left(\frac{\delta Q_\mu^{-1}}{Q_\mu^{-1}}\right) + K_\phi^{Q_\kappa} \left(\frac{\delta Q_\kappa^{-1}}{Q_\kappa^{-1}}\right)\right] d^3\mathbf{x}, \tag{4.6}$$

$$\ln\left(1 + \frac{\delta A(\omega)}{A(\omega)}\right) = \iiint_{\oplus} \left[K_A^{Q_\mu} \left(\frac{\delta Q_\mu^{-1}}{Q_\mu^{-1}}\right) + K_A^{Q_\kappa} \left(\frac{\delta Q_\kappa^{-1}}{Q_\kappa^{-1}}\right)\right] d^3\mathbf{x}, \tag{4.7}$$

where $K_\phi^{Q_\mu,Q_\kappa}(\omega, \mathbf{x})$ and $K_A^{Q_\mu,Q_\kappa}(\omega, \mathbf{x})$ are the phase delay and amplitude sensitivity kernels to per-

turbations in Q_μ^{-1} and Q_κ^{-1}. These kernels are related to wave speed kernels (Zhou, 2009),

$$K_\phi^{Q_\mu} = -\frac{1}{2Q_\mu}(K_A^\beta + \gamma K_A^\alpha) + \frac{1}{\pi Q_\mu}(K_\phi^\beta + \gamma K_\phi^\alpha)\ln\left(\frac{\omega}{\omega_0}\right), \tag{4.8}$$

$$K_A^{Q_\mu} = \frac{1}{2Q_\mu}(K_\phi^\beta + \gamma K_\phi^\alpha) + \frac{1}{\pi Q_\mu}(K_A^\beta + \gamma K_A^\alpha)\ln\left(\frac{\omega}{\omega_0}\right), \tag{4.9}$$

$$K_\phi^{Q_\kappa} = -\frac{1}{2Q_\kappa}(1-\gamma)K_A^\alpha + \frac{1}{\pi Q_\kappa}(1-\gamma)K_\phi^\alpha\ln\left(\frac{\omega}{\omega_0}\right), \tag{4.10}$$

$$K_A^{Q_\kappa} = \frac{1}{2Q_\kappa}(1-\gamma)K_\phi^\alpha + \frac{1}{\pi Q_\kappa}(1-\gamma)K_A^\alpha\ln\left(\frac{\omega}{\omega_0}\right). \tag{4.11}$$

Where

$$\gamma = \frac{4}{3}\frac{\beta^2}{\alpha^2},$$

and $\omega_0 = 2\pi f_0$ is the reference angular frequency of the earth model, commonly f_0 is chosen to be 1 Hz in seismic tomography. In this Chapter, we shall focus on perturbations in shear wave speed, $\delta\beta$, and perturbations in shear quality factor, δQ_μ^{-1}, for the following reasons: (1) surface waves are most sensitive to S-wave speed, and Rayleigh waves have some sensitivities to P-wave structures only at shallow depths; (2) bulk quality factor Q_κ is orders of magnitude larger than shear quality factor Q_μ, and surface-wave sensitivity to perturbations in Q_κ^{-1} is much weaker than the sensitivity to perturbations in Q_μ^{-1}.

Following Zhou *et al.* (2004) and Zhou (2009), the 3-D finite frequency kernels can be reduced to 1-D integrals along the great circle path based upon a paraxial, forward-scattering approximation. The ray-theoretical phase delays and amplitude perturbations due to elastic wave speed variations can

be written as (Zhou *et al.*, 2004)

$$\delta\phi(\omega) = -k\int_0^{\Delta}\frac{\delta c}{c}dx, \tag{4.12}$$

$$\ln\left(1+\frac{\delta A(\omega)}{A(\omega)}\right) = \frac{1}{2\sin\Delta}\int_0^{\Delta}\sin x\sin(\Delta-x)\partial_y^2\frac{\delta c}{c}dx. \tag{4.13}$$

Where k is the wave number, c is the phase velocity, and Δ is the epicentral distance. Here amplitude perturbations are caused by elastic focusing and defocusing as they are associated with the second derivative of phase velocity perturbations. For 3-D anelastic perturbations, ray-theoretical phase delays can be written as (Zhou, 2009)

$$\begin{aligned}\delta\phi(\omega) = & -\frac{\omega}{\pi CQ}\ln\left(\frac{\omega}{\omega_0}\right)\int_0^{\Delta}\frac{\delta Q^{-1}}{Q^{-1}}dx \\ & -\frac{c}{4CQ\sin\Delta}\int_0^{\Delta}\sin x\sin(\Delta-x)\partial_y^2\frac{\delta Q^{-1}}{Q^{-1}}dx,\end{aligned} \tag{4.14}$$

where the first term accounts for anelastic dispersion and the second term has no direct physical meaning. The dominant term on phase delays is the dispersion term as pointed out in Zhou (2009). Ray-theoretical amplitude perturbations due to 3-D Q can be written as

$$\begin{aligned}\ln\left(1+\frac{\delta A(\omega)}{A(\omega)}\right) = & \frac{\omega}{2CQ}\int_0^{\Delta}\frac{\delta Q^{-1}}{Q^{-1}}dx \\ & +\frac{c}{2\pi CQ\sin\Delta}\ln\left(\frac{\omega}{\omega_0}\right)\int_0^{\Delta}\sin x\sin(\Delta-x)\partial_y^2\frac{\delta Q^{-1}}{Q^{-1}}dx,\end{aligned} \tag{4.15}$$

where Q is the Love-wave or Rayleigh-wave quality factor and C is the group velocity of the wave. Effects of variations in Q^{-1} on amplitude perturbations are twofold: (1) attenuation, which is associated with energy loss and directly depends on the variations in Q^{-1}, and (2) anelastic focusing, which is caused by anelastic dispersion and associated with the second derivative of variations in Q^{-1}.

4.3 Kernel examples

Examples of 100 s Rayleigh-wave phase delay and amplitude kernels to shear wave speed (K_ϕ^β, K_A^β) are shown in Fig. 4.1. These kernels are calculated in PREM (Dziewonski & Anderson, 1981) at a reference frequency of 1 Hz. Phase and amplitude kernels are similar in magnitude but the amplitude kernel is more oscillatory than the phase kernels, indicating that surface wave amplitudes are more sensitive to the geometry of the anomalies. Fig. 4.2 shows phase and amplitude sensitivities to perturbations in Q^{-1} ($K_\phi^{Q_\mu}, K_A^{Q_\mu}$). These kernel examples are also calculated for 100 s Rayleigh waves in PREM. Q kernels are very similar to the wave speed kernels in Fig. 4.1 but they have opposite polarities, this is expected because, in general, an increase in Q^{-1} will attenuate wave amplitudes and increase phase delays through dispersion, while an increase in wave speed will decrease amplitudes through defocusing and decrease phase delays.

Seismic phase delays and amplitudes are sensitive to windowing and tapering techniques as they will affect the spectra of seismograms. This is especially the case for seismic surface waves due to their strong dispersive characteristics (e.g., Ruan & Zhou, 2012). Taking into account measurement technique in the calculation of sensitivity kernels is therefore important. One advantage of finite frequency theory over ray theory is that the effects of tapering can be accounted for in kernel calculation. The time-domain windowing and tapering process corresponds to a convolution of seismogram's spectra with the spectra of taper(s). Significant effects of measurement techniques (tapers) on surface wave phase-delay kernels have been shown in Zhou *et al.* (2004), and the effects on amplitude kernels are also illustrated in Fig. 4.3. Example seismograms calculated in PREM and S20RTS are shown with amplitude and phase delays measurements indicated above them. Amplitude perturbations in 100 s Rayleigh waves measured using cosine taper and multitaper (prolate spheroidal eigentapers) are -0.38 and -0.18, demonstrating a strong dependence of amplitude measurements on tapering. Map views of wave speed sensitivity kernels corresponding to measurements made with different tapers

are plotted at depth of 100 km. These kernels are calculated for cosine taper and multi-taper with an approximately 1200 seconds time window. The multi-taper kernel shows stronger sensitivity within the first Fresnel zone than the cosine taper kernel. In addition, the group arrival of 100 s Rayleigh waves is not located at the center of the time window, which leads to more oscillatory side bands in cosine-taper kernel. Finite frequency kernels accounting for the effects of measurement techniques require frequency domain convolutions, which is a time consuming procedure in kernel calculations. To speed up the kernel calculation speed without much loss in accuracy, we follow Zhou *et al.* (2004) to approximate the frequency domain convolution by a spacial multiplication. This approximation is adequate for the long windows used in our surface-wave measurements and the tapers have narrowly concentrated spectra.

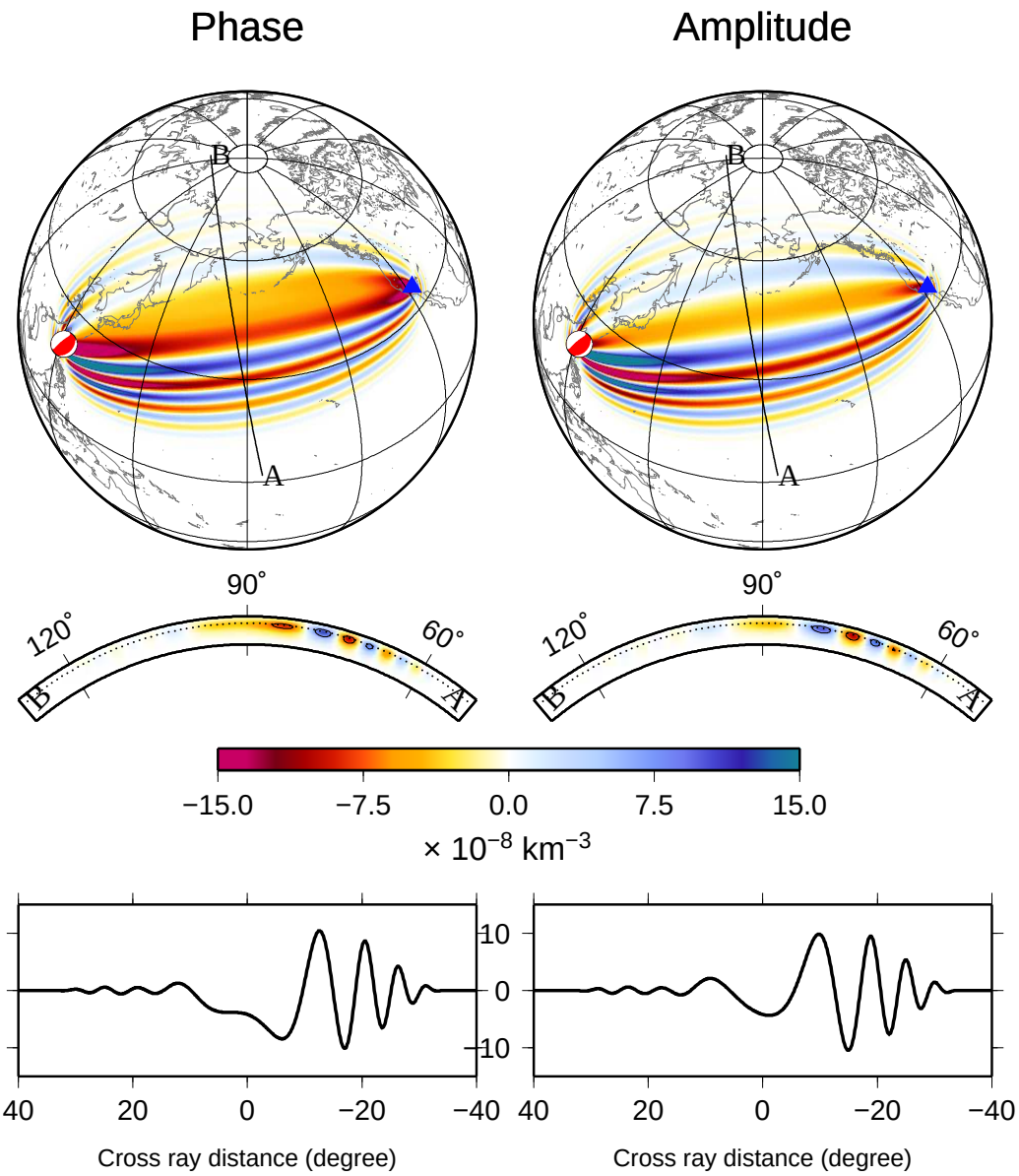

Figure 4.1: Three-dimensional sensitivity of 100-s Rayleigh wave phase and amplitude measurements to wave speed perturbations. Seismic source is a thrust event at 33 km, epicenter distance to the station GPO is $\Delta = 101^{\circ}$. Top: Map view of kernels at depth of 120 km. Middle: Depth cross-section of kernels half way between the source and receiver (AB). Bottom: Cross-section AB at depth of 120 km (dotted line). Note amplitude kernel is more oscillatory than phase kernel.

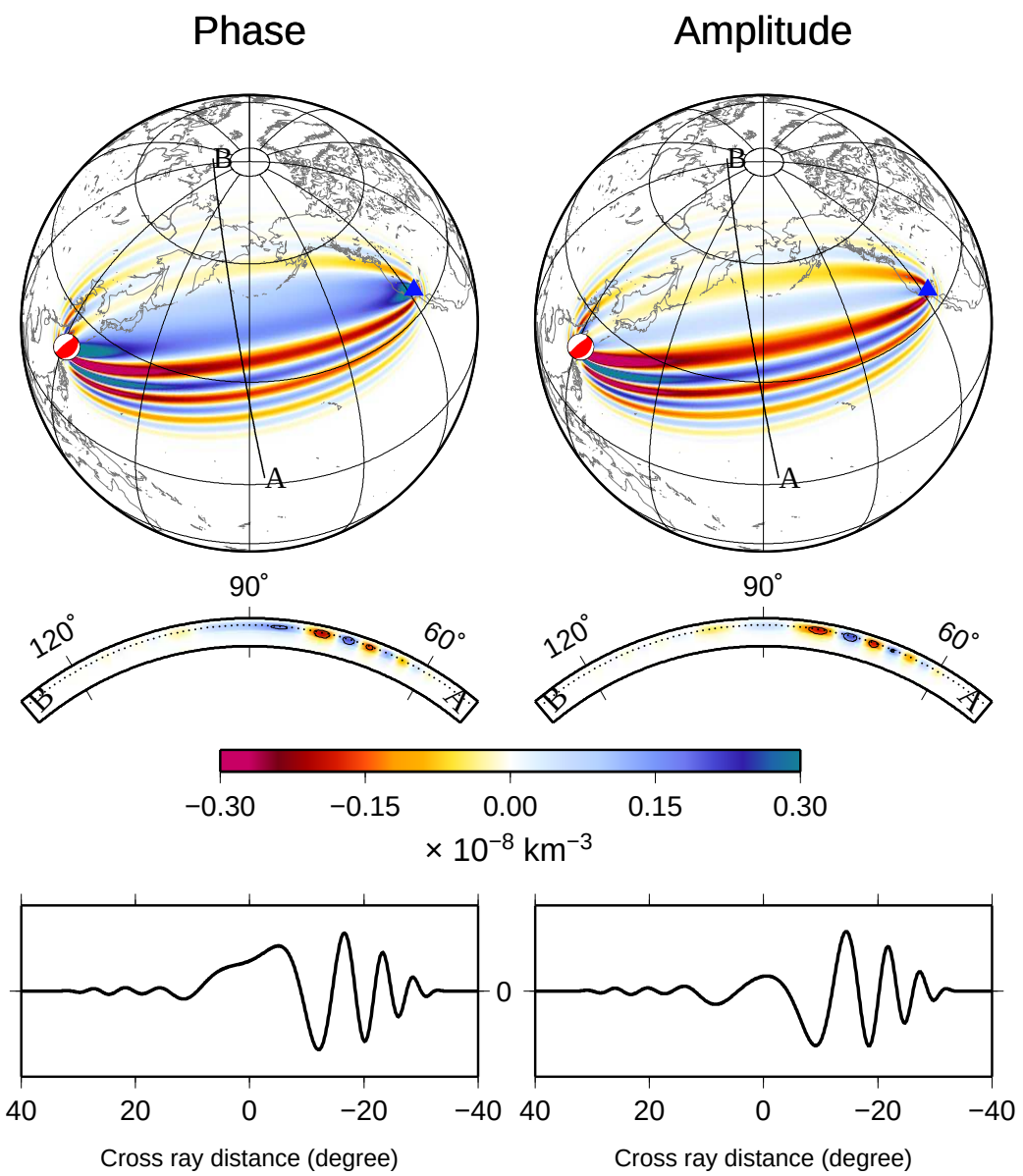

Figure 4.2: Three-dimensional sensitivity of 100-s Rayleigh wave phase and amplitude measurements to perturbations in anelasticity (Q^{-1}). Source and receiver are the same as in Fig. 4.1. Top: Map view of kernels at 120 km depth. Middle: Depth cross-section of kernels half way between source and receiver. Bottom: Center cross-section AB at depth of 120 km (dotted line). Note the scale of Q kernels is much smaller than the one for wave speed kernels.

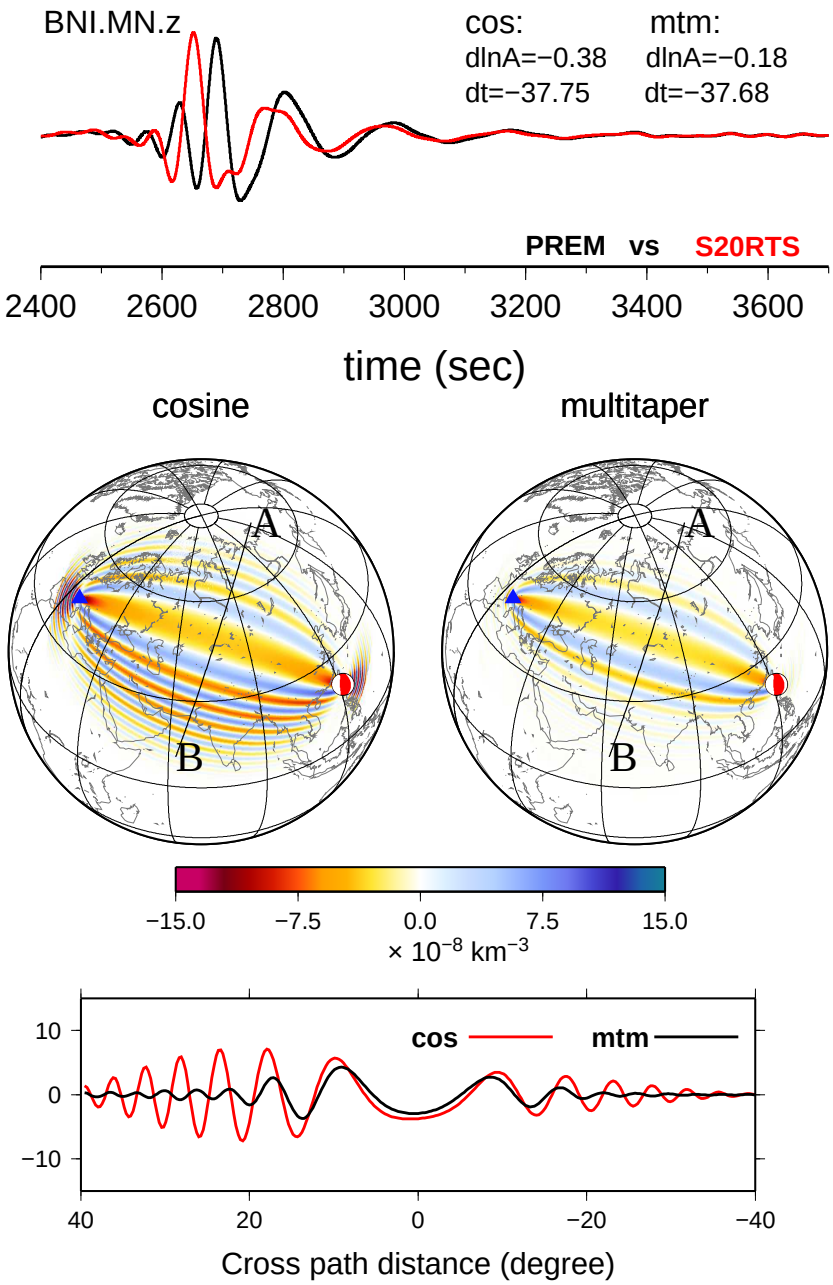

Figure 4.3: Example sensitivity of amplitudes to wave speed calculated for cosine taper measurements and multitaper measurements. The epicentral distance for this example is 92.2°. Top: Example seismogram in PREM (black) and S20RTS (red) are bandpass filtered between 5 and 20 mHz, amplitude and phase delays measurements using cosine taper and multitapter are indicated above the seismograms. Middle: map view of kernels at 100 km depth. Bottom: cross-section AB at depth of 100 km, red line for cosine taper and black for multitaper. Note multitaper kernels are less oscillatory than cosine-taper kernels.

4.4 Surface wave finite frequency effects

The focus of this study is to examine finite frequency effects of surface waves in a global 3-D wave speed model and a global 3-D anelasticity (Q) model. It is well known that when the length scale of anomalies is comparable to or less than the the wavelength of seismic waves, ray theory will break down and finite frequency effects need to be considered. We will investigate finite frequency effects in surface waves at periods between 50 s to 200 seconds for earth models with anomalies at currently resolvable length scales.

4.4.1 3-D earth models and wave propagation simulations

To evaluate finite frequency effects in 3-D wave speed and 3-D anelasticity (Q) model, we calculate and compare phase delays and amplitude perturbations in 3-D models based upon ray theory and finite frequency theory. In this section, we shall discuss the 3-D earth models and briefly review wave propagation simulations based upon Spectral Element Method (Komatitsch & Tromp, 1999, 2002a,b). In order to provide a good path coverage, 12 earthquakes and 801 stations are used in both theoretical calculations and numerical simulations.

Due to large discrepancies between existing 3-D global tomography Q models, we construct tomography-like 3-D Q models for our numerical experiments assuming existing tomography models are correct in order of magnitude. We first construct a reference 1-D Q model based upon an estimated geotherm of mantle. This geotherm is an approximation of average mantle temperature and is derived assuming half-space cooling of an adiabatic mantle using reasonable geothermal parameters (see Table 3.1). Assuming a thermal mechanism of anelasticity (Jackson & Anderson, 1970; Karato

Table 4.1: Mineralogical parameters used for constructing 1-D Q reference model.

Parameters	Values
Activation energy, E^*	470 KJ mol^{-1}
Activation volume, V^*	17 cm^3 mol^{-1}

(a) 3-D anelasticity (Q) model at 120 km

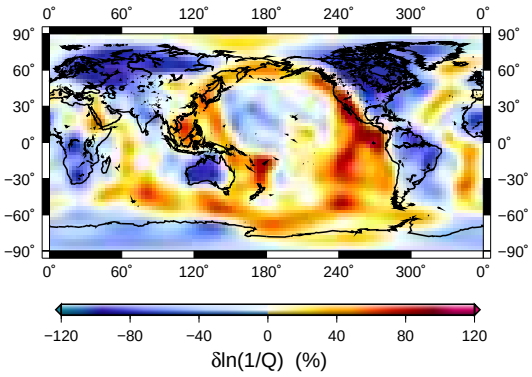

(b) 3D S-wave wavespeed model at 120 km

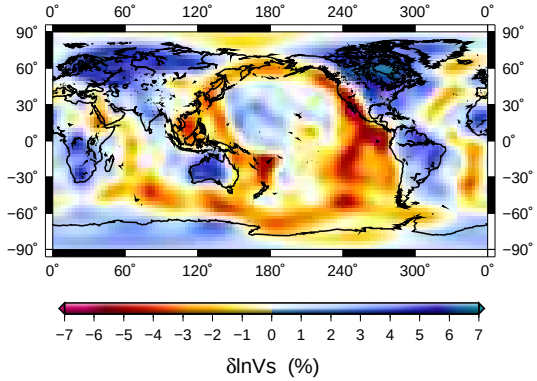

Figure 4.4: (a) Map view of 3-D wave speed model S20RTS (Ritsema & Van Heijst, 2000) at depth of 120 km. (b) Map view of 3-D Q model (Q3DM) at 120 km depth. This model is constructed from 1-D reference Q model and shear wave speed in S20RTS. Note wave speed model and Q model are highly correlated because we assume they both are thermally originated.

& Spetzler, 1990), we calculate 1-D reference Q model using the temperature profile

$$Q(T) = A \exp\left[\frac{\alpha(E^* + PV*)}{RT}\right]. \tag{4.16}$$

Where activation energy E^* and activation volume V^*, are the mineralogical parameters estimated from laboratory experiments of upper mantle minerals such as olivine (Table 4.1). The constant $A = 1.394$ is chosen to calibrate the reference Q model and make it close to PREM Q profile. The reference Q model, $\mathrm{Q1DM}$, has a higher-than-PREM Q values at crust and uppermost mantle, but close to PREM Q at deeper mantle. Unlike PREM, the reference Q model does not contain discontinuities through out upper mantle.

Based on a 3-D wave speed model S20RTS (Ritsema & Van Heijst, 2000) and the reference Q model, we construct a 3-D Q model assuming perturbations in wave speed and anelasticity are both

caused by temperature variations. We follow Ruan & Zhou (2010) and calculate temperature perturbations associated with shear wave speed perturbations in model S20RTS using the temperature partial derivative of shear wave speed (Karato, 1993; Ruan & Zhou, 2010). As shown in eq. 2.8 (Chap. 2), the temperature partial derivative $\partial \ln V/\partial T$ is dependent on Q, therefore an iterative approach was adopted to construct 3-D temperature which will be further converted to 3-D Q model. Wave speed model S20RTS and associated 3-D Q model are shown in Fig. 4.4 at a depth of 120 km. The same Q model has been used to quantify the effects of anelastic perturbations on surface wave travel times (Ruan & Zhou, 2010) and amplitudes (Ruan & Zhou, 2012). Based upon 3-D wave speed and Q models, we make predictions of phase delays and amplitude perturbations using finite frequency kernels.

In ray theory (eqs. (4.12 – 4.15)), phase delays and amplitude perturbations are associated with phase velocity perturbations and their second spatial derivative (roughness) in 3-D wave speed model and perturbations in Q^{-1} and their roughness in 3-D Q model. Following the approach in Ruan & Zhou (2012), we calculate phase velocity perturbations caused by 3-D wave speed and surface wave Q^{-1}_{Love} or $Q^{-1}_{Rayleigh}$ perturbations caused by 3-D Q perturbations at periods of 50 s, 100 s, and 200 s. We discretize the 3-D wave speed model and 3-D Q model to 16,200 1-D local radial models on $2^\circ \times 2^\circ$ cells and solving radial equation in these 1-D local wave speed models for phase velocity and Love- and Rayleigh-wave Q^{-1} values, respectively. Phase velocity perturbations due to 3-D wave speed structures are calculated base upon model I – PREM and model II – S20RTS (Table 3.2). We decomposed the phase velocity perturbations using the real spherical harmonics (Dahlen & Tromp, 1998, Appendix B),

$$\psi(\theta,\phi) = \sum_{l=0}^{\infty} \left[a_{l0} X_{l0} + \sqrt{2} \sum_{m=1}^{l} X_{lm} (a_{lm} \cos m\phi + b_{lm} \sin m\phi) \right], \tag{4.17}$$

where the $\psi(\theta,\phi)$ is perturbation field of phase velocity or Q^{-1} and a_{lm} and b_{lm} are the spherical

harmonics coefficients. The second spatial derivative (roughness) of phase velocity perturbations ($\nabla^2\psi$) are calculated using methods described in Ruan & Zhou (2012, Appendix A). Example phase velocity perturbations and their roughness for 100 s Rayleigh waves are shown in Fig. 4.5. The power spectra of phase velocity perturbations and their roughness are calculated using the spherical harmonics coefficients,

$$P_l = \frac{1}{2l+1}\left[a_{l0}^2 + \sum_{m=1}^{l}(a_{lm}^2 + b_{lm}^2)\right], \tag{4.18}$$

where l is the spherical harmonics degree. Examples of power spectra for 100 s Rayleigh waves are plotted in Fig. 4.5 as well. The power spectra of phase velocity perturbations show that anomalies are dominated by low harmonic degree structures ($l < 10$), while the spectra of its roughness show that low harmonic degree structures ($l < 5$) are less significant and a constant power band ($5 < l \leq 20$) indicates shorter wavelength anomalies are dominant. Based upon the phase velocity perturbations and their roughness maps, we calculate phase delays and amplitude perturbations caused by 3-D wave speed using eqs. (4.12) and (4.13). Unlike the roughness map shown in the examples, in practice (eq. 4.13), we only need to calculate the second spatial derivative in cross-ray direction (Ruan & Zhou, 2012).

Similarly, Love- and Rayleigh-wave Q^{-1} perturbations caused by 3-D anelasticity are calculated for model III – 1-D reference Q with PREM wave speed and model IV – 3-D Q with PREM wave speed (Table 3.2). In Fig. 4.6, we show examples of Q^{-1} perturbations and its roughness map for 100 s Rayleigh waves, as well as their power spectra. Given that 3-D wave speed model and 3-D Q model in this study is highly correlated, it's not surprising that perturbations of Rayleigh-wave Q^{-1} is also dominated by long-wavelength structures ($l < 5$), and roughness map is dominated by short-wavelength structures ($5 < l \leq 20$). We calculate phase delays and amplitude perturbations caused by 3-D Q using eqs. (4.14) and (4.15).

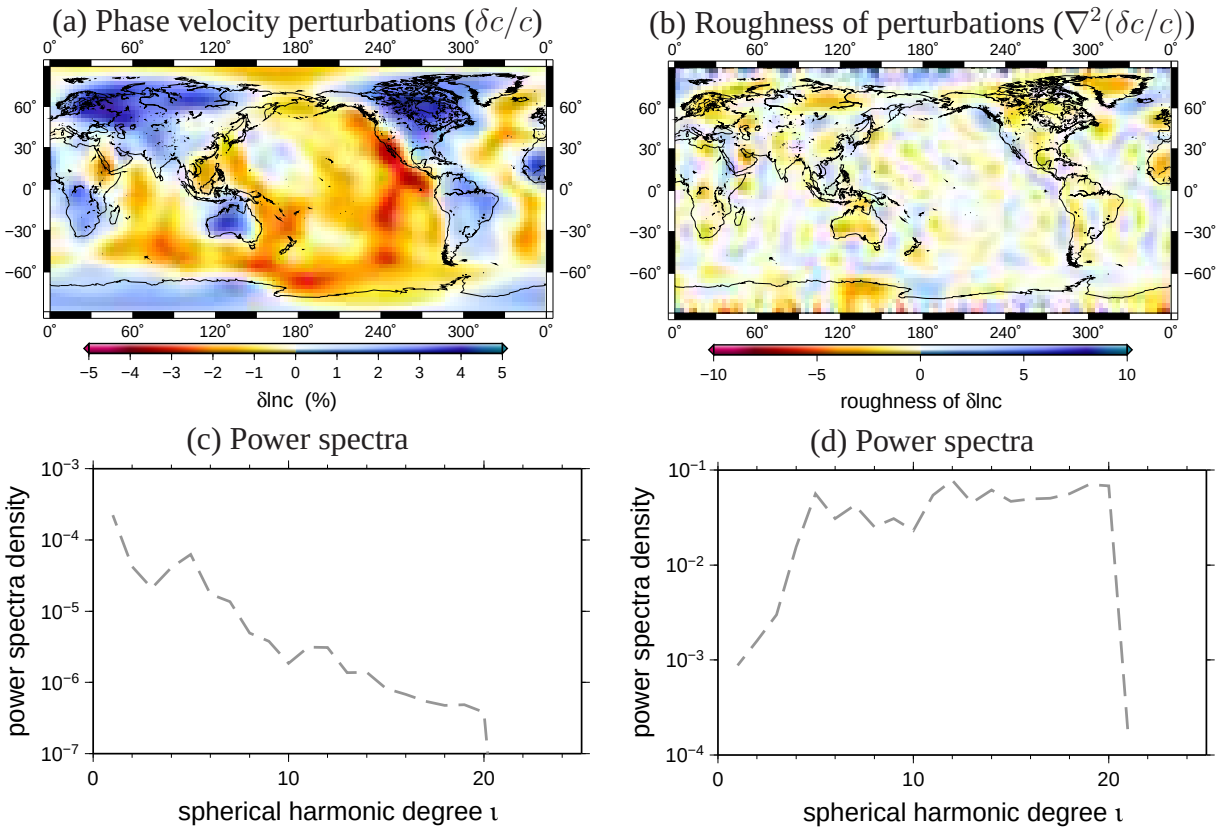

Figure 4.5: (a) Perturbations of 100-s Rayleigh wave phase velocity caused by 3-D wave speed structures (S20RTS). (b) Second spatial derivative (roughness) of phase velocity perturbations shown in (a). (c) and (d) are the associated power spectra of phase velocity perturbations and its roughness. Note long-wavelength anomalies dominate phase velocity perturbations while shorter-wavelength anomalies at broad arrange ($5 < l \leq 20$) become important in roughness model.

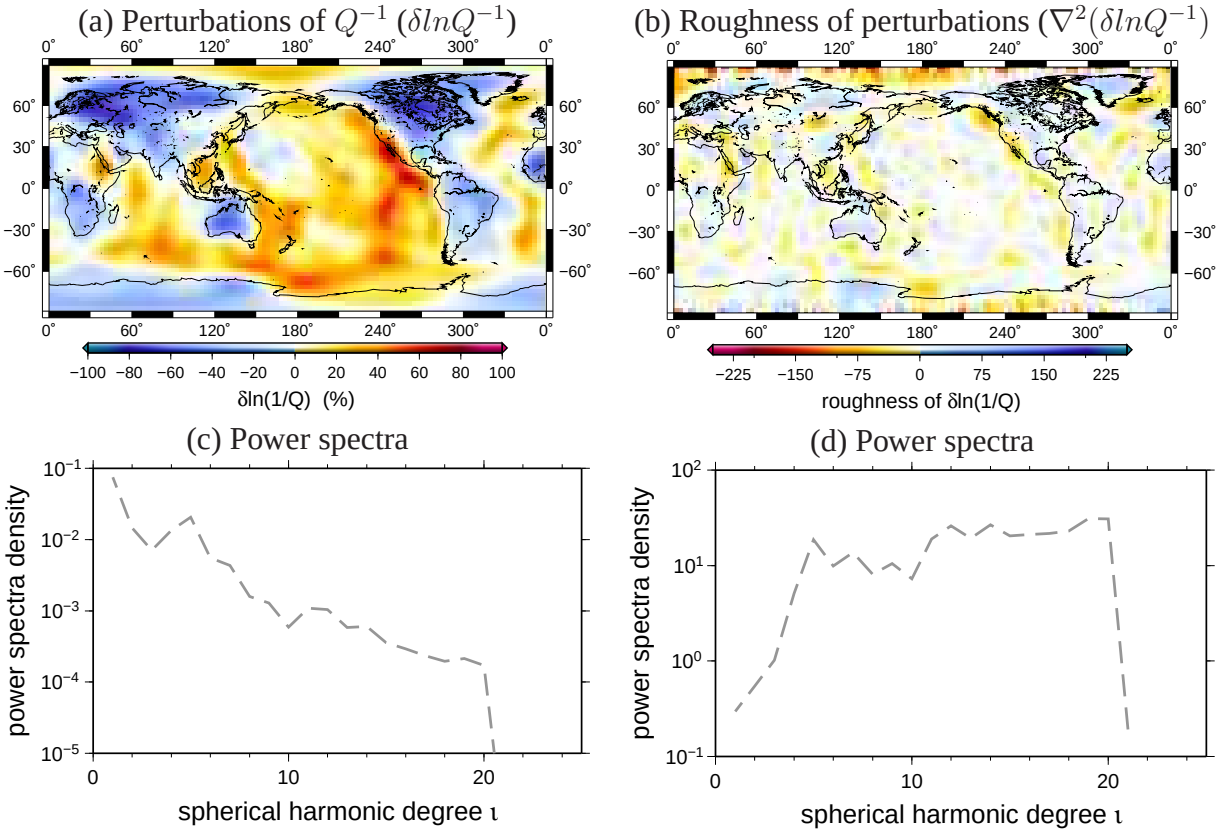

Figure 4.6: (a) Perturbations of 100-s Rayleigh wave Q^{-1} caused by 3-D Q structures (Q3DM). (b) Second spatial derivative (roughness) of Q^{-1} perturbations shown in (a). (c) and (d) are the associated power spectra of Q^{-1} perturbations and its roughness. Similar to the power density properties shown in Fig. 4.5, long-wavelength anomalies dominate Q^{-1} perturbations while shorter-wavelength anomalies at broad arrange ($5 < l \leq 20$) become important in roughness model.

To investigate finite frequency effects as well as limitation of linear perturbation theory, we compare theoretical predictions with measurements based upon synthetic seismograms generated using a Spectra Element Method (Komatitsch & Tromp, 1999, 2002a,b). In the case of investigating finite frequency effects of 3-D wave speed, we measure phase delays and amplitude perturbations between synthetic seismograms calculated in model I and II, which has 1-D wave speed and 3-D wave speed structures, respectively (Table 3.2). In the case of examining finite frequency effects due to 3-D anelasticity, we measure the difference in phases and amplitudes from the synthetic seismogram calculated in model III and IV, which has 1-D reference Q and 3-D Q structures, respectively (Table 3.2). To ensure good spectra estimates, we adopt a multi-taper method (MTM) (Laske & Masters, 1996; Zhou *et al.*, 2004) in the measurements of surface-wave phase delays and amplitude perturbations. The advantage of using multi-taper method lies in that the prolate spheroidal eigentapers can reduce bias in spectral estimations because of their narrowly concentrated spectra. In addition, this method can provide an estimation of measurement errors by least-square fitting of measurements from each taper. In this Chapter, we use five 2.5-π tapers to measure surface-wave phase delays and amplitude perturbations at wave period from 50 s to 200 s. The hand-picked time window for measurements are chosen to include the group arrivals of surface wave at measuring period, but exclude higher-mode surface waves when possible. The window length is predetermined to balance spectra resolution and higher-mode surface wave contamination (Ruan & Zhou, 2012). The same time windows will be used in both measurements and kernel predictions.

4.4.2 Finite frequency effects in 3-D elastic model

We compare surface-wave phase delays and amplitude perturbations calculated in the framework of ray theory and finite frequency theory to examine finite frequency effects in 3-D wave speed and 3-D anelasticity (Q), respectively. Differences between ray-theoretical predictions and kernel predictions indicate finite frequency effects. In Fig. 4.7, kernel predictions of Rayleigh-wave amplitude per-

turbations are compared with ray-theoretical predictions in the 3-D wave speed model S20RTS. We exclude earthquake-station pairs located near the nodal direction of source radiation (less than 40% of maximum radiation), which leaves approximately 2000–4000 pairs in each plot. The scatterplot for 50 s Rayleigh waves show less difference between ray-theoretical and kernel predictions than that for 200 s Rayleigh waves, indicating finite frequency effects are stronger in 200 s than in 50 s waves. This frequency dependence is expected because ray theory is a infinite frequency approximation. Similar ray-versus-kernel comparisons for Rayleigh-wave phase delays are plotted in Fig. 4.8 at wave periods of 50 s, 100 s, and 200 s. Larger discrepancies in 200 s than in 50 s Rayleigh waves demonstrate finite frequency effects in phase delays are also stronger in long-period waves than in short-period waves.

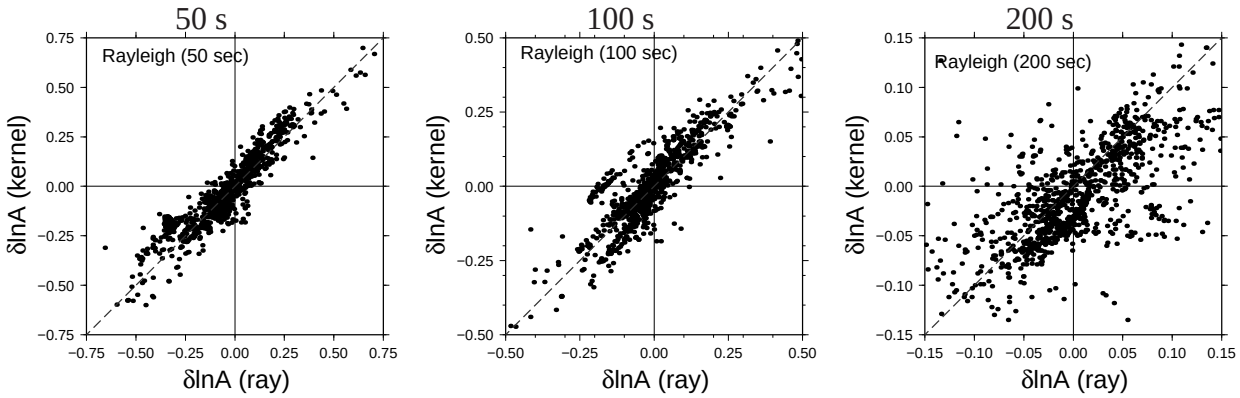

Figure 4.7: Comparison between finite-frequency kernel predictions and ray-theoretical predictions of Rayleigh-wave amplitude perturbations caused by 3-D wave speed (S20RTS). Comparisons are shown at wave periods of 50 s, 100 s, and 200 s. A more scattered pattern at 200 s indicates stronger finite frequency effects on long-period Rayleigh waves.

It is noteworthy that finite frequency effects in amplitudes (Fig. 4.7) are stronger than that in phase delays (Fig. 4.8). This is probably because amplitude kernels are more oscillatory than phase kernels (Fig. 4.1) reflecting the fact that amplitude are sensitive to the geometry of the anomalies. In the frame work of ray theory, predictions of amplitude perturbations in a 3-D wave speed model are dependent on the second spatial derivatives (roughness) of phase velocity perturbations (eq. 4.13). As shown in Fig. 4.5, roughness of phase velocity perturbations contain more finer scale anomalies than phase velocity perturbations. For anomalies at length scales smaller than wavelength, ray theory is

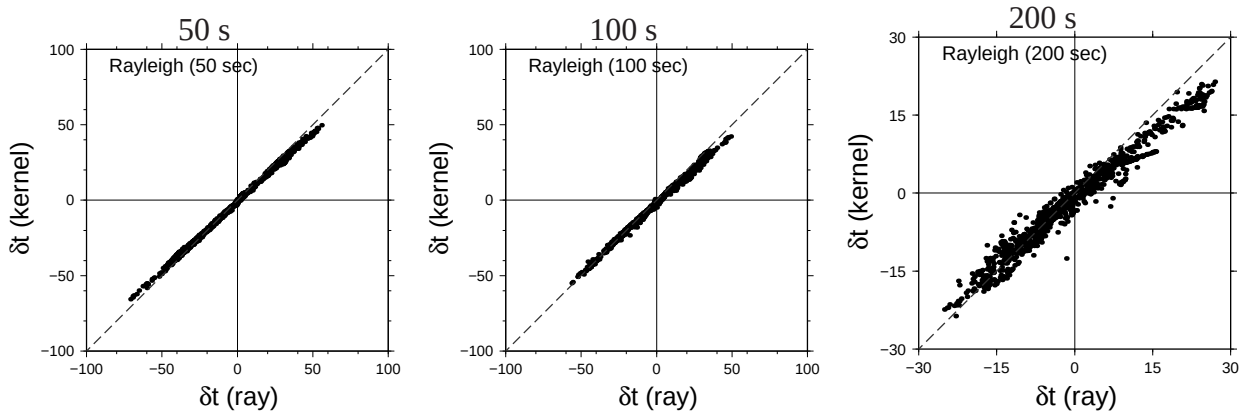

Figure 4.8: Comparison between finite-frequency kernel predictions and ray-theoretical predictions of Rayleigh-wave phase delays caused by 3-D wave speed (S20RTS) . Finite frequency effects are frequency dependent. In general, finite frequency effects are less significant than those in amplitudes (Fig. 4.7).

more likely to break down, and stronger finite frequency effects in amplitudes than in phase delays are expected.

It's worthy of emphasizing that in a fairly smooth model such as S20RTS, small-scale structures are often damped out due to resolution limits of ray theory, however, strong finite frequency effects at long-period surface waves are still observed. When the size of mantle heterogeneities becomes comparable to or smaller than seismic wavelength, finite frequency effects become much stronger than what have been shown in this study (Zhou, 2010).

4.4.3 Finite frequency effects in 3-D anelastic model

In 3-D anelastic (Q) model, we compare ray-theoretical predictions and finite-frequency kernel predictions of amplitude perturbations and phase delays as we have done in section 4.4.2 for 3-D wave speed model. Q kernels are calculated for a 1-D reference model with a radial Q structure. Ray-vs-kernel comparisons are shown as a function of wave period in Fig. 4.9. Large discrepancies between calculations based on ray theory and finite frequency theory for 200 s Rayleigh waves show finite

frequency effects in 200 s waves are more significant than in 100 s and 50 s waves. Finite frequency effects on amplitudes shown in 3-D Q model (Fig. 4.9) are relatively weaker than those shown in 3-D wave speed model (Fig. 4.7), especially at 50 s and 100 s. This is probably due to that at short period, the dominantly effects on amplitude caused by 3-D Q are attenuation (Ruan & Zhou, 2012). In ray theory limit, amplitude attenuation is dependent upon perturbations in Q^{-1} which are dominated by low harmonic degree structures, therefore weak finite frequency effects is expected. While in long-period surface waves, attenuation become less significant and anelastic focusing becomes the dominant effect. Anelastic focusing is dependent upon roughness (second spatial derivatives) of perturbations in Q^{-1} which contain structures at higher harmonic degrees. Compared with perturbations in $\delta Q^{-1}/Q^{-1}$, the roughness of perturbations in $\delta Q^{-1}/Q^{-1}$ contains more small scale anomalies as shown in their power spectra (Fig. 4.6), therefore stronger finite frequency is expected. Therefore in 3-D Q model, when attenuation effects are dominant finite frequency effects are relatively weak; when anelastic focusing effects are dominant finite frequency effects become stronger. This explains the less-pronounced finite frequency effects in 50 s and 100 s Rayleigh waves than in 200 s Rayleigh waves, in addition to the finite frequency effects of attenuation.

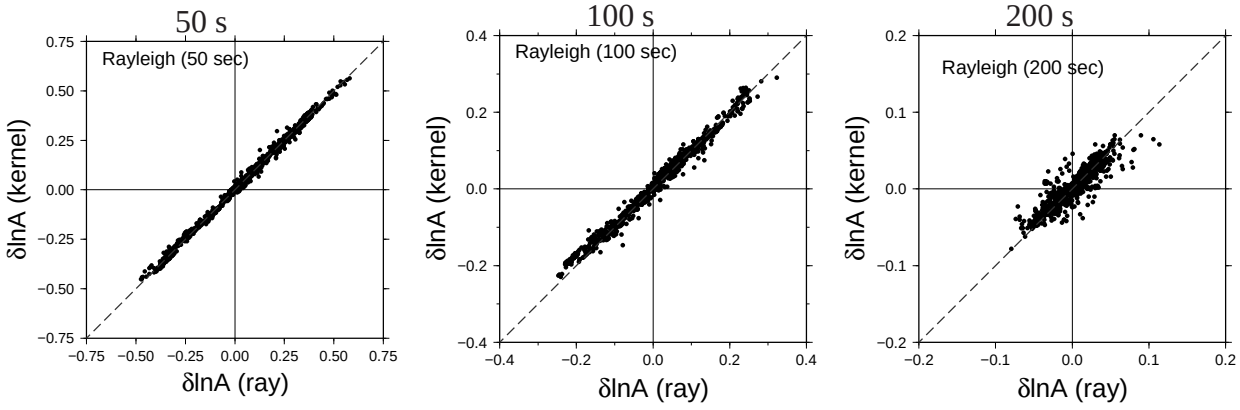

Figure 4.9: Comparison between finite-frequency kernel predictions and ray-theoretical predictions of Rayleigh-wave amplitude perturbations caused by 3-D Q (Q3DM). Finite frequency effects are stronger at long period than in short period (< 100 s).

Fig. 4.10 shows comparisons between ray-theoretical and kernel predictions for Rayleigh-wave

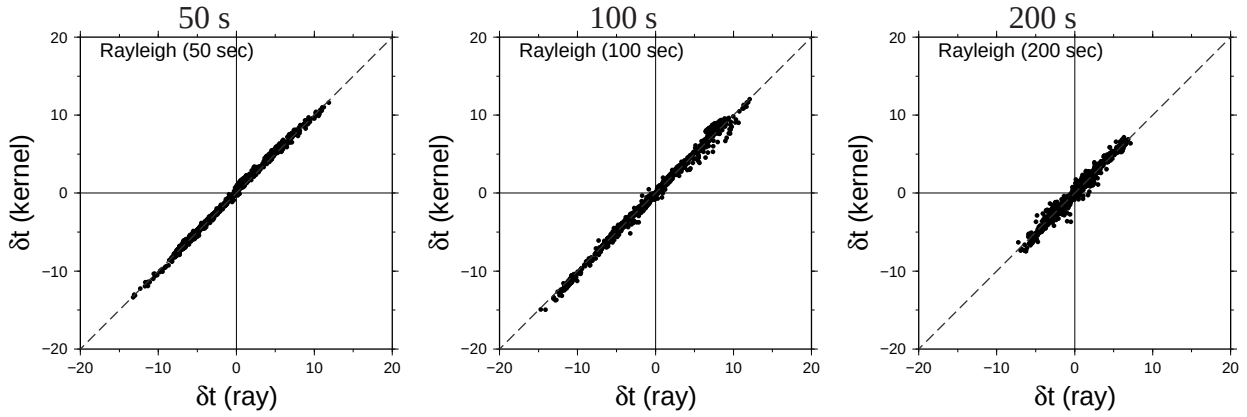

Figure 4.10: Comparison between finite-frequency kernel predictions and ray-theoretical predictions of Rayleigh-wave phase delays caused by 3-D Q. Finite frequency effects are weaker than they are in 3-D wave speed models (Fig. 4.8).

phase delays caused by 3-D Q structures as a function of wave period. Finite frequency effects in anelastic dispersion also vary with wave periods and become stronger at longer period. Compared with finite frequency effects on phase delays in 3-D wave speed model (Fig. 4.8), the effects are much weaker in the 3-D Q model. This is because that phase delays caused by 3-D anelastic dispersion are mainly due to perturbations in $\delta Q^{-1}/Q^{-1}$ rather than the second derivative of the perturbations (Zhou, 2009), therefore, in the presence of large scale Q^{-1} anomalies in 3-D Q model (Fig. 4.6), phase delays can be relatively well predicted by ray theory. It is worth to emphasize again that ray theory breaks down when anomalies are small compare to wavelength. For example, Baig *et al.* (2003) argued that ray theory will no longer be valid when anomalies are smaller than half of the maximum Fresnel Zone width along the ray path.

4.4.4 Comparisons with SEM measurements

In Fig. 4.11, we compare ray theoretical predictions with SEM measurements for Rayleigh-wave amplitude perturbations at period of 50 s, 100 s, and 200 s (left column). Each scatterplot shows ray-theoretical predictions of amplitude perturbations in a 3-D elastic (wave speed) model against mea-

surements based on synthetic seismograms generated in SEM simulations. For each event, paths with source radiations less than 40% of the maximum source radiation have been excluded. In addition, when phase delay measurements show large error bars, then corresponding amplitudes measurements will also be excluded. This left 1000 to 1500 source-receiver pairs in each scatterplot for four events used in the comparisons. Fig. 4.11 shows that amplitude perturbations calculated using ray theory in general agree reasonably well with SEM measurements except at a period of 200 s. Similar comparison between kernel predictions and SEM measurements (right column) agree well to each other at all periods. This is expected because finite frequency effects in 200 s waves are stronger than in short-period waves (Fig. 4.7). For 3-D Q model, comparison between theoretical predictions and SEM measurements are shown in Fig. 4.12. It's not surprising that both ray theory and finite frequency kernels can predict amplitude perturbations measured from synthetic seismograms because finite frequency effects are not strong in amplitudes in 3-D Q model (Fig. 4.9). In conclusion, ray theory and finite frequency theory both can predict amplitude perturbations reasonably well when amplitudes are mainly caused by attenuation, while finite frequency theory provides more accurate estimates when focusing effects are the main cause of amplitude perturbations. Wave speed and Q models used in this experiments are very smooth, when imaging mantle heterogeneities at length scale smaller than seismic wavelength, finite frequency effects will become more pronounced.

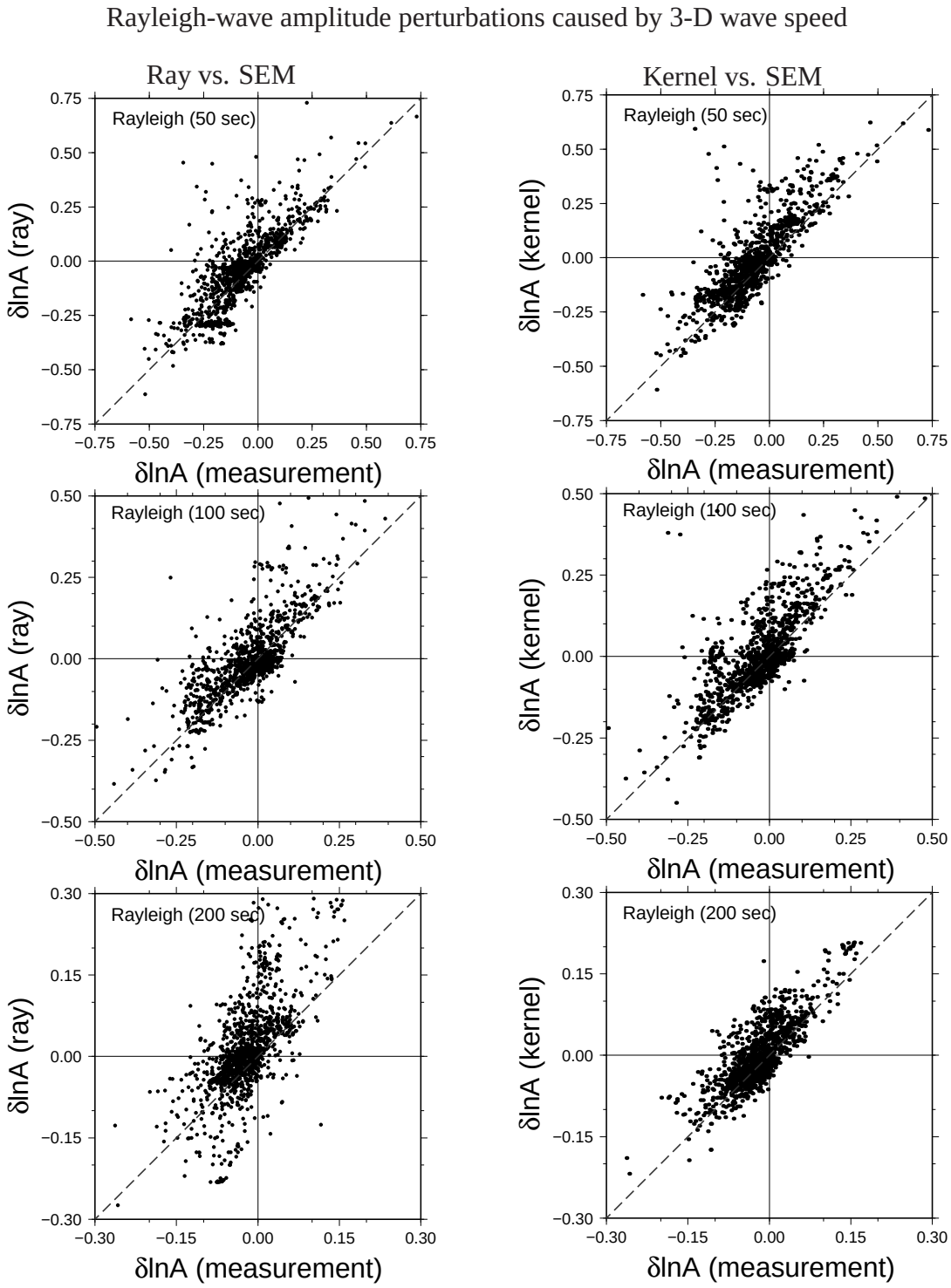

Figure 4.11: Left: comparison between ray-theoretical predictions and SEM measurements of Rayleigh-wave amplitude perturbations in 3-D wave speed model at wave periods of 50 s, 100 s, and 200 s. Right: same as left but between kernel predictions and SEM measurements. At 200 s, kernel predictions agree well with SEM measurements but ray-theory can hardly predict the amplitude perturbations.

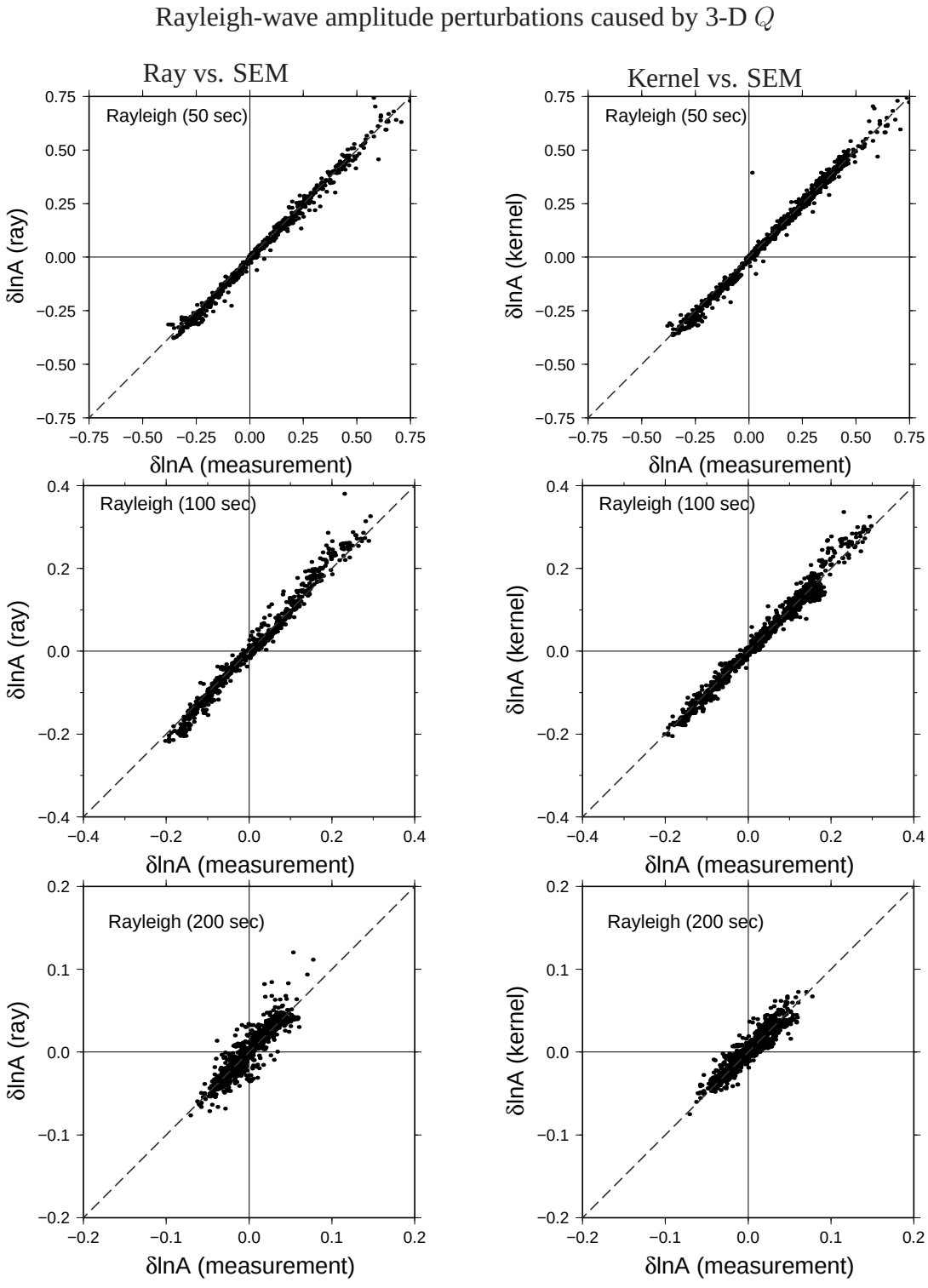

Figure 4.12: Same as Fig. 4.11 but for 3-D Q models.

4.5 Effects of source local structures

In Fig. 4.1 and 4.2, we have taken into account the effects of attenuation and focusing in calculation of finite frequency kernels but seismic amplitudes are also sensitive to source focal mechanisms. In the presence of 3-D structures, local perturbations at sources will lead to changes in excitation of seismic amplitudes. In this section, we will investigate the effects of source local structures. It has been suggested that the effects of local structure at receivers are negligible (e.g., Ferreira & Woodhouse, 2007), and therefore will not be considered in this study. Near the maximum direction of radiation pattern, amplitude variations due to different source local structures is relative small, while when a station is near the nodal direction of source radiation, a slight variation in radiation pattern may result in large variations in amplitudes. We have excluded stations located in directions where radiation is less than 40% of the maximum. We correct effects of source local perturbations by replacing the source term in finite frequency kernels calculated in reference model with that calculated in a 1-D local model at the source. Comparison between kernels with and without source correction are shown in Fig. 4.13, the differences are mainly in the side bands of kernels. To evaluate possible source effects in this study, we recalculate kernel predictions with source corrections and an example is shown in Fig. 4.14. This is an event with considerable variations in amplitudes and phase delays after corrections of source local structures in sensitivity kernels. In this example, phase delays caused by source local perturbations does not exceed 0.5 s in 50 s and 200 s Rayleigh waves. However, amplitude variations can be as large as 8% in 50 s Rayleigh waves at some stations and less than 1% in 200 s Rayleigh waves. In general, source local perturbations may be important for short-period surface wave's amplitudes but their effects are limited in long-period surface wave's amplitudes. In surface wave tomography practice, most earthquakes occurred along subduction zones where local earth models may be very different from reference model, therefore the effects of source local structure will be relatively strong and probably need to be taken into account. One possible approach to reduce such effects in global tomography study is to calculate source term in local models in an iterative way, this need to be taken

into account in future studies.

Amplitude perturbations in 3-D wave speed model are in general positively correlated with phase delays. For example, slow anomalies in earth model cause travel time delays and increase wave amplitudes through focusing. Fig. 4.15 shows examples of correlations between phase delays and amplitude perturbations measurements and corresponding comparisons between amplitude perturbations calculated using finite frequency kernels and measured using SEM seismograms. In this study, events showing strong negative correlation between phase and amplitude have been excluded. The negative correlation may be due to strong non-linear effects near the source. This also indicates that far-field approximation used in the calculation of amplitude kernels may not be adequate as a general positive correction would be expected (Liu & Zhou, 2008).

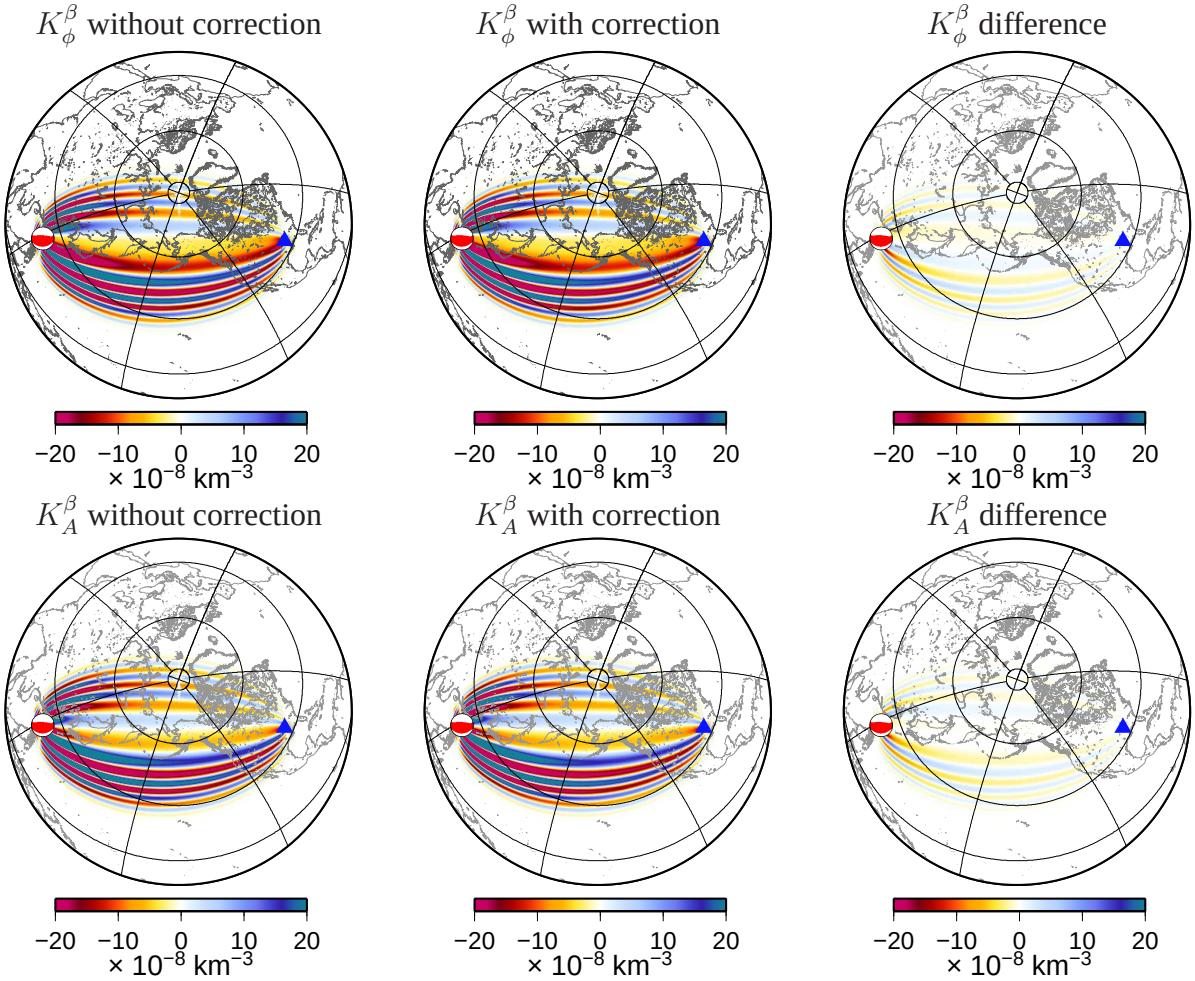

Figure 4.13: Difference in finite frequency kernels calculated with and without corrections of source local perturbations. In this example, azimuth of station OXF is in the direction in which source radiation is 40% of the maximum radiation. Note the difference are mainly located in the oscillatory side bands.

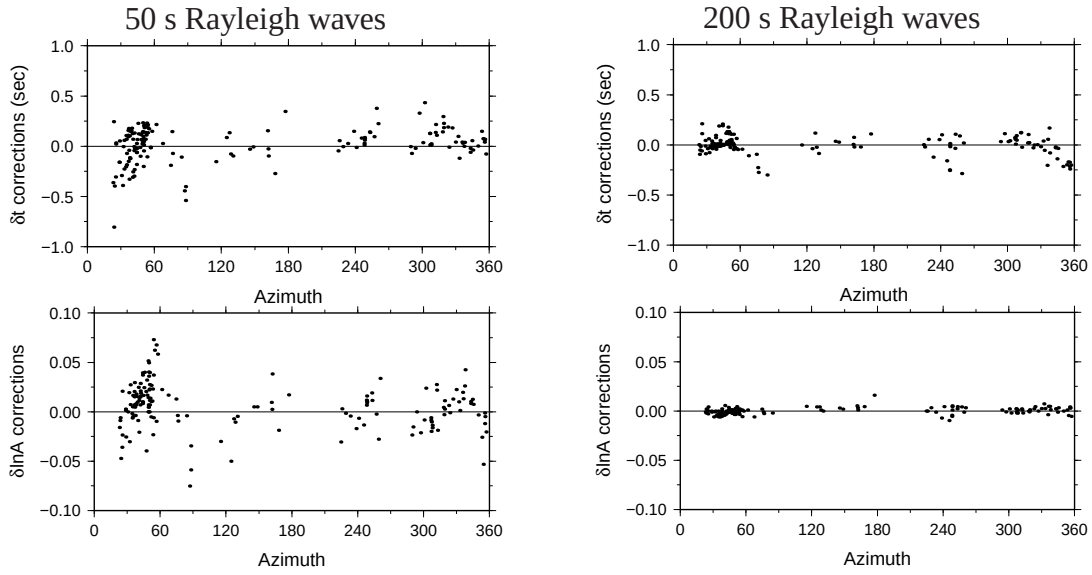

Figure 4.14: Effects of source local structures on kernel predictions of amplitude perturbations and phase delays. Difference between kernel predictions with and without consideration of source local structures are shown for 50 s and 200 s Rayleigh waves.

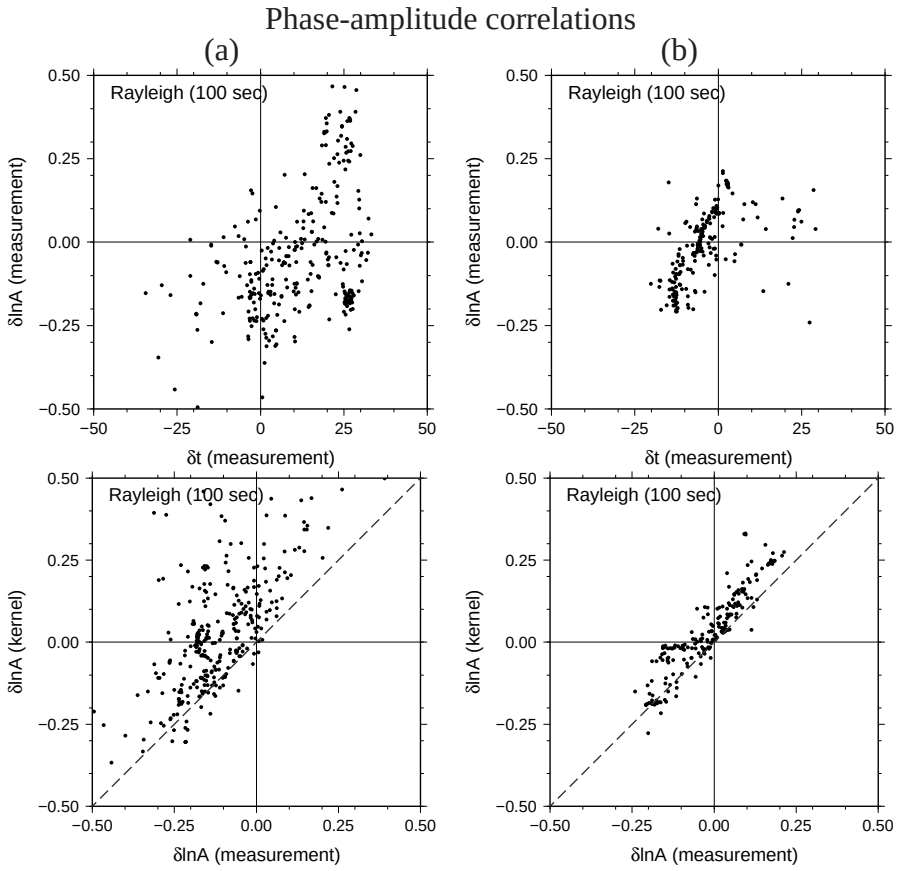

Figure 4.15: Examples correlation between phase delays and amplitude perturbations measurements for two different events (top). Bottom: Comparison between kernel predictions and SEM measurements of amplitudes. Strong negative correlation between phase and amplitude in (a) indicate strong non-linear effects.

4.6 Discussion and Conclusion

We investigate finite frequency effects in 3-D wave speed model and 3-D Q models by comparing theoretical predictions of surface-wave phase delays and amplitudes with those measured from SEM simulations at wave periods from 50 s to 200 s. Assuming a thermal mechanism of lateral heterogeneities in the mantle, the 3-D Q model is constructed from a tomography wave speed model S20RTS. Ray-theoretical phase delays and amplitude perturbations are calculated and compared with kernel predictions. The comparison shows that (1) finite frequency effects are stronger in long-period surface waves than in short-period waves; (2) finite frequency effects are stronger in amplitudes than in phase delays, especially at long periods.

We compare theoretical predictions with "ground-truth" measurements from SEM simulations. In 3-D wave speed model, ray-theoretical and kernel predictions of amplitude perturbations in short period waves ($<$ 100 s) agree reasonably well with SEM measurements, but in long-period surface waves ($\sim$ 200 s) sensitivity kernels predicted amplitude perturbations better than ray theory. For 3-D Q models, amplitudes calculated based on ray theory and finite frequency theory both agree well with measured amplitudes. Source local structures in general have limited effects on finite frequency kernel predictions of amplitude, especially at long periods. When phase delays and amplitudes show strong negative correlations, nonlinear effects can be significant in surface-wave amplitudes.

Bibliography

Baig, A. M., Dahlen, F. A., & Hung., S.-H., 2003. Traveltimes of waves in three-dimensional random media, *Geophys. J. Int.*, **153**, 467-482.

Dahlen, F. A. & Tromp, J., 1998. *Theoretical Global Seismology*, Princeton University Press, Princeton, New Jersey.

Dahlen, F. A. & Zhou, Y., 2006. Surface-wave group-delay and attenuation kernels, *Geophys. J. Int.*, , **165**, 545–554.

Dahlen, F. A., Hung, S.-H. & Nolet, G., 2000. Frèchet kernels for finite frequency travel times – I. Theory, *Geophys. J. Int.*, textbf141, 157-174.

Dalton, C., Ekström, G. & Dziewoński, A. M., 2008. The global attenuation structure of the upper mantle, *J. geophys. Res.*, **113**, B09303, doi:10.1029/2007JB005429.

Dziewonski, A. M. & Anderson, D. L., 1981. Preliminary reference Earth Model, *Phys. Earth planet. Inter.*, **25**, 297-356.

Ferreira, A. M. G. & Woodhouse, J. H., 2007. Source, path and receiver effects on seismic surface waves. *Geophys. J. Int.*, **168**, 109-132.

Grand, S. P., 1987. Tomographic inversion for shear velocity beneath the North American plate. *J. geophys. Res.*, **92**, 14,065-14,090.

Gung, Y. & Romanowicz, B., 2004. Q tomography of the upper mantle using three-component long-period waveforms, *Geophys. J. Int.*, **157**, 813-830.

Jackson, D. D. & Anderson, D. L, 1970. Physical Mechanisms of Seismic-Wave Attenuation, *Rev. Geophys.*, **8**, issue 1, 1-63.

Karato, Shun-ichiro, 1993. Importance of anelastic in the interpretation of seismic tomography, *Geophys. Res. Lett.*, **20**, NO. 15, 1623-1626.

Karato, S. & Spetzler., H. A., 1990. Defect microdynamics in mineral and solid-state mechanisms of seismic wave attenuation and velocity dispersion in the mantle, *Rev. Geophys.*, **28**, 399-421.

Komatitsch, D. & Tromp, J., 1999. Introduction to the spectral-element method for 3-D seismic wave propagation, *Geophys. J. Int.*, **139**, 806-822.

Komatitsch, D. & Tromp, J., 2002. Spectral-element simulations of global seismic wave propagation—I. Validation, *Geophys. J. Int.,* **149**, 390-412.

Komatitsch, D. & Tromp, J., 2002. Spectral-element simulations of global seismic wave propagation—II. Three-dimensional models, oceans, rotation and self-gravitation, *Geophys. J. Int.*, **150**, 303-318

Laske, G. & Master, G., 1996. Constraints on global phase velocity maps from long-period polarization data, *J. geophys. Res.,* **101**, NO. B7, 16,059-16,075.

Liu, K. & Zhou, Y., 2008. Near-Field Surface-wave Sensitivity Kernels. *Eos trans.* AGU, 89(53), Fall Meet. Suppl., Abstract DI21A-1736.

Liu, Q., & Tromp, J., 2008. Finite-frequency Sensitivity Kernels for Global Seismic Wave Propagation based upon Adjoint Methods, *Geophys. J. Int.,* **174**, 265-286.

Marquering, H., Nolet, G. & Dahlen, F. A., 1998. Three-dimensional waveform sensitivity kernels, *Geophys. J. Int.,* **132**, 521-534.

Master, G., Johnson, S., Laske, G., & Bolton, H., 1996. A shear-velocity model of the mantle, *Phil. Trans. R. Soc. Lond.* A, **354**, 1385-1411.

Ritsema, J. & Van Heijst, H. J., 2000. Seismic imaging of structural heterogeneity in Earth's mantle: Evidence for large-scale mantle flow, *Science Progress*, **83**, 243-259.

Ruan, Y. and Zhou Y. 2012, The effects of 3-D anelasticity (Q) structure on surface wave amplitudes, *Geophys. J. Int.,* **189**, 967-983.

Ruan, Y. and Zhou Y. 2010, The effects of 3-D anelasticity (Q) structure on surface wave phase delays, *Geophys. J. Int.,* **181**, 479-492.

Su, W.-J., Woodward, R. L., and Dziewonski, A. M., 1994. Degree 12 model of shear velocity heterogeneity in the mantle. *J. geophys. Res.,* **99**, 6945-6980.

Tape, C., Liu, Q., Maggi, A. & Tromp, J., 2009. Adjoint tomography of the southern California crust, *science* **325**, 988-992.

Tape, C., Liu, Q., Maggi, A., & Tromp, J., 2010, Seismic tomography of the southern California crust based on spectral-element and adjoint methods, *Geophys. J. Int.,* **180**, 433-462.

Tian, Y., Sigloch, K., & Nolet, G., 2009. Multiple-frequency SH-wave tomography of the Western U.S. upper mantle. *Geophys. J. Int.,* **178**, 1384-1402.

Tian, Y., Zhou, Y., Sigloch, K., Nolet, G. & Laske, G., 2011. Structure of North American mantle constrained by simultaneous inversion of multiple-frequency SH, SS, and Love waves, *J. geophys. Res.,* **116**, B02307, doi:10.1029/2010JB007704.

Tromp, J., Tape, C., & Liu, Q., 2005. Seismic Tomography, Adjoint Methods, Time Reversal, and Banana-Doughnut Kernels, *Geophys. J. Int.,* **160** 195-216.

Yang, Y., & D.W. Forsyth, 2006. Regional tomographic inversion of amplitude and phase of Rayleigh waves with 2-D sensitivity kernels, *Geophys. J. Int.,* , **166**, 1148-1160.

Zhao, L., Jordan, T. H. & Chapman, C. H., 2000. Three-dimensional Fréchet differential kernels for seismic delay times *Geophys. J. Int.,* **141**, 558-576.

Zhou, Y., 2009. Surface-wave sensitivity to 3-D anelasticity, *Geophys. J. Int.,* **178**, 1403-1410.

Zhou, Y., 2010. The scale dependence of finite-frequency effects in traveltimes and amplitudes, abstract S31A-2014 presented at 2010 Fall Meeting, AGU, San Francisco, Calif., 13-17 Dec.

Zhou, Y., Dahlen, F. A. & Nolet, G., 2004. Three-dimensional sensitivity kernels for surface wave observables, *Geophys. J. Int.,* **158**, 142-168.

Zhou, Y., Dahlen, F. A., Nolet, G., and Laske, G., 2005. Finite-frequency effects in global surface-wave tomography, *Geophys. J. Int.,* **163**, 10871111.

Zhou, Y., Liu, Q., & Tromp, J., 2011. Surface wave sensitivity: mode summation versus adjoint SEM, *Geophys. J. Int.,* **187**, 1560-1576.

Zhou, Y., Nolet, G., Dahlen, F. A. & Laske, G., 2006. Global upper-mantle structure from finite-frequency surface-wave tomography, *J. geophys. Res.,* **111** B04304, doi:10.1029/2005JB003677.

Chapter 5

Conclusion

In this thesis, I investigate the effects of lateral perturbations in anelasticity (Q) and wave speed on surface wave travel times and amplitudes by wave propagation simulations using the Spectral Element Method. Synthetic seismograms computed in earth models with and without 3-D wave speed structures are measured to examine elastic effects, and seismograms computed in earth models with and without 3-D Q structures are used to examine anelastic effects. By comparing phase delays and amplitude perturbations caused by 3-D wave speed and 3-D Q structures, I quantify the relative significance of wave speed and Q structures on surface-wave travel times and amplitudes.

Numerical experiments based on wave propagation in 3-D global models at teleseismic distance show that anelastic dispersion effects on surface-wave phase delays caused by lateral perturbations in anelasticity (Q_μ) are significant. 3-D anelastic dispersion increases with wave period and can account for 15-20$\%$ of observed phase delays at period range from 50 s to 200 s. The effects are strongly frequency dependent as a result of local S-wave anelastic dispersion, frequency dependent depth sensitivity of surface waves and 3-D distribution of perturbations in Q.

Calculations of surface-wave amplitude perturbations show that wave attenuation caused by lateral

perturbations in Q is only important at short-period ($\sim$ 50 s), and becomes less significant at longer period ($>$ 100 s), while elastic focusing/defocusing effects caused by 3-D wave speed are dominant effects in long-period surface waves. In the framework of ray theory, we decompose amplitude perturbations into elastic focusing/defocusing, attenuation and anelastic focusing/defocusing. Ray-theoretical calculations confirm elastic focusing is the dominant effect in surface wave amplitudes, in addition, calculations show that anelastic focusing becomes more significant than attenuation in long-period ($\sim$ 200 s) surface waves. Anelastic focusing effects have been long ignored in global tomography studies of 3-D Q structures and may result in biased tomographic models. Calculations also show that if lateral heterogeneities in the mantle are purely thermal-induced, anelastic focusing/defocusing will be positively correlated with elastic focusing/defocusing.

The 3-D Q models used in this study are constructed from a global tomography wave speed model S20RTS assuming lateral heterogeneities in the mantle are due to temperature perturbations. The magnitude of the Q model is consistent with current tomography studies. Assuming current tomography models are correct in order of magnitude, conclusions are applicable to wave propagation in the Earth. Calculations using end member mineralogical parameters show that the effects on the theoretical results are very limited.

I investigate finite frequency effects in 3-D earth models by comparing surface-wave phase delays and amplitude perturbations predicted using ray theory and finite frequency theory with those measured from SEM synthetic seismograms. Finite frequency kernels are developed to account for the dual dependence of surface-wave travel times and amplitudes on perturbations in wave speed and anelasticity as well as effects of measurement techniques which can not be accounted for in ray theory. Comparisons between ray-theoretical and kernel predictions show that finite frequency effects are stronger in amplitudes than in phase delays, especially at long periods. Theoretical predictions are compared with “ground-truth” measurements of synthetic seismograms from SEM simulations. Ray theory works reasonably well in predicting amplitude perturbations for short-period surface waves

but breaks down at longer periods. It is worth pointing out global model (e.g., S20RTS) used in this dissertation are smooth and dominated by long wavelength structures. Finite frequency effects are dependent upon path length as well as the length scale of heterogeneities in the earth model (Ch. 4, Zhou, 2010). When heterogeneities become smaller than wavelength, finite frequency effects will become more prominent than what have been shown in our numerical experiments.

In present-day tomography studies, surface-wave travel times have been used to invert for 3-D wave speed models and amplitudes have been used to invert for 3-D Q models. Consider that (1) 3-D anelasticity can significantly affect traveltime through anelastic dispersion and (2) 3-D wave speed structures can cause focusing/defocusing of amplitudes and it is difficult to separate the effects from anelastic effects, it is necessary to fully take into account the dual dependence in tomography studies and simultaneously invert surface-wave amplitude and phase delays for 3-D wave speed and 3-D Q models. Finite frequency kernels introduced in Chapter 4 can be used to simultaneously image 3-D wave speed and 3-D Q models in Earth's mantle.